Directionality of the strain aging effect in ultra low carbon steel

by

Wendel Melo

B.A., Centro Universitário do Leste de Minas Gerais, 2015

A THESIS SUBMITTED IN PARTIAL FULFILLMENT OF

THE REQUIREMENTS FOR THE DEGREE OF

MASTER OF APPLIED SCIENCE

in

THE FACULTY OF GRADUATE AND POSTDOCTORAL STUDIES

(Materials Engineering)

THE UNIVERSITY OF BRITISH COLUMBIA

(Vancouver)

July 2020

The following individuals certify that they have read, and recommend to the Faculty of Graduate and Postdoctoral Studies for acceptance, a thesis entitled:

Directionality of the strain aging effect in ultra low carbon steel

submitted by Wendel Melo in partial fulfillment of the requirements for

the degree of Master of Applied Science

in Materials Engineering

Examining Committee:

Chad W. Sinclair, Department of Materials Engineering
Supervisor

Warren Poole, Department of Materials Engineering
Supervisory Committee Member

Rizhi Wang, Department of Materials Engineering
Supervisory Committee Member

Abstract

This thesis contributes to the understanding of strain aging in ultra-low carbon (ULC) steels. Three studies (chapters 5, 6 and 7) were performed to achieve the end results. First, the kinetics of strain aging following monotonic tensile tests were measured and compared to an analytical model that can be used to predict the upper and lower yield strength for different aging temperatures and times. Next, the stress-strain behavior was evaluated. Lüders band formation was investigated using a model coupled to simulations using the finite element method (FEM). Digital image correlation (DIC) experiments were performed for comparison with the FEM simulations. Results showed many similarities between both methods, which increases the credibility of the FEM application. Good agreement between experiments and simulations was found. Finally, the directionality of strain aging was studied. Samples were taken from rolled sheet at 0˚, 45˚ and 90˚ to the rolling direction (RD). These were reloaded in tension following aging, the results being very different to those obtained from monotonic tensile tests. In particular, the strain path change was found to result in a large change in work hardening rate and a small effect on the yield strength. This was discussed in terms of a physically based model for strain aging.

Lay summary

Ultra-low carbon steels belong to a class of bake hardenable steels and are an excellent choice for materials applications requiring a combination of good formability and high yield strength. Descriptions of bake hardenability are normally defined in terms of monotonic tensile tests. Sheet forming processes used commercially commonly lead to deformation paths that are very different from those found in a pure tension test. The directionality of the strain aging effect is not yet understood. This brings uncertainty for the prediction of material behavior in fabrication and in service. In this work, different deformation paths are investigated using experimental work, analytical models, and numerical simulations to better understand the mechanical behavior of ULC steels. The conclusion of this work provides guidelines about the different mechanical behavior expected for aged ULC steels deformed in different deformation paths.

Preface

The work presented in this thesis was performed at the University of British Columbia, more specifically in the department of Materials Engineering, with supervision and continuous collaboration of Dr. C. W. Sinclair. The steel used in this work was supplied by ArcelorMittal Dofasco in a cold-rolled state. All experimental design, heat treatment, sample preparation, metallography, tensile test, cold rolling test, digital image correlation, Abaqus template and V-Uhard subroutines has been done by the author.

Table of contents

List of tables

List of figures

List of symbols

A: Parameter that depends on elastic constants and change in shape caused by a solute atom.

b: Burgers vector.

b_{BH}: Coefficient term that accounts for the effect of grain size and strain rate.

b_1: Material parameter related to strain hardening behavior.

b_2: Material parameter related to softening behavior.

c: Equilibrium concentration of solute atoms in an "atmosphere" around each dislocation.

c_o: Bulk concentration of solute.

Cs: Total number of carbon atoms per unit length of dislocations required to form an atmosphere

$C(t)$: Total number of solute atoms segregating per unit length of dislocation within time.

of one atom per atom plane.

$c(t)$: Rate of solute segregation.

D: is diffusion coefficient.

d: Grain size.

E_1: Plastic strain increment during first deformation path.

E_2: Plastic strain increment during second deformation path.

G: Shear modulus.

k: Boltzmann's constant.

K_d: Constant.

K_1: constant that depend on the test conditions.

K_2: constants that depend on the test conditions.

K3: Hardening fitting parameter.

K4: Softening fitting parameter.

K30: Locking of ρ_{f0} parameter.

K40: Recovering of ρ_{f0} parameter.

L_{band}: Lüders band length.

L_o: Initial dislocation length.

$L(t)$: Length of dislocation still free of carbon.

M: Taylor factor.

m: material parameter (inverse rate sensitivity).

P_{ij}: Elastic dipole moment tensor.

Q_{BH}: Parameter.

Q_1: Material parameter related to strain hardening behavior.

Q_2: Material parameter related to softening behavior.

q: material parameter.

r: Radius of iron.

r_{dis}: Distance from the dislocation core.

ro: Minimum distance from the core of the dislocation where linear elasticity theory is applicable.

S: Constant.

T: Temperature.

t: Time.

t_f: Final thickness.

t_o: Initial thickness.

U: Binding energy.

U_{max}: Maximum binding energy.

ΔV: Change in Volume.

ν: Poisson`s ratio.

ϵ : Strain due solute atom.

Θ: Polar coordinate measured from the dislocation core.

$\in_{ij}$: The strain field around dislocation at the position of the point defect.

λ: Atomic diameter of iron atom.

f: Fraction of dislocation density.

β: Angle between the rolling direction (RD) and tested tensile axis.

Δt_f: Standard error of the mean value of t_f.

Δt_o: Standard error of the mean value of t_o.

θ: Angle between first and second deformation path.

σ_f: Last load before aging.

σ_L: Lower yield stress.

σ_H: Hydrostatic Pressure.

σ_{max}: Maximum stress of local behavior constitutive law.

σ_{min}: Minimum stress of local behavior constitutive law.

σ_{BH}: Extra hardening term (overstress).

σ_o : Friction stress.

σ_ρ: Stress at RD.

σ_U : Upper yield stress.

σ_β: Stress at β angle.

σ_{xz}: Shear stress in x-y plane.

σ_{yz}: Shear stress in y-z plane.

Δσ: Increase in yield stress.

$\Delta\sigma_U$: The difference between the upper yield stress and the stress at the point of unloading from pre-loading.

$\Delta\sigma_L$: The difference between the lower yield stress and the stress at the point of unloading from pre-loading.

$\Delta\sigma_{max}$: Maximum increase in yield strength.

$\Delta\sigma_{Umax}$: Maximum increase in upper yield stress.

$\Delta\sigma_{Lmax}$: Maximum increase in lower yield stress.

$\sigma_{a_{\varepsilon_p=\varepsilon_L}}$: Stress at yield point elongation after aging treatment.

$\sigma_{n_{\varepsilon_p=\varepsilon_L}}$: Stress developed during loading the as-received sample at a strain corresponding to yield point elongation of aged sample.

$\Delta\sigma_{\varepsilon_p=\varepsilon_L}$: Difference between $\sigma_{a_{\varepsilon_p=\varepsilon_L}}$ and $\sigma_{n_{\varepsilon_p=\varepsilon_L}}$.

τ: Applied stress resolved in the slip plane.

τ_0: Shear stress for $\bar{v} = \frac{1m}{s}$.

ε : Strain.

ε_{eq}: Equivalent plastic strain.

ε_p: Plastic strain.

ε_L: Yield point elongation.

ε_{min}: Minimum strain (local behavior constitutive law).

ε_{max}: Maximum strain induced by Lüders band

$\Delta\varepsilon$: Local behavior change in strain.

$\dot{\varepsilon}$: Strain rate.

$\dot{\varepsilon}_o$: Reference strain rate.

$\bar{v}$: Average velocity of dislocations.

v: Lüders band velocity.

α : Saada constant.

η: Parameter associated with generation rate of mobile dislocations.

β^*: Constant.

ρ_f : Forest dislocation density.

ρ_{f0}: Locked forest dislocation density.

ρ_m: Mobile dislocation density.

List of abbreviations

BBC: Body Center Cubic.

DIC: Digital Image Correlation.

FEM: Finite Element Model.

HSLA: High Strength Low Alloy.

IRT: Infrared Thermography.

ND: Normal Direction.

O: Octahedral.

RD: Rolling Direction.

T: Tetrahedral.

TEM: Transmission Electron Microscope.

TD: Transverse Direction.

UBC: University of British Columbia.

ULC: Ultra Low Carbon.

Acknowledgements

I would like to express my gratitude to those who have helped me to make this thesis possible. First, I would like to thank God for all of the blessings that He has bestowed on me thus far. Then, I would like to thank my supervisor Dr. Chad W. Sinclair for this unique opportunity to join the University of British Columbia. I was lucky to have a supervisor whose dedication and passion for materials science inspired me to learn so much during the last 3 years.

I appreciated the support of the members of the faculty and the Department of Materials Engineering. Especially, I wish to thank the shopping machine staff (Ross Mcleod, Carl Ng, and David Torok) for their expert services and assistance. Also, I would like to thank Ali Khajezad and Willian Sparling for their comradery, discussions and advices.

This work would not be possible without the support of my wonderful wife, Midyan. She has encouraged me during the hardest times of this work and her positive thoughts helped me to be a more resilient person. Also, I would like to show my gratitude towards my parents (Evandro and Neusa) and my sister (Franciele) who during my absence showed their trust, support and love to me.

Lastly, I wish to also thank ArcelorMittal Dofasco for providing us with ULC steel sheets used for this study, and the National Science and Engineering Council of Canada for providing support for this project.

Chapter 1: Introduction

Understanding strain aging effects in ultra-low carbon (ULC) steels brings unique application opportunities for industry[1]. For instance, ULC steels, which normally present excellent formability, can increase in strength if strain aged after the final shape is reached, a process also known as bake hardening [1], [2]. In addition to these steels guaranteeing good levels of deformation and strength during processing and working, they can replace other steels in industry to reduce weight and improve safety [2], [3]. Therefore, comprehending the strain aging effect might improve the mechanical behavior of ULC steels and help designers to produce materials with better final performance.

Strain aging is usually described in terms of effects observed following uniaxial tensile tests. In particular, the yield strength is increased when the material is deformed, then aged (at low temperature) then tested again in the same direction [4], [5]. During metal forming, however, the material is normally submitted to complex strain paths, and strain aging cannot be understood by only unidirectional tests [5]–[7]. The influence of strain aging when materials are reloaded in a direction different to the direction before aging is not yet well understood and far less investigated than the strain aging effect from tensile tests performed in the same direction. For instance, Richards et al. [8] have investigated samples taken from the circumferential and longitudinal direction in two different sections of steel pipes, the pipes having been formed by the UOE process. These pipes were aged at room temperature during the summer months in service. After the samples were tensile tested, the results showed that in the circumferential direction the material exhibited an upper yield point, a lower yield point, and yield point elongation. In contrast, the longitudinal tested samples showed a round transition from elastic to plastic deformation, a much lower yield stress, and a higher work hardening rate [8].

This work aims to explore the kinetics of strain aging on ULC steels for different deformation histories. Specifically, in the laboratory, pre-deformation is imposed either using tensile loading or cold rolling, with specimens being tested in different deformation paths after pre-deformation and aging (distinct temperatures and times). In parallel, a finite element model (FEM) was developed to predict both Lüders band formation and strain aging. This was developed by coupling a practical understanding of the kinetics of strain aging with constitutive laws that were found to predict the strain aging effect in ULC steels for different deformation histories. Digital image correlation (DIC) was used to track the non-uniform deformation resulting from Lüders band propagation and the observations compared to the numerical simulations.

Chapter 2: Literature review

This chapter reviews basic concepts important for the current study. It reviews basic knowledge of static strain aging from the macroscopic to the microscopic point of view, covering its kinetics, current theories on the origin of the upper and the lower yield point, yield point elongation, anisotropy, deformation history and some factors affecting strain aging. Also, a basic review of models developed to predict the Lüders band formation and propagation in relation to strain aging is discussed.

2.1 The strain aging effect

From a macroscopic point of view, strain aging evolves the mechanical behavior of the material; strain aging increases the strength and hardness of the material and decreases its ductility and toughness [9]–[11]. Two types of strain aging are often discussed in the literature: static and dynamic strain aging. When strain aging occurs after plastic deformation at 'low' temperature (often at room temperature for low carbon steels), it is termed static strain aging. In contrast, dynamic strain aging occurs concurrently with plastic deformation at temperatures between 100-300°C and strain rates of between $10^{-4} - 10^{1}\ s^{-1}$ in low carbon steels [12], [13] [14], [15]. This study focuses on static strain aging in steels.

Strain aging changes the mechanical behavior of metals due to the interaction of interstitial solute atoms and dislocations [16]. This phenomenon is seen in almost all steels, including ultra-low carbon (ULC) steels, and micro-alloyed steels used in high-strength pipelines

[8], [17]–[22] where diffusion of carbon and nitrogen towards dislocations are responsible for Cottrell atmospheres formation [23], [24]. Only small amounts of carbon or nitrogen in solution are required for steels to experience strain aging [23]. For instance, ultra-low carbon (ULC) steels contain less than 50 ppm of carbon yet can exhibit significant strengthening by aging [15], [16], [19].

Strain aging occurs at room temperature (long aging times) but can be accelerated at elevated temperature due increases in diffusivity of solute atoms towards dislocations[8], [11]. For example, if an ULC steel is loaded up to point x in Figure 2.1 (label A), unloaded, and immediately reloaded again (label b), it is expected that the material will follow the same working hardening path to that of a material monotonically loaded along the same path. However, if the specimen was unloaded at point y and aged, an increase in yield strength ($\Delta\sigma$), the reappearance of the upper (σ_U) and lower yield strength (σ_L), followed by a yield point elongation (ε_L) would be expected when the material is reloaded (Figure 2.1, label C). These are the standard characteristics of a strain aged ULC steel when the reloading occurs in the same direction compared to first deformation before aging.

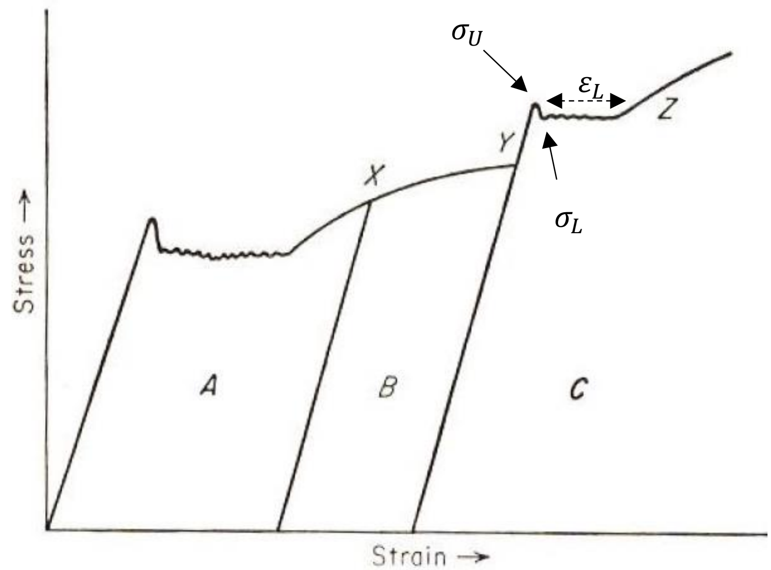

Figure 2-1: Schematic stress-strain curve for an ultra-low carbon steel. Region A represents a specimen subjected to pre-deformation. Region B shows no aging after immediately reloading the sample, and region C displays the reappearance of upper and lower yield point, and yield point elongation after aging [11].

2.2 Binding energy between solute atoms and dislocations in BCC iron

Although the strain aging effect has been known since the earliest days of steel making [25], it was only in 1949 that Cottrell and Bilby presented the first physically based model to explain it at the microscopic scale[23]. The value of this simple model is illustrated by the fact that many aspects of this theory are still used today [23]. The model states that diffusion of carbon and/or nitrogen to dislocations is responsible for making their motion harder, and thus the stress to cause plastic strain, much higher than it would be if the carbon/nitrogen was randomly distributed [8]. Interaction between solute atoms and dislocation is assumed to occur due to the binding energy between the elastic stress field of the dislocation and the misfit strain introduced by the solute atom in the iron lattice. This strong binding between dislocations and solute atoms reduces the energy of the system meaning that a high stress must be imposed to pull the dislocation away. This qualitatively has been used as main phenomena responsible for the increase in yield strength seen macroscopically during reloading of an aged sample. This is commonly called the first stage of aging[19], [26]. Depending on the solute concentration, aging time, and pre-strain level, precipitation of carbides may also occur, which leads to an additional increase in yield stress, this occurring during what is called the second stage of aging [3], [16].

The binding energy between dislocations and solute atoms can be calculated by evaluating the change in volume caused by the introduction of solute atoms in interstitial sites causing lattice distortion (ΔV), and by taking into account the hydrostatic pressure of dislocations' stress field (σ_H) [23], [25].

$$U = \sigma_H \, \Delta V \qquad (2.3)$$

Considering a change in volume of a sphere, and the pressure field of the dislocation $\sigma_H = \frac{1}{3}\left(\sigma_{xx} + \sigma_{yy} + \sigma_{zz}\right)$ equation 2.3 can be modified to:

$$U = \frac{4}{3}\frac{(1+\nu)}{(1-\nu)}\frac{Gb\epsilon r^3 \sin\Theta}{r_{dis}} \qquad (2.4)$$

Where $\nu, G, b, \epsilon \; and \; r$ are Poisson's ratio, shear modulus, burgers vector, strain due to solute atoms in the lattice, and radius of an iron atom. The parameters $\Theta \; and \; r_{dis}$ indicate the position of a solute atom in polar coordinates relative to the dislocation core (Figure 2.2). This equation can be condensed into:

$$U = \frac{A sin\Theta}{r_{dis}} \qquad (2.5)$$

From the difference between equation 2.5 and 2.4, A is defined as a parameter that depends on the elastic constants and the elastic deformation caused by the insertion of a solute atom. For carbon and nitrogen solute atoms in body-center (BCC) iron, the parameter A ≈ $3.15\text{x}10^{-29}$J m [27].

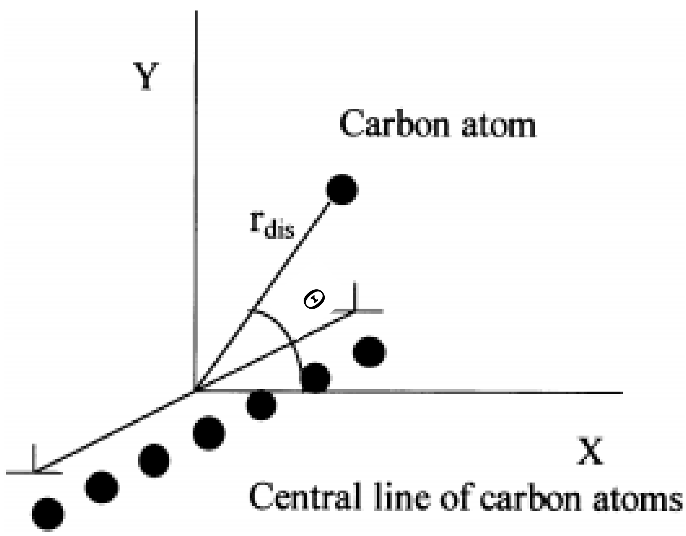

Figure 2-2: Carbon atom in the strain field of a positive edge dislocation and the central line of the Cottrell atmosphere [28].

It is important to emphasize that this equation is only valid outside of the core of the dislocation where linear elasticity is applicable. In BCC iron, the energetically most favorable position for carbon and nitrogen atoms is normally at $\Theta = \frac{3\pi}{2}$ and $r = ro \cong 2\ A$ [23], [25] . Cottrell [23] suggested that at this position, the atmosphere consists of a line of carbon atoms parallel to the dislocation line where the maximum binding energy (U_{max}) is expected to be in order of magnitude of $\approx 1\ eV$. At regions further way from this, the probability of finding a carbon atom is expected to differ from the average based on a Maxwell-Boltzmann distribution [23].

Equations 2.4 and 2.5 assume that solute atoms produce a spherically symmetric distortion of the lattice, i.e., there is an interaction with edge dislocations but not screw dislocations [25]. Solute atoms such as carbon and nitrogen sit in the distorted octahedral position of BCC iron, i.e. the midpoints of the edges of the BCC unit cell, which induces a non-isotropic, tetragonal distortion of the iron lattice [29], [10]. Then, the stress-strain field introduced by these solute atoms in the BCC iron matrix presents both shear and hydrostatic components producing shear and hydrostatic interactions with dislocations, i.e., solute atoms can interact strongly with screw and edge dislocations [30], [31]. To account for the interaction of solute atoms with both screw and edge dislocations in iron, a more general version of equation 2.3 can be used [32]:

$$U = P_{ij}\varepsilon_{ij} \qquad (2.6)$$

In elasticity theory, a point defect like carbon is represented as a singular source of strain and modeled by its elastic dipole moment tensor P_{ij}. The strain field around dislocations at the position of the point defect is accounted by ε_{ij} [29]. Figure 2.3 and 2.4 illustrate carbon-dislocation binding energy for a carbon atom sitting at octahedral (O) sites near an edge and screw dislocation computed using equation 2.6 with the dipole moment tensor parameterized from atomistic simulations.

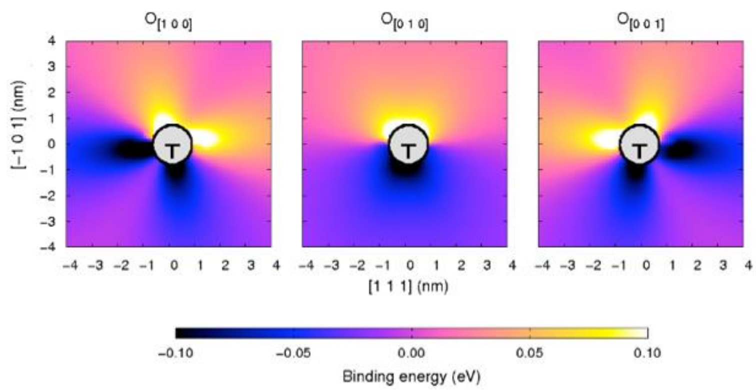

Figure 2-3: Mapping of carbon-dislocation binding energies obtained by atomistic simulations for carbon in the vicinity of a straight edge dislocation (in the center) which is aligned parallel to the $[1\bar{2}1]$ direction (perpendicular to the page). The gray circle in the center (diameter 8b) refers to the region termed dislocation core [29].

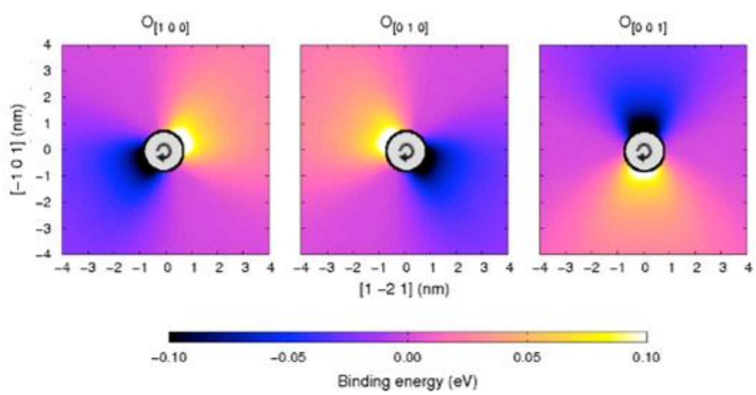

Figure 2-4: Mapping carbon-dislocation binding energies obtained by atomistic simulations for carbon in the vicinity of a straight screw dislocation (in the center) which is aligned parallel to the $[111]$ direction (perpendicular to the page). The gray circle in the center (diameter 8b) refers to the region termed dislocation core [29].

Looking at the above pictures, one can see that the binding energy tends to decrease proportionally to $1/r_{dis}$ for all cases [29], which can be also visualized through equation 2.5. Around an edge dislocation, the binding energy of a carbon atom sitting at octahedral site is affected mainly by normal stress σ_{xx} and σ_{yy} generated by the edge dislocation and related to the volume of the region occupied by carbon atom in iron [29]. On the contrary, a screw dislocation stress field presents predominately shear (σ_{xz} and σ_{yz}), which interacts with local shear stress induced by carbon atoms located at octahedral sites[29].

The binding energy between solute atoms and dislocations can be used to predict the equilibrium distribution of solute that would be located around a dislocation for a given bulk concentration of solute. The equilibrium concentration of solute atoms in an "atmosphere" around each dislocation was first given by Cottrell who used the Boltzmann distribution of solute atoms [23]:

$$c = c_o \exp\left(\frac{U}{kT}\right) \qquad (2.7)$$

Where c_o is the bulk atomic concentration of solute, k is the Boltzmann constant and T is the temperature. A problem arises when accounting for the carbon distribution around a dislocation, especially as r gets close to 0, where atomic fractions > 1 are predicted by equation 2.7. To solve this problem, Cottrell and Bilby assumed that at the dislocation core, $r < 1\ x10^{-7}cm$, carbon saturation is reached when the core contains one carbon per atom plane of dislocation [23], [25], [27]. This is valid if a change in concentration at any point does not alter substantially the value of U at that point. Later, Louat [33] proposed using Fermi-Dirac statistics to remove the problems of the Boltzmann distribution,

$$c = \frac{c_o \exp\left(\frac{U}{kT}\right)}{1+c_o \exp\left(\frac{U}{kT}\right)} \quad (2.8)$$

2.3 Migration of solute atoms towards dislocations

The Cottrell model described above describes only the equilibrium level of solute expected at a dislocation. Cottrell and Bilby proposed the first kinetic model to describe the time evolution of the solute atmosphere at a dislocation [23]. According to this model, the total number of solute atoms segregating per unit length of dislocation within time (t) during the formation of the atmosphere is given by:

$$\frac{C(t)}{Cs} = 3C_o\lambda \left(\frac{\pi}{2}\right)^{\frac{1}{3}} \left(\frac{ADt}{kT}\right)^{\frac{2}{3}} \qquad (2.9)$$

Where λ is the atomic diameter of an iron atom, C_o is the total number of atoms in solution per unit volume, Cs is the total number of carbon atoms per unit length of dislocation required to form an atmosphere of one atom per atom plane (Cs= 1/ λ), and D is the diffusion coefficient of the solute. De Cooman et al.[21] have modified this equation to consider the effect of solute saturation on the kinetics of strain aging.

The rate of solute segregation assumes that the rate is proportional to the concentration of solute remaining in solid solution, $c(t) = C_o - C(t)$. Here $C(t)$ is the concentration of solute already segregated [21]. It also assumes that the rate is proportional to the length of dislocation which is still free of solute, $L(t) = L_o - \lambda C(t)$. Considering the rate of diffusion towards the dislocation, Cottrell gave the rate as :

$$\frac{dC(t)}{dt} = L(t)c(t)\, 3\left(\frac{\pi}{2}\right)^{\frac{1}{3}}\left(\frac{ADt}{kT}\right)^{\frac{2}{3}} \qquad (2.10)$$

The Haper modification to eq 2.10 accounts for the lowering of solute concentration in the matrix surrounding the dislocations as aging occurs with time:

$$\frac{C(t)}{Cs} = 1 - \exp\left(3C_o\lambda\, \left(\frac{\pi}{2}\right)^{\frac{1}{3}}\left(\frac{ADt}{kT}\right)^{\frac{2}{3}}\right) \qquad (2.11)$$

Combining eq 2.9 - 2.11 and assuming that at the initial condition $C(t) = 0$, the segregated concentration can be calculated as:

$$\frac{C(t)}{Cs} = \frac{\left(1-\exp\left(3(L_o-C_o\lambda)\left(\frac{\pi}{2}\right)^{\frac{1}{3}}\left(\frac{ADt}{kT}\right)^{\frac{2}{3}}\right)\right)}{\left(1-\left(\frac{C_s}{C_o}\right)\exp\left(3(L_o-C_o\lambda)\left(\frac{\pi}{2}\right)^{\frac{1}{3}}\left(\frac{ADt}{kT}\right)^{\frac{2}{3}}\right)\right)} \qquad (2.12)$$

2.4 Measurement of the strain aging effect

The kinetics of strain aging is normally measured in terms of increase in yield strength [16]. Experimentally, the increase in yield strength due to the strain aging effect (Δσ) is measured either by the difference between upper yield strength after aging (σ_U) and the last load before aging (σ_f) or by subtracting the lower yield strength after aging (σ_L) from the last load before aging[19], [24], [34]. Figure 2.5 represents an example of experimental measurement of strain aging effect (Δσ).

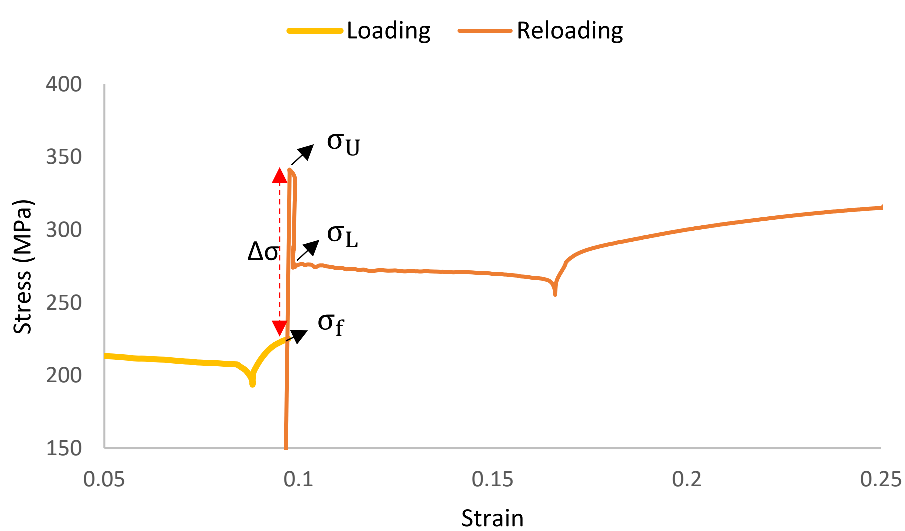

Figure 2-5: Measurement of strain aging effect using the difference between upper yield strength (σ_U) and last load before aging (σ_f).

It is typically assumed that the percentage increase in yield strength is proportional to the kinetics of solute segregation, i.e. $\frac{\Delta\sigma}{\Delta\sigma_{max}} = \frac{C(t)}{Cs}$ [33], [34]. This is only an approximation, ignoring the potential of other strengthening mechanisms[21]. Assuming this relationship between strengthening and segregation, it is common to re-write eq 2.11 as,

$$\Delta\sigma = \Delta\sigma_{max}\left(1 - \exp\left[-\left(\frac{t}{t^*}\right)^{\frac{2}{3}}\right]\right) \quad (2.13)$$

where $\Delta\sigma_{max}$ is the maximum increase in yield strength, t is time and t^* is a characteristic time that depends upon diffusion of solute atoms and binding energy between solute and dislocations (can be deduced from the difference between eq 2.13 and 2.11). Figure 2.6 displays the strain aging effect (Δσ) measured experimentally for different temperatures and times plotted against the above model (continuous line).

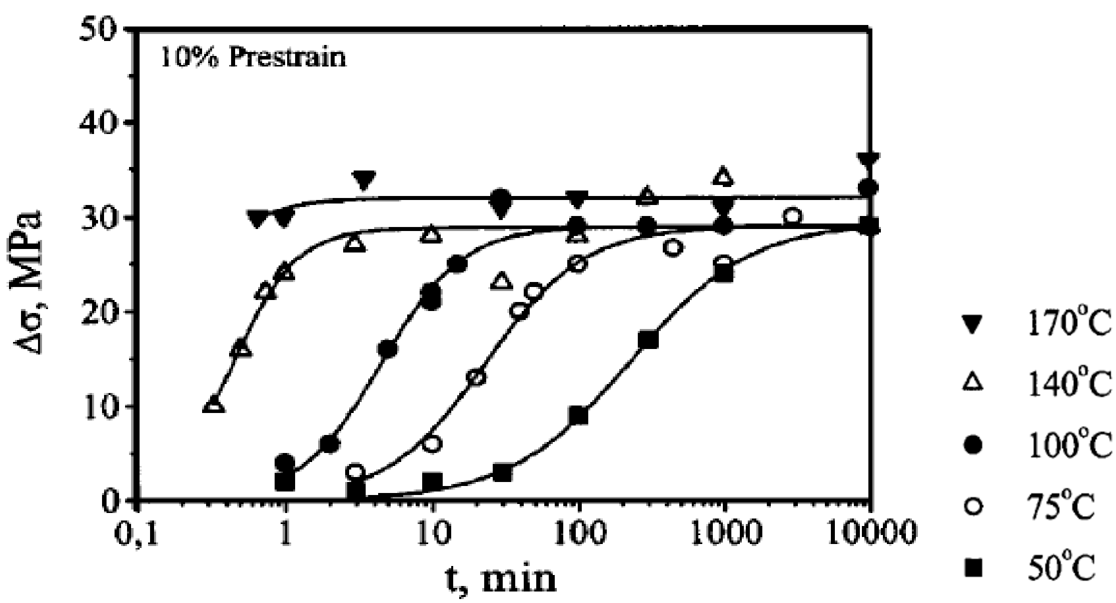

Figure 2-6: Increase in yield strength measured experimentally and compared to the Loaut Modification of the Cottrel model, eq 2.13 [16].

Another very useful model available to measure changes in yield stress due strain aging effect is described by the Hartley kinetic equation, which is derivated in same way as eq 2.13 [16], [29], [35] but invokes an extra parameter to facilitate fitting of experimental data:

$$\frac{\Delta\sigma}{\frac{1}{2}(\sigma_U+\sigma_f)} = \frac{\Delta\sigma}{\bar{\sigma}} = K_1 + K_2\left(\frac{Dt}{T}\right)^{\frac{2}{3}} \qquad (2.14)$$

Here K_1 and K_2 are constants that depend on the test conditions, D is the diffusion coefficient, σ_f is shown in Figure 2.5, and T is the aging temperature. The use of this model with experimental data is shown in the following Figure 2.7.

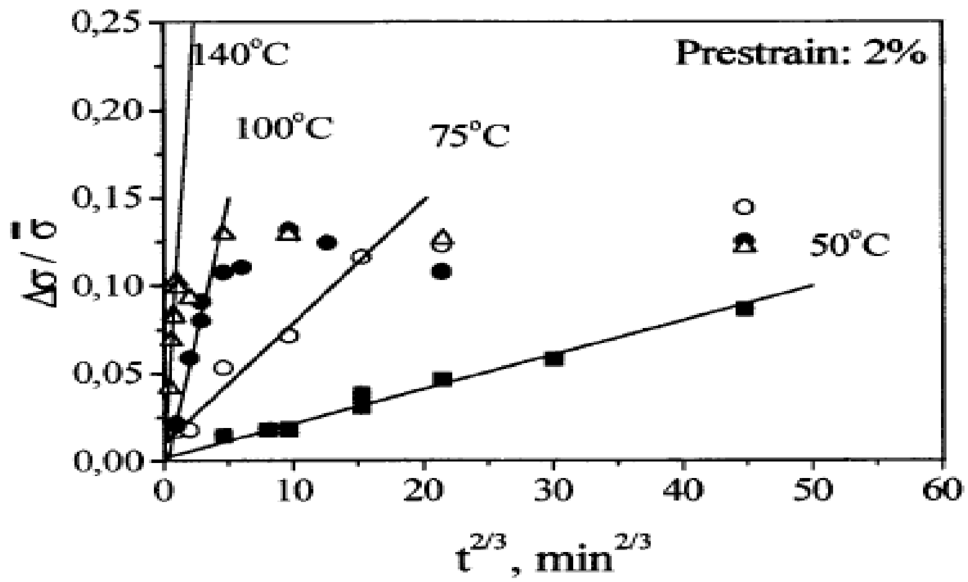

Figure 2-7: Increase in yield strength measured experimentally and compared to a model like the Hartly model [16].

2.5 Yield point in ultra-low carbon steels

Plastic deformation happens through the movement of dislocations. Especially in materials like ULC steels, the movement of dislocations are delayed due to ‘locking’ of dislocations by solute atmospheres. This increases the stress necessary for the onset of plastic deformation. For this reason, these materials show a characteristic stress-strain diagram with an upper yield point, followed by a yield point elongation during a tensile test as already explained. There are two basic concepts used to explain the origin of the upper yield point, in materials like ultra-low carbon steels. The first idea, originally proposed by Cottrell and Billby argues that at the upper yield point, dislocations are broken free from the Cottrel atmosphere and the stress to continue plastic deformation drops due to dislocations being unlocked.

The second theory, based on work by Johnston and Gilman[36], considers that the upper yield point is a consequence of a low density of mobile dislocations and that the generation of new dislocations at (or near) the upper yield point causes the formation of a Lüders band and a decrease in the flow stress. The fact that dislocations have a very strong interaction with their atmospheres, even at room temperature [23], supports the multiplication of mobile dislocation theory if one considers that the stress to unlock dislocations from their atmospheres would be unrealistically high due to the high binding energy. According to Hahn [37], the flow stress cannot be governed alone by the unlocking of dislocation at low temperature where pinning points are stationary. Furthermore, Johnston and Gilman [36] have found no evidence of dislocation unlocking in their study on plastic flow of LiF crystals.

The dislocation multiplication mechanism accounts for the effect of mobile dislocation on the stress necessary to maintain the imposed strain rate. This relation can be expressed using the Orowan equation:

$$\dot{\varepsilon} = b\rho_m \bar{v} \qquad (2.15)$$

Where b, ρ_m and $\bar{v}$ represents the magnitude of the Burgers vector, the mobile dislocation density, and the average velocity of dislocations, respectively. The average velocity of dislocations is determined by the mobile dislocation density and the need to meet the macroscopic strain rate. If the mobile dislocation density is low, the average velocity must be high. The average velocity typically is assumed to vary with the applied stress as:

$$\bar{v} \approx \left(\frac{\tau}{\tau_0}\right)^m \qquad (2.16)$$

Here τ, τ_0 and m are the applied shear stress resolved in the slip plane, the reference shear stress (the shear stress when $\bar{v} = \frac{1\mathrm{m}}{\mathrm{s}}$) and a parameter (inverse rate sensitivity) that varies according to the material and temperature, e.g. for steel at room temperature m = 35 [25]. After aging, when most dislocations have been locked by solute atoms, the number of mobile dislocations is very low and therefore, a high stress is necessary to meet the imposed strain rate. However, as yielding occurs, and new mobile dislocations are generated the stress drops without the need for unlocking dislocations pinned during strain aging by solute atoms. Following this idea, Hahn has developed a model able to predict the stress-strain curves of iron during tensile tests [37].

$$\sigma = q\varepsilon_p + 2\tau_o \left[\frac{\dot{\varepsilon}}{0.5bf(\rho_o + C\varepsilon_P^{\alpha})}\right]^{\frac{1}{m}} \qquad (2.17)$$

Where ε_p is the plastic strain, ρ_o is the initial dislocation density, C, and α are dislocation-density parameters q is a material parameter and f is a fraction of dislocation density.

2.6 Yield point elongation

The yield point elongation (ε_L) is a key characteristic of materials, like ULC steel, which shows non-uniform plastic deformation following the upper yield stress. In ULC steels, the initial macroscopic plastic response following the upper yield point is normally accompanied by a plateau in stress (Figure 3) where the specimen is divided into three regions: the region in which plastic deformation has already occurred (behind the Lüders band front), the area where plastic deformation is occurring (at the Lüders band front), and the region where plastic deformation has not yet started (ahead of Lüders band front) [11]. Once the Lüders bands have passed through the entirety of the tensile sample the material starts to deform uniformly.

The formation and characteristics of Lüders bands in low carbon steels can change depending on grain size [38]–[40], strain rate[40]–[42], and shape of samples [38], [43]. Also, other authors have noticed that temperature and carbon concentration affect the Lüders bands elongation [8]. Studies have shown, for example, that for a given range of grain size, two single bands can nucleate from each shoulder of a rectangular sample [38]. The same study also shows that circular cross-section samples with grain size above 0.15mm do not form sharp Lüders bands, but generally produce diffuse bands [38], [44].

When plastic deformation initiates, the local strain rate in the region deforming plastically exceeds that of the machine and the stress necessary to continue plastic deform drops drastically (lower yield strength) [25], [45]. The Lüders bands nucleate at areas of stress concentration like the shoulders of a flat cross-section specimen and are normally visible with the eye, oriented at approximately $\pm 55°$ to tensile axis[46]. Once the Lüders bands have propagated through the entire gauge length of the specimen, the stress is observed to increase with strain in the usual manner reflecting homogeneous deformation and strain hardening. Figure 2.8 shows the Lüders bands propagation during the yield point elongation.

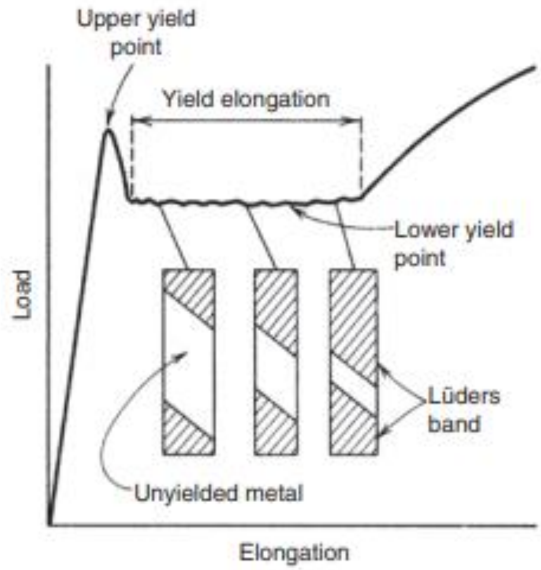

Figure 2-8: Represents the evolution of Lüders bands through the gauge length in flat cross-section [47].

2.7 Factors affecting strain aging in steels

Many authors in the literature have studied the factors affecting static strain aging in steels. For instance, the effect of the amount of pre-strain, strain rate, grain size, temperature, and aging time on the static strain aging was studied [10], [18], [21], [40].

De Cooman at.al [19] have performed experiments on ultra-low carbon steels for different pre-strain, and they found that the yield point elongation is reached at about the same time regardless of the pre-strain level. Furthermore, no clear dependence between increase in $\Delta\sigma$ with the degree of pre-straing at any stage of aging period was found. They concluded that the increase in strength reaches a saturation level after a certain amount of time, in their case about 30 MPa, no matter the tested pre-strain level and temperatures [16].

The strain aging effect increases with carbon content [3]. Van Snick et al. have shown that strain aging response can be increased from 40 to 70 MPa by varying carbon content between 0 to 40 ppm [3]. Further increase in carbon content was shown to have no effect on strain aging. Figure 2.9 shows the dependence of carbon content on bake aging response of ULC steels.

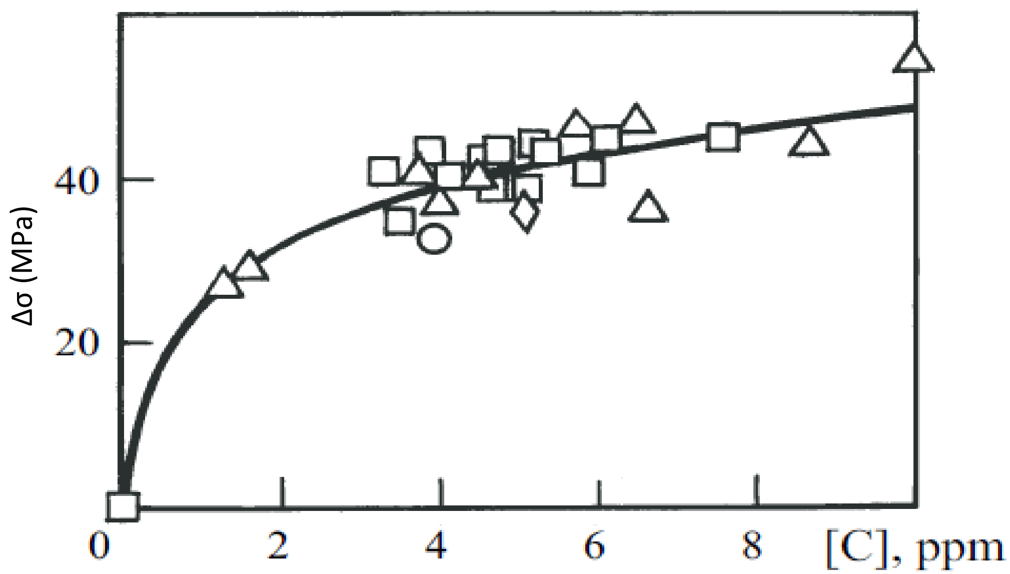

Figure 2-9: Relationship between carbon content and strain aging effect for ULC steels tested for different companies[48].

The grain size has been reported to affect strain aging, the magnitude of strain aging increasing with decreasing grain size [49]. This effect is justified by the contribution of carbon at the grain boundaries to the hardening processes or by difference in the intra/intergranular cementite precipitation [39]. However, De Cooman et al.[39] showed that for ULC steels, this idea is only valid for grain sizes of 15μm or smaller (Figure 2.10). They justify these findings by the fact that ULC steels contain only 30 ppm of carbon and a decrease in grain size increases the segregation sites at the grain boundary and decreases the diffusion distances from the grain interior to the grain boundary. This results in less carbon remaining in the matrix for segregation to dislocations [39], [50].

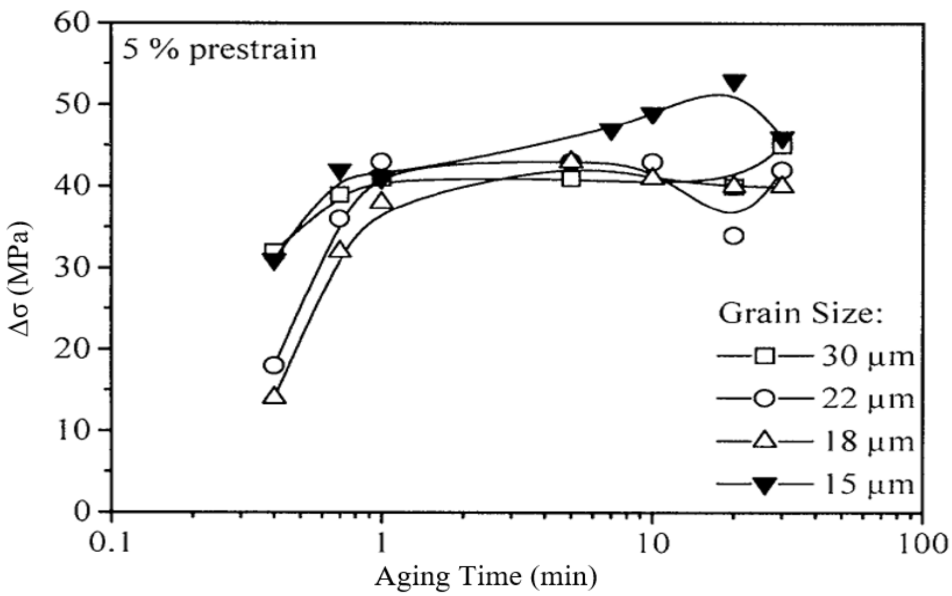

Figure 2-10: Strain effect in ULC steels for different strain sizes, 5% pre-strain and aging at 170˚C [39].

2.8 The effect of anisotropy and strain path changes on yield stress

It was shown above that strain aging increases the yield strength of ULC steels when the deformation path remains the same before and after aging. However, in real life, metals can undergo complex deformation histories. For instance, ULC steels can be subjected to plain strain deformation in stamping applications for automotive parts [5] or bending in UOE pipe making processes [8]. Because of this, it is important to understand how material and deformation anisotropy affects strain aging.

Plastic deformation in crystalline materials is inherently anisotropy because of texture [51], [52]. Texture is an intrinsic property of not only polycrystalline metals but also ceramics, polymers, and even rocks. Most materials are arranged as aggregates of crystals, and their crystallographic orientation are normally non-random, which means they have a preferred crystallographic orientation distribution (texture)[52]. A preferred texture is developed during growth or deformation and modified during recrystallization or phase transformation [51], [53], [54]. For instance, ULC steels normally have a γ (<111> // ND) fiber recrystallization texture [55]. This preferred texture is responsible for the excellent deep drawability of steels [56]–[58].

Texture directly correlates to the anisotropic properties of materials [54], [57], [59]. For example, Figure 2.11, curve 1, illustrates the initial yield strength anisotropy of a low carbon steel in a cold-rolled state. Here β is the angle between the rolling direction (RD) and tested tensile axis, σ_β is the stress at β angle, and σ_ρ is the yield stress measured parallel to RD [60]. In this study, the initial anisotropy was small, with a maximum of 5% increase in yield stress at around 50 degrees to RD.

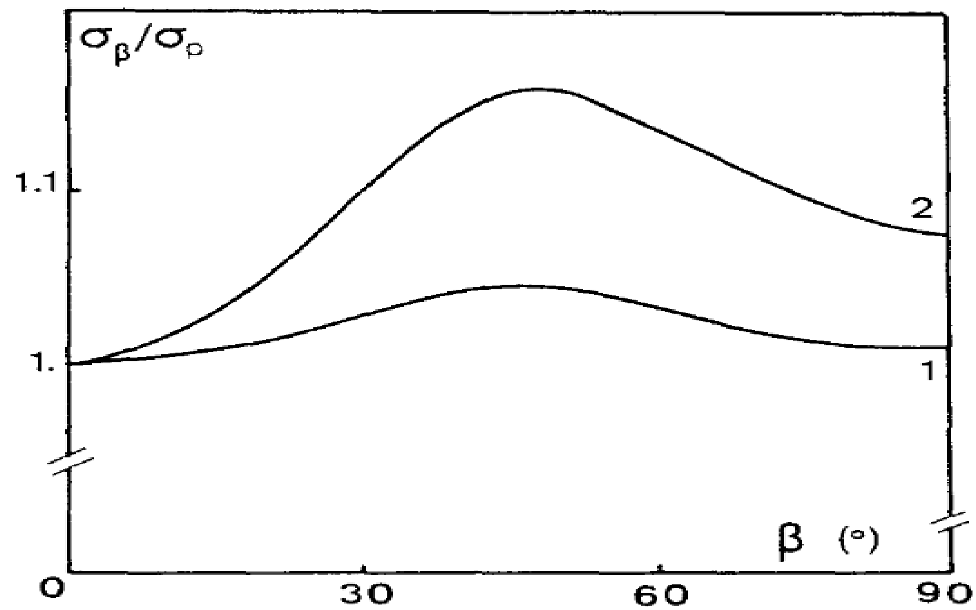

Figure 2-11: Curve 1: Variation of yield stress at angle β to RD relative to the yield stress measured parallel to RD (σ_β/σ_ρ). Curve 2: the ratio σ_β/σ_ρ measured after a presetrain of 0.15 in the RD. [60].

Curve 2 in Figure 2.11 shows the effect of strain path change on the yield stress anisotropy of low carbon steels. In this case the material was prestrained to $\varepsilon = 0.15$ by tensile testing parallel to RD. Subsequently, the material was retested at different angles (β) to RD [60]. Studies have shown that changes in deformation path can affect the microstructure, leading to changes in yield stress and flow stress evolution [7], [61], [62]. Therefore, the subsequent plastic behavior is influenced by the anisotropic hardening, this being a function of the magnitude of the change in deformation path. Schmitt et al. [63] used this to develop an equation that allows one to quantify the magnitude of change in deformation path:

$$Cos\theta = \frac{E_1:E_2}{(E_1:E_1)^{\frac{1}{2}}(E_2:E_2)^{\frac{1}{2}}} \qquad (2.17)$$

In this equation, the terms E_1 and E_2 represent the plastic strain increment before and after the strain path change, respectively. This parameter corresponds to the cosine of the angle between E_1 and E_2 in the plastic strain space [4]. According to this relationship, cos θ = 1 is obtained for monotonic deformation, cos θ = -1 for Bauschinger tests, and cos θ = 0 for orthogonal tests. Examples of tests are displayed in table 2.1.

Table 2-1: Tests commonly used for the investigation of strain aging effect [35].

Test	Denomination	θ	$\cos\theta$
Uniaxial tension + uniaxial tension	UT-UT	0 deg	1
Shear in forward direction + shear in forward direction	S +/+	0 deg	1
Plane tension + uniaxial tension in the same direction	PT-UT	30 deg	0.86
Equibiaxial stretching + uniaxial tension	EBS-UT	60 deg	0.5
Uniaxial tension + uniaxial tension in a direction at 45 deg*	UT-UT 45 deg	76 deg	0.25
Plane tension + uniaxial tension in a direction at 90 deg	PT-UT 90 deg	90 deg	0
Uniaxial tension + uniaxial tension in a direction at 90 deg*	UT-UT 90 deg	120 deg	−0.5
Shear in forward direction + shear in reverse direction	S ±	180 deg	−1
Uniaxial tension + uniaxial compression*	UT-UC	180 deg	−1

2.9 Directionality of strain aging

Carbon steels deformed beyond the yield point elongation, when unloaded, aged, and strained further in the same direction, show the reappearance of the yield point elongation. The effect of strain aging in monotonic loading has been widely studied in the literature [18], [19], [23]. When steels are strained further in a direction different from that before aging, the strain aging response has been much less investigated.

Elliot et al. [64] have carried out experiments on low carbon steel specimens to evaluate the importance of the deformation path on strain aging (Figure 2.12). Their results showed a surprising result when the specimens were strained in a direction opposite to that of the first deformation after aging. Permanent softening and no trace of yield point phenomenon was observed whenever reversed deformation was performed. This loss of strength upon re-straining in a direction opposite to the original direction is referred to, in literature, as Baushcinger effect [65], [66]. Furthermore, according to this work, only the direction just before and just after aging matters; the early past of the sample has no influence. For instance, when the material was deformed in opposite direction (5) compared to first deformation performed in this work (1), aged and reloaded again (6) in the same direction to that of before aging, the upper and lower yield point was present; the prior part of the deformation showed no influence.

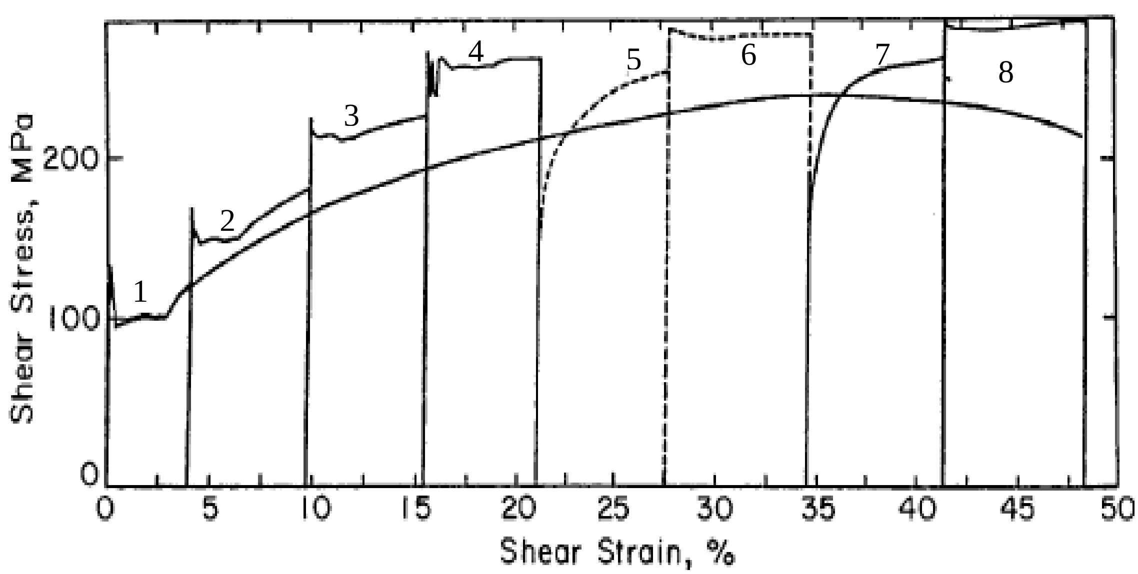

Figure 2-12: Stress and strain of same sign (full curves) and of opposite signs (dashed curves) [64].

Williams [65] tried to demonstrate in his experiments on a HSLA steel that it is possible to obtain yield point elongation when the deformation direction is reversed if the specimen is adequately aged [65]. In this work, a very high aging temperature was used (315ºC), so it is most likely that both segregation and precipitation occurred during aging [3], [16]. In addition, even though the yield stress increases with pre-strain (Figure 2.13), at the maximum pre-strain level, the yield stress was still 10 percent lower than the as-received steel. He concluded that the strain aging was quite efficient in reducing the Bauschinger effect, even though it did not completely eliminate it.

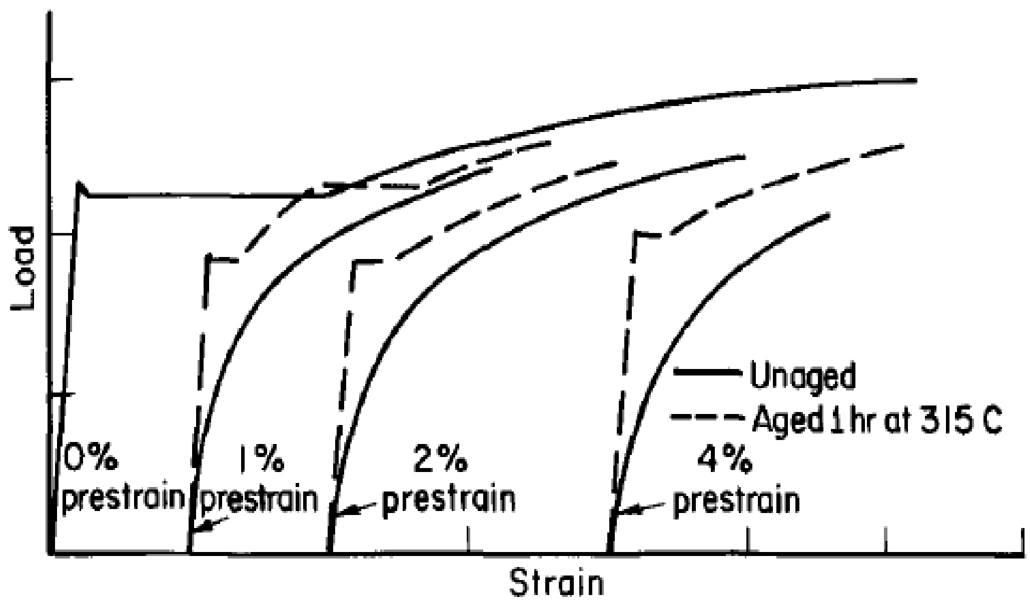

Figure 2-13: Load vs strain curves after various amounts of tensile pre-strain, with and without subsequent aging [65].

Directionality of strain aging has also been measured by preparing tensile test specimen from a pre-strained sheet. Yonemura et al [5] have compared the proof stress of samples strained in different direction relative to a first deformation parallel to the sheet's RD (Figure 2.14). In this work they have found a strong anisotropy after pre-straining, even though the as-received proof stress was independent of the test direction. On the other hand, aging the pre-strained samples and reloading them in different directions reduced anisotropy.

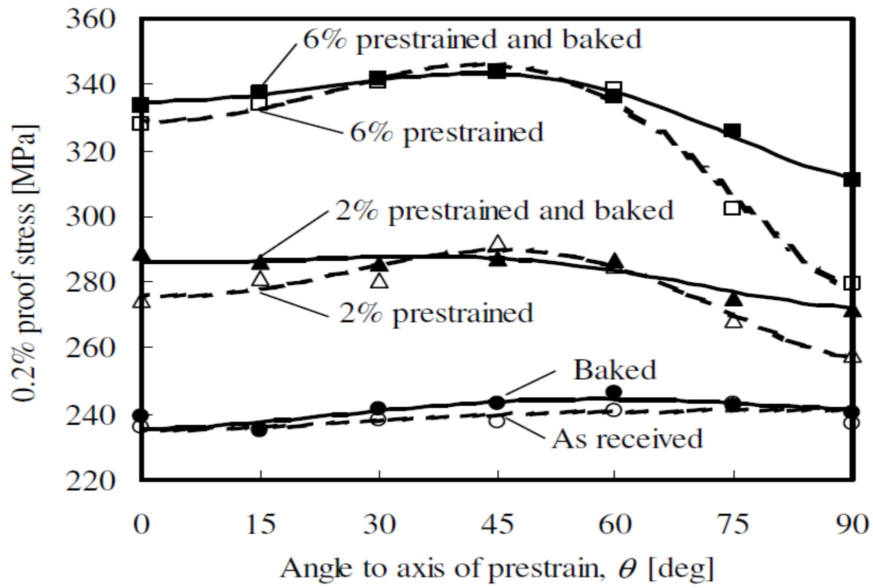

Figure 2-14: Anisotropy of proof stress in a pre-strained and strain aged bake-hardenable steel [5].

The relationship between the deformation behavior and the microstructural evolution has been studied in the literature, especially for two strain paths [5], [60], [61], [67]. The Bauschinger effect, when the second deformation occurs in a reverse direction, and the cross effect, when second deformation is orthogonal to the first one, are typically reported phenomena [61], [68]. The first one causes a decrease in the subsequent yield stress, which is believed to be related to internal stresses in the material developed during previous plastic deformation (Figure 2.13) [64], [65]. Internal stresses are generated by heterogeneous deformation of grains, particles and dislocation cells [5]. During plastic deformation dislocations interact with different obstacles leading to back stresses [66]. During reversed deformation, this back stress can help dislocations to move in the reverse direction [5], [66].   The cross-effect, which causes an increase of the subsequent yield stress when second deformation is perpendicular to first deformation [68], is believed to arise from a change in active slip systems on strain path change [5][68].

2.10 Prediction of Lüders bands and strain aging

One of the challenges in strain aging is to predict Lüders band formation and its effect on the macroscopic stress-strain response. Finite element method (FEM) simulations have been developed to enable one to test different constitutive laws and to compare the predicted stress-strain response with that measured in experiments.

Several different constitutive laws have been tested in the literature in an attempt to understand the propagation of Lüders bands [24], [69]–[71]. Ballarin et.al. described Lüders band nucleation using a physical model having three components: (1) prediction of solute carbon content necessary for dislocation pinning, (2) prediction of dislocation density and (3) determination of strain aging kinetics [24]. This model uses the same idea introduced by Tsukahara and Iung [72]; however, here, an exponential constitutive law was used to determine the Von Mises stress:

$$\sigma = \sigma_{max} + Q_1.\left(1 - e^{-b_1.\varepsilon_p}\right) + Q_2.\left(1 - e^{-b_2.\varepsilon_p}\right) \qquad (2.18)$$

Where σ_{max} is the same as the applied upper yield strength σ_U, ε_p is the plastic strain, Q_1, Q_2, b_1 and b_2 are material parameters. The first part of this equation accounts for the strain hardening behavior while the second part describes the initial softening behavior, respectively [24]. During simulation of strain localization, the local behavior is described by softening: the stress first rises to σ_{max} and then drops to σ_{min} at ε_{min} [73] as seen in Figure 2.15.

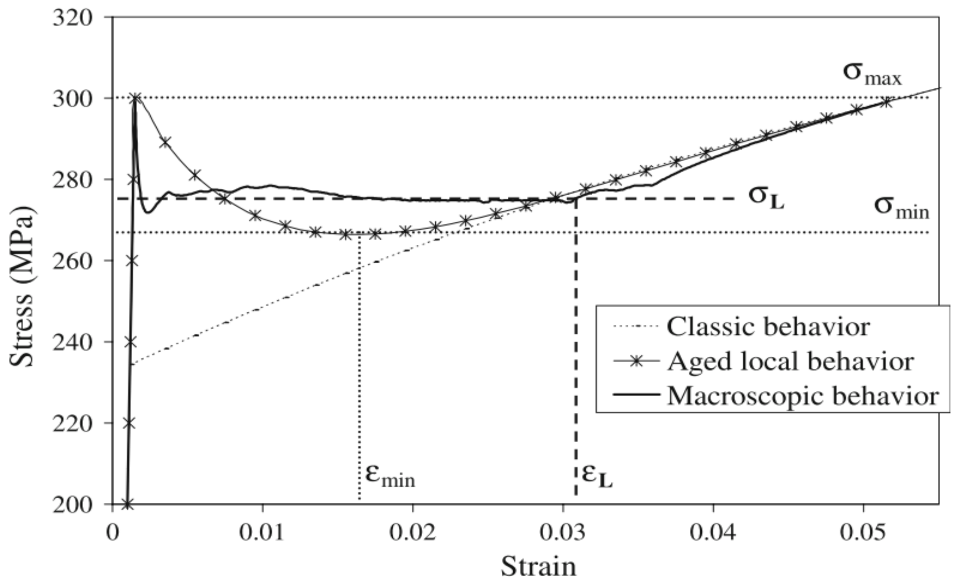

Figure 2-15: Represents the use of local behavior to predict Lüders band nucleation and comparison with classic behavior and macroscopic behavior [24].

In this model the terms σ_{max}, σ_{min} and ε_{min} are directly related to the experimentally measurable quantities σ_U, σ_L and ε_L. The relationship between the macroscopic lower yield stress (σ_L), maximum and minimum stresses of local behavior (σ_{min} and σ_{max}) was found to be:

$$\sigma_L - \sigma_{min} = 0.4(\sigma_{max} - \sigma_{min}) \qquad (2.19)$$

To predict strain aging an extra contribution to the flow stress (called the 'overstress' (σ_{BH}) by the authors) was added to equation 2.18 [24].

$$\sigma_{BH} = R_{BH} + Q_{BH}.\left(1 - e^{-b_{BH}.\left(\varepsilon^{p} - \varepsilon^{p}_{prestrain}\right)}\right) \qquad (2.20)$$

This equation is shown in Figure 2.16 as the solid black line which varies from R_{BH} at $\varepsilon^{p} = \varepsilon^{p}_{prestrain}$ to at $R_{BH} + Q_{BH}$ when $\varepsilon^{p} \gg \varepsilon^{p}_{prestrain}$. If It is clear that R_{BH} in this model should be proportional to the measured increase in upper yield stress induced by strain aging, $\Delta\sigma$ [24]. The parameter b_{BH} is meant to account for the effect of grain size and strain rate and was taken by the authors to follow for the form,

$$b_{BH} = K_{d}.d^{0.8} - S.\ln\left(\frac{\dot{\varepsilon}}{\dot{\varepsilon}_{o}}\right) \qquad (2.21)$$

Where d is grain size, $\dot{\varepsilon}$ is the strain rate, and K_{d}, S and $\dot{\varepsilon}_{o}$ are constants.

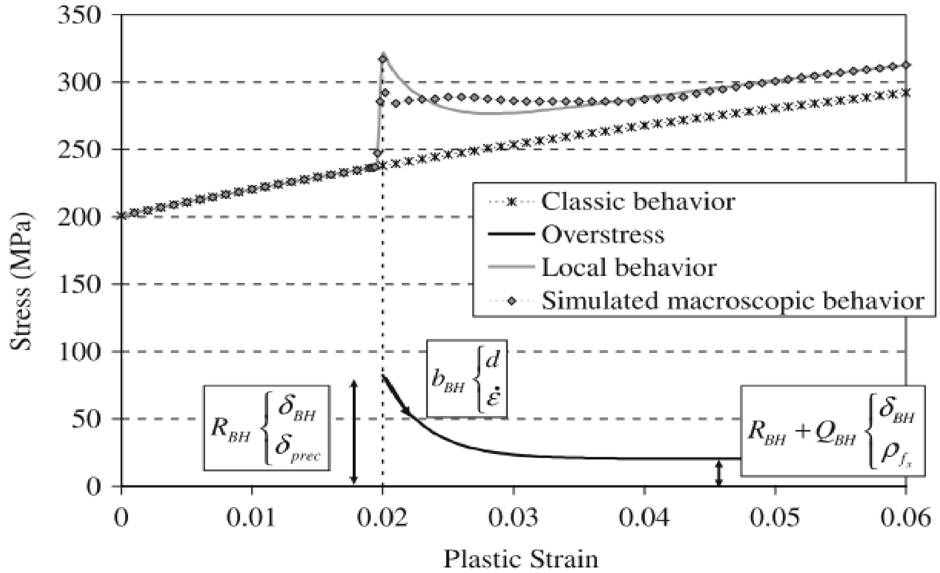

Figure 2-16: Simulation of strain aging effect by addition of the "overstress" equation (equation 2.20) to equation 2.18 [24].

These equations aim to predict the stress-strain behavior of materials such as ULC steel by following a similar idea to that originally proposed by Hahn [37]. A constitutive model (equations 2.18 and 2.20) are used to account for dislocation unlocking or multiplication at a high enough stress, causing load decreases before following a strain hardening behavior seen in Figures 15 and 16. Combined with the FE method this model allows for the prediction of Lüders band propagation as well as upper and lower yield stresses and yield point elongation. These have been shown to reasonably well predict Lüders band propagation and work hardening behaviors seen experimentally [69], [72], [74]–[76].

2.11 Summary

This literature review has highlighted important points about strain aging effect. At the microscopic scale, the binding energy between solute atoms and dislocations causes solute segregation and an increase in yield strength. If the material is pre-deformed then aged, solute segregation to dislocations leads to the appearance of an upper and lower yield stress and yield point elongation if the second loading direction is the same as the first. When the material is reloaded in a different direction after aging, the strain aging effect can be very different. Finally, a combination of a properly selected constitutive law and a finite element model can be used to predict the characteristic features in the stress-strain curve arising from strain aging.

Chapter 3: Scope and objectives

One of the tasks of a material engineer is to predict the material behavior in service. This can be quite a challenge, especially for aged ULC steels because they can behave quite differently according to their deformation history. In addition, the directionality of strain aging is not well understood. This limits the ability of the engineer to predict the mechanical behavior in service. Therefore, this project intends to investigate the effect of strain aging on the mechanical behavior of ULC steels for distinct deformation paths.

Firstly, the strain aging kinetics and mechanical properties of a ULC steel are studied using tension pre-deformation followed by aging and tensile deformation in the same direction. These results are compared against classical models for strain aging kinetics and shown to be in good agreement with previous studies on ULC steels.

After understanding the macroscopic kinetics of strain aging, the formation and propagation of Lüders bands are investigated experimentally by digital image correlation (DIC) and modeled using a constitutive model proposed in the literature with finite element method (FEM) simulations.

Finally, the strain aging response is reported for materials deformed along different deformation paths. Tensile samples were taken from cold-rolled sheet at different angles (0˚, 45˚ and 90˚) to the rolling direction. Following aging, the mechanical behaviors were compared. The very different responses observed are discussed in relation to work previously performed on

ULC steels as well as a new constitutive model that is more physically motivated compared to others in the literature.

Chapter 4: Experimental methodology

This chapter outlines the experimental procedure followed in this study. First, the material is characterized in terms of the as-received state. Then, sample design, annealing treatment, mechanical testing, aging treatment, and digital image correlation (DIC) procedures are discussed.

4.1 Material & annealing

A 1 mm thick cold-rolled ULC steel sheet supplied by ArcelorMittal Dofasco was used for this study. The nominal composition of this steel is displayed in Table 4.1. This steel presents very small amounts of Nb and Ti, leaving approximately 18 ppm of C and 23 ppm of N in solid solution. The estimation of free carbon/nitrogen was done using the following references [77], [78].

Table 4-1: Chemical composition of the ULC steel (wt%)

C	Si	N	P	Mn	S	Nb	Ti	V	Al(S)	Al (T)	Cr	Mo	Ni	Cu	Others
0.0024	0.011	0.0027	0.039	0.358	0.0084	0.0048	0.012	0.0029	0.037	0.042	0.043	0.003	0.023	0.037	0.0001

The starting material was received in a “full hard” (as cold rolled) state and thus it had to be annealed to achieve a fully recrystallized microstructure. Annealing was conducted in a box furnace, where the sample was inserted, and temperature was measured by a thermocouple welded to the sample`s surface. The annealing temperature was performed at 800˚C for a total heat treatment time of 7 min. It was found that it took approximately 2 minutes for the samples to reach 800˚C. After this heat treatment, each sample was air-cooled. The annealing temperature and time were selected to guarantee full recrystallization for the shortest possible annealing time and to ensure that the samples remained in the fully ferritic portion of the phase diagram. This helped to reduce the risk of decarbonization while also ensuring a grain size that would not impact on the strain aging response [39], [79], [80]. Samples were annealed individually with a minimum of 20 minutes interval between samples.

The final microstructure was analyzed by optical microscopy. Sample preparation included mounting followed by grinding using papers starting from 120 μm and ending at 1200 μm grit. Next, the samples were polished using 6 μm and 1 μm diamond paste. After grinding and polishing, samples were etched with 4% nital for 15 seconds.

Grain size measurement was performed using image-J version 1.52p. First, a micrograph was uploaded to the software, transformed into 8-bit, adjusted into autolocal threshold, and processed using skeletonize, find edges and fill holes tools before grain size analysis. Pictures were processed to allow the software to correctly identify the grains and grain boundaries. After analysis, the area of each grain was obtained and from this, the equivalent area diameter of each grain calculated.

4.2 Tensile samples and mechanical testing

Samples were produced from the as-received sheets by the waterjet cutting, the dimensions of these samples being shown in Figure 4.1. After being produced, the cross-sectional dimensions of each tensile sample within its gauge length (width and thickness) were measured ten times with a digital micrometer, and the average value was used to compute the gauge length cross-section area. It is important to notice that the dimensions of the samples shown in Figure 4.1 are not those of the ASTM standard[81]. The sub-sized samples used here were selected to allow for samples to be cut at different angles from the cold-rolled sheet produced at UBC. Though these samples are non-standard, they have been used routinely within the microstructure group at UBC.

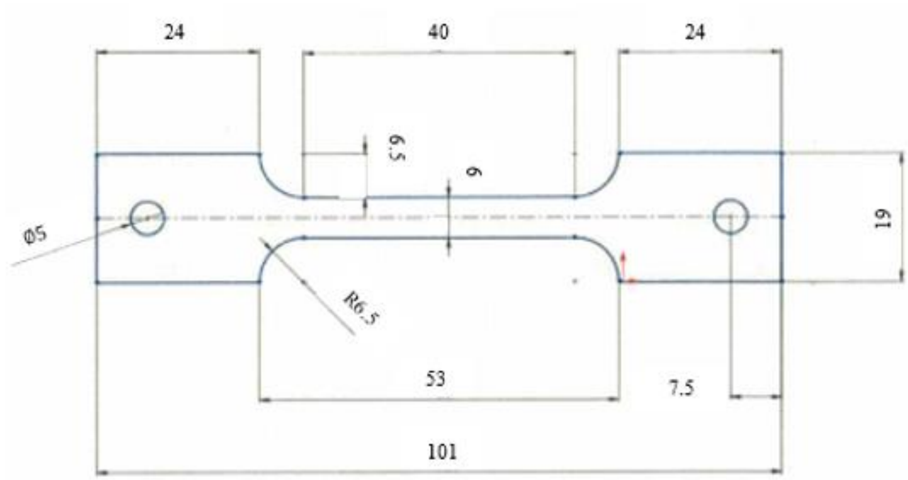

Figure 4-1: Schematic illustration of tensile test specimens used in this study. All dimensions are given in millimeters.

A screw-driven Instron tensile machine (Figure 4.2) was used to perform all of the tensile tests in this study. The load was measured by a 5KN load cell, and displacement on the sample by a 12.5 mm gauge length extensometer attached to the center of the tensile sample's gauge length. The tensile test data, load, and displacement were computer recorded during each test at a rate of 40 Hz. Before starting a test, both load and strain were calibrated using built-in calibrations.

Each test was started manually with a fixed imposed cross-head speed. For all of the testing performed here a cross-head speed of 0.21 mm/s was selected. Based on the gauge length of the samples used, this corresponds to an applied strain rate of approximately $6\ x\ 10^{-2}\ s^{-1}$. To stop a test at a specific level of strain, the displacement of the extensometer was used. During pre-straining, samples were targeted to be deformed to 10% strain prior to unloading. This corresponded to an extensometer displacement (assuming zero initial displacement of the extensometer) of 1.25 mm. When the displacement of the extensometer reached this value, the direction of loading was manually switched so as to unload the sample. It was found that this could be achieved to within a strain (displacement) of $\pm 1\%$ (± 0.125 mm).

A pre-strain of 10% was selected based on a couple of criteria. First, if a pre-strain level less than 10% had been chosen then it would have risked unloading the sample prior to the onset of uniform plastic deformation prior to the end of the yield point elongation. Second, it was found that 10% plastic pre-strain, being comparable to strain levels experienced in sheet forming [2], allowed for comparison against data already in the literature [2], [19].

At the end of each tensile test, the recorded force (KN) and displacement (mm) data were converted to engineering stress-strain data. Each condition examined was tested a minimum of two times to ensure the reproducibility of the test results.

Figure 4-2: The screw driven Instron tensile load frame equipped with 5 KN load cell used for all tensile tests in this thesis.

4.3 Aging treatment

Aging treatments were performed on samples immediately following pre-deformation. The delay between the tensile tests and aging treatment was no longer than 10 min. In the case of the cold-rolled samples, a longer delay had to be managed as the cold-rolled sheet had to be taken to the machine shop and aging could not take place until the samples were prepared. A full discussion of the various tests made to ensure reproducibility, in this case, will be reserved until

Chapter 5. Aging temperatures and times varied between 50˚C to 150˚C and 10 seconds to 220 minutes for samples pre-deformed in tension. In the case of the cold-rolled materials only aging at 150˚C for 10 min was used. Aging was performed in a stirred oil bath containing silicon oil. The bath temperature was monitored continuously by an immersed K-type thermocouple. Following aging, all samples were quenched into room temperature water and subsequently cleaned with water and soap to remove oil.

4.4 Cold rolling

Samples for cold rolling were cut from the received sheet by waterjet cutting. Specifically, two different rectangular samples were produced to allow tensile samples to be machined at different directions after cold rolling tests (Figure 4.3). Also, rectangular samples dimensions were limited by the size of annealing treatment furnace (box furnace), aging station and cold rolling machine.

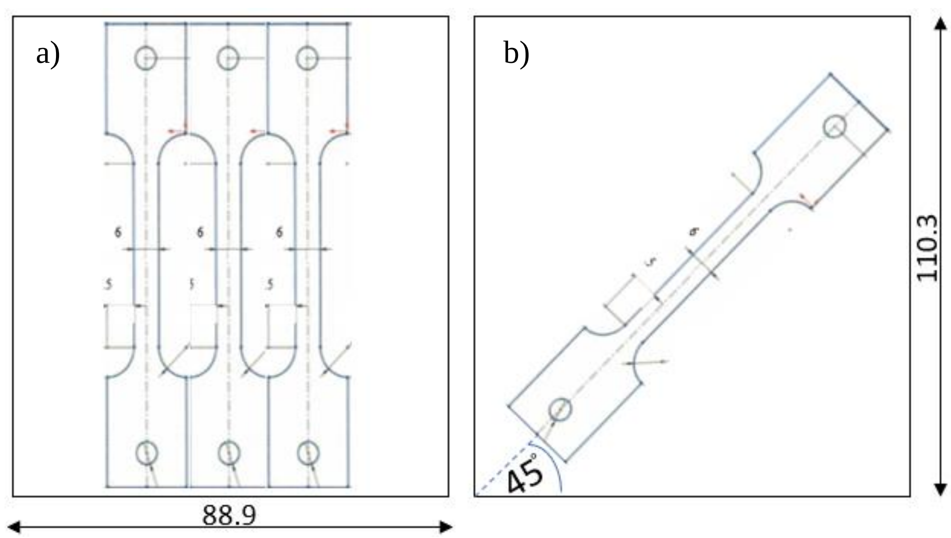

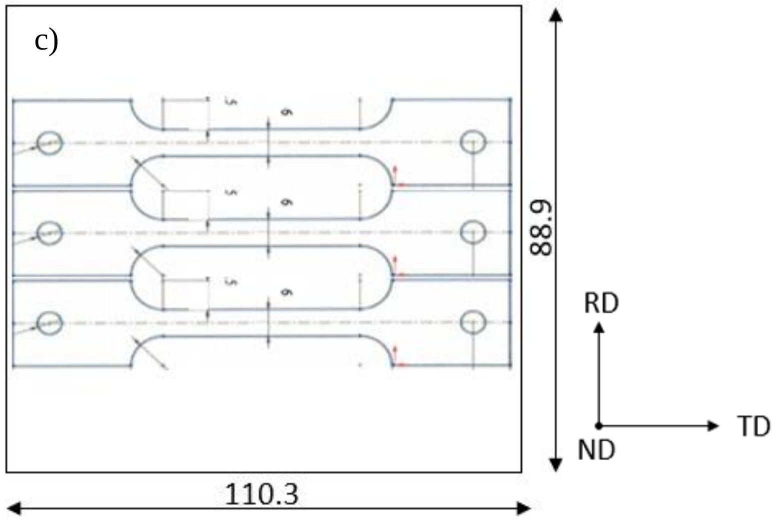

Figure 4-3: Represents cold rolling samples different dimensions in millimeters. First dimension is applied for tensile samples cut at a) 0˚, b) 45˚ from RD, and second dimension for samples cut at c) at 90˚ from RD, after cold rolling and aging.

The rolling mill used had rolls with a diameter of 170 mm. The material was cold-rolled in the same rolling direction as that of the as-received condition. The reduction in thickness was measured using a digital micrometer, and a total reduction of 9% $\pm$ 1% was reached by rolling in 4-5 to passes. In this work, the first two passes were subjected to greater plastic deformation, and the last passes slightly plastic deformed.

4.5 Digital image correlation (DIC)

DIC is an experimental technique for the non-contact measurement of full-field displacements that can be used for the study of heterogeneous displacement and strain fields [82]–[84]. The basic idea of DIC is that a random (speckly) pattern on the surface of a specimen is tracked over a sequence of images taken (in this case) during testing. In the study performed here, the speckle pattern was created by coating the sample surface with a matt white paint followed by using an airbrush to distribute a random pattern of fine black dots [82]. During tensile deformation, pictures were taken from a single camera (1380 x1035 pixels) located directly in front of the sample. LED lighting was used to uniformly light the sample surface. The distance between the camera and the sample was fixed and the field of view focused on the gauge section of the sample. The frequency of image acquisition was 9 pictures/second. The load from the load cell was imprinted onto each image so that a load-displacement (and eventually stress-strain) curve could be reconstructed from this data.

Following testing, the LAVISION DIC software [85], [86]was used to perform image processing so as to obtain displacements and to obtain strains on the sample surface. The basic steps required to obtain these strains were: (1) define the desired area of analysis, (2) select a seeding point and (3) choose the appropriate subset size and step size. Details of the various parameters selected will be discussed further in chapter 6.

Chapter 5: Macroscopic behavior of ULC steels

This chapter's goals are to quantify the kinetics of strain aging in a ULC steel under monotonic tensile test conditions and to use the results to develop an analytical model to predict the upper yield stress and lower yield stress. This model will then be used in Chapter 6 to predict the overall stress-strain response.

5.1 Annealing and pre-straining samples

The as-received material was in a cold-rolled state having been subjected industrially to a total of 76% reduction. This results in the microstructure presented in Figure 5.1. Annealing was performed on the as-rolled material to remove the effects of the cold rolling, increasing ductility, and decreasing hardness.

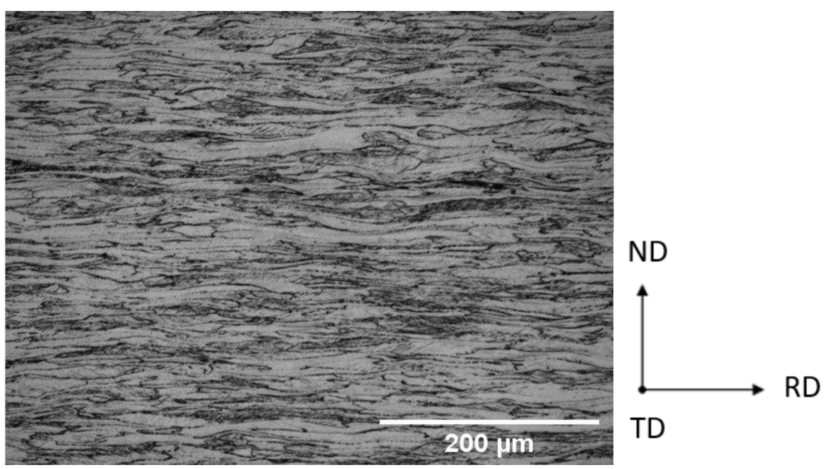

Figure 5-1: Optical micrograph showing the microstructure of the as-received ULC steel sheet. The grains are seen to be highly elongated parallel to the prior rolling direction (RD).

It was found that annealing for 7 min in an 800^{o}C furnace was enough to result in a microstructure containing equiaxed grains indicating recrystallization (Figure 5.2). To optimize annealing, several samples were annealed in the same furnace at the same time. To make sure that variations in furnace temperature did not influence the final recrystallization, the homogeneity of the microstructure was checked across the entire length of the gauge section of samples (Figure 5.2). The final grain size was measured after full recrystallization using Image-J and an equivalent circular area diameter. Approximately 7000 grains were measured, and the mean grain size was found to be 14 µm. This mean grain size was calculated using an area fraction weighted average of the diameter [87]. Figure 5.3 shows the grain size distribution obtained from these measurements.

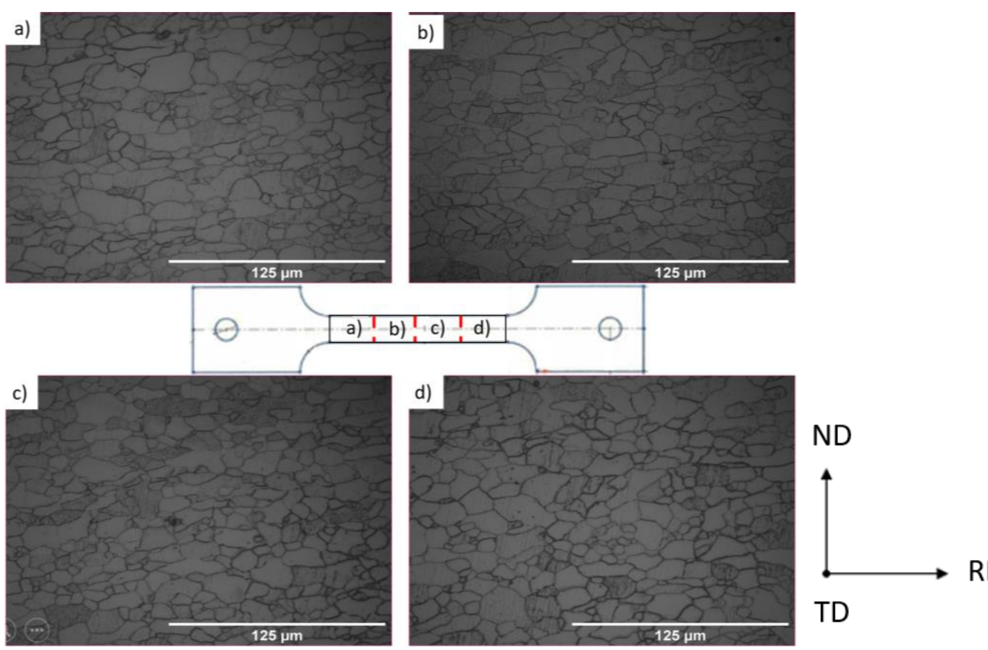

Figure 5-2: Microstructure observed at different positions along the gauge length of a tensile sample from one shoulder to the other shoulder after annealing for 7 minutes at 800ºC. No variation in microstructure was observed indicating full recrystallization along the entire length of the sample.

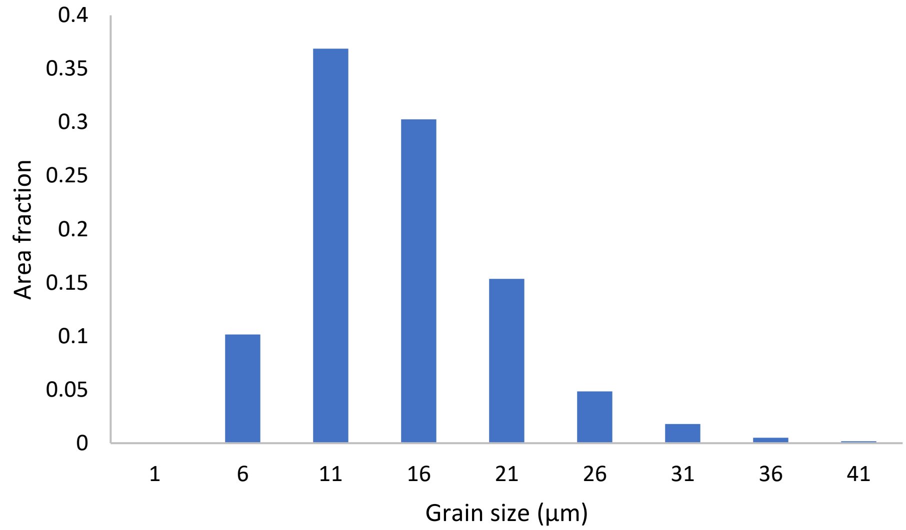

Figure 5-3: Grain size distribution obtained from a fully recrystallized sample after annealing at 800^{o}C for 7 minutes. To construct this histogram 7000 grains were sampled.

As a final check on the suitability of the annealing conditions, the mechanical response following annealing was obtained in tension. Figure 5.4 illustrates the difference in mechanical behavior between the as-received sample and annealed sample. Samples tested after annealing presented an upper and lower yield stress, and yield point elongation. The flow stress was reduced, and ductility increased relative to the as-received material. The annealed sample shows a behavior (yield strength, uniform elongation) similar to that reported for other recrystallized ULC steels in the literature [48], [88].

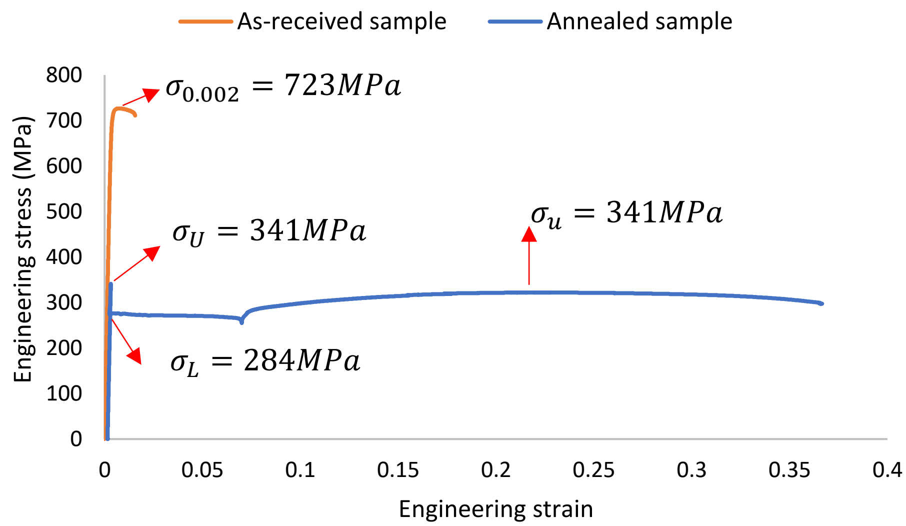

Figure 5-4: Stress-strain curve of ULC steel in an as-received condition and following recrystallization annealing. Where σ_U, σ_L, $\sigma_{0.002}$ and σ_u are lower yield stress, upper yield stress, stress at 0.2% deformation, and ultimate stress, respectively.

As noted in section 4.2, each sample studied here was pre-strained to 10% tensile strain prior to aging. This provides an opportunity to check the success of the annealing on each sample tested as the pre-deformation stress-strain response can be compared. Figure 5.3 shows all pre-straining tests performed superimposed on the same graph.

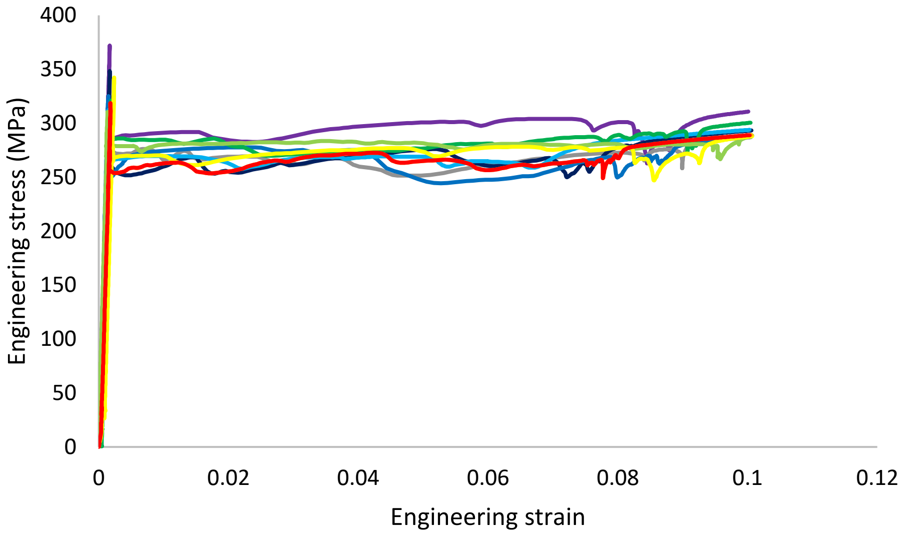

Figure 5-5: Engineering stress-strain diagram for several tensile tested samples illustrating the reproducibility of the annealing for recrystallization.

Overall the results show very good reproducibility in terms of the upper yield point, lower yield stress and yield point elongation. The test-to-test differences in behavior could be related to small differences arising from tensile sample fabrication or pre-loading of samples [37], [38], [89]. Furthermore, the accuracy of capturing the upper yield point may have been affected by the limited data sampling rate (40 Hz) used in these tests.

Another important result that can be assessed from the data in Figure 5.5 is the ability to end the tests at 10% pre-strain. As mentioned above, this was done manually and so could not be controlled to better than ~ +/- 1% strain. Figure 5.6 shows the distribution of flow stresses at the end of pre-straining (at ~ 10% strain) for each sample in Figure 5.5. The mean stress was found to be 301 MPa and the standard deviation 6 MPa. This indicates that 68% of the samples were pre-strained to stresses of between the narrow range of 295 MPa and 307 MPa. This small difference is not expected to be enough to lead to major differences in aging behavior.

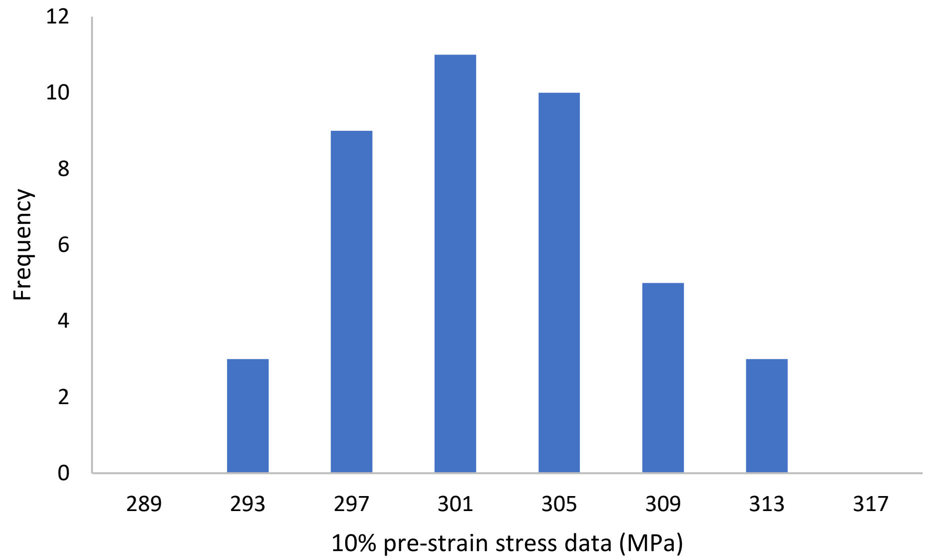

Figure 5-6: The flow stress measured just prior to unloading (at ~10% strain) for each sample studied here. The mean was 301 MPa with a standard deviation of 6 MPa.

5.2 Strain aging measurement

After pre-straining, samples were aged at different temperatures (50 ^oC, 100 ^oC, and 150^oC) and times before being reloaded again in the same direction. Strain aging led to an increase in the flow stress with increasing temperature and time as illustrated in Figure 5.7 and Figure 5.8. In the first figure, the influence of temperature was evaluated by increasing temperature for a given time, while the second figure evaluated the effect of time by increasing aging time for a fixed temperature.

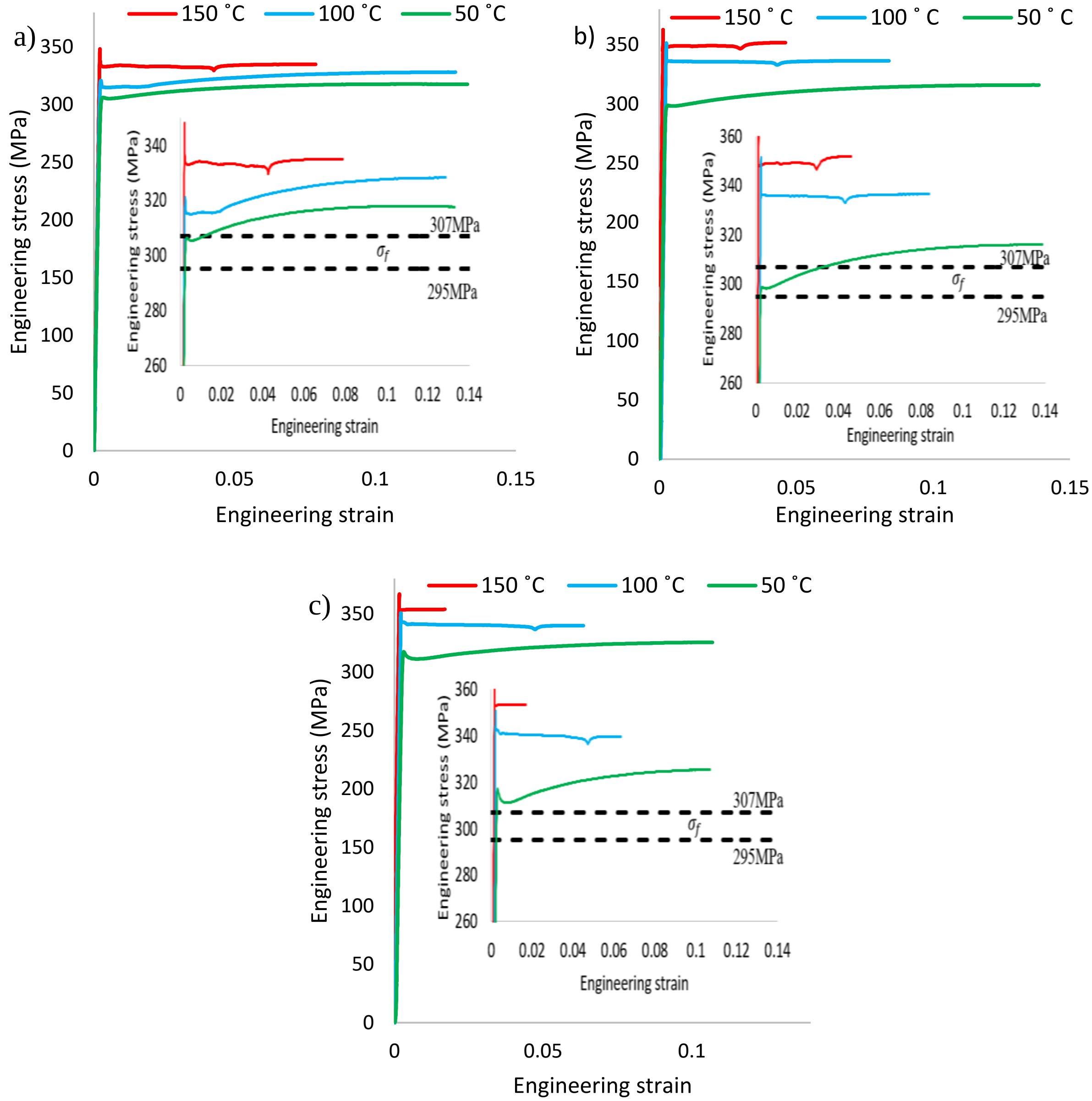

Figure 5-7: Illustration of the effect of aging temperature on strain aging and flow stress of ULC steels by increasing the aging temperature for a fixed aging time of a)1min, b)5min, and c)10min. The smaller figures are zoomed regions, and σ_f is the last load before unloading and aging which varies between 307 MPa and 295 MPa.

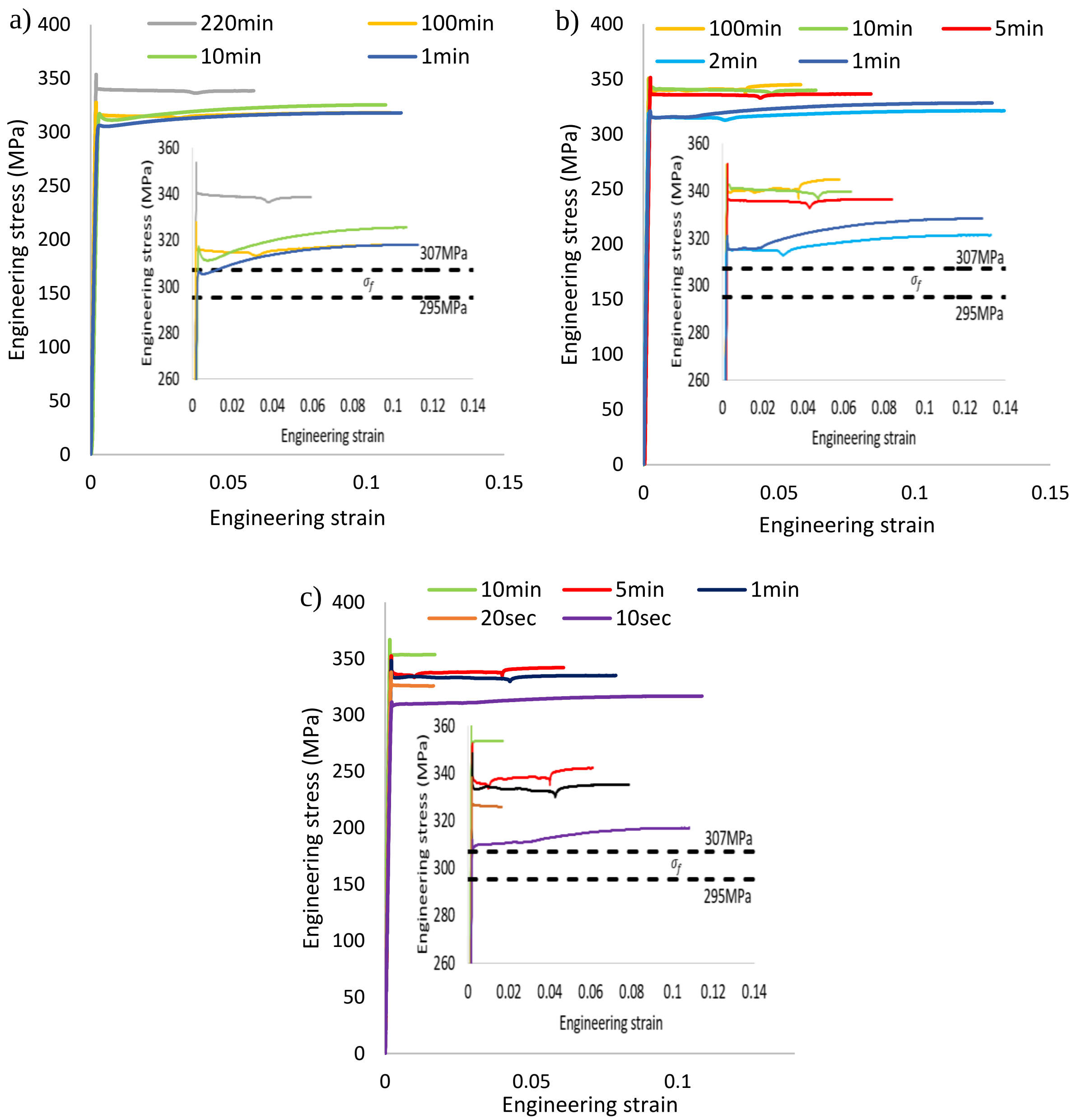

Figure 5-8: Illustration of the effect of aging time on strain aging and flow stress of ULC steels by increasing aging time for a fixed aging temperature of a)50˚C, b)100˚C, and c)150˚C. The smaller figures are zoomed regions, and σ_f is the last load before unloading and aging which varies between 307 MPa and 295 MPa.

All tests displayed the expected increase in yield stress, reappearance of upper yield and lower yield stress, and yield point elongation. Upper and lower yield stresses rose with aging temperature and time, which is expected since the amount of segregation of solute atoms to dislocations increases with time and the kinetics will increase with temperature as described by the Cottrell and Bilby model [23]. For instance, a sample aged at 50˚C takes about 220 minutes to increase 43MPa in yield stress, while a sample aged at 150˚C for 1 minute has its yield stress increase by 50MPa.

Although, the increase in yield point elongation (ε_L) with aging temperature [90] [91], and yield drop ($\sigma_U - \sigma_L$) [92] have been reported in the literature, the present work, did not find any clear relationship between them (Figure 5.9). The possible reasons for that are: (1) yield point elongation measurement can be a challenge especially if the Lüders band travels outside of the region covered by the extensometer and (2) difficulty of getting the right upper yield stress during the tensile test due to the limited data acquisition rate.

Finally, a permanent increase in flow stress was noticed after strain aging by comparing the lower yield stress and ultimate tensile stress of all aged samples. The increase of flow stress and ultimate tensile stress with strain aging has been reported in the literature [18]. Figure 5.10 illustrates a close linear relationship between the ultimate tensile stress and lower yield stress. In a similar way, the ultimate tensile stress increases with the upper yield stress.

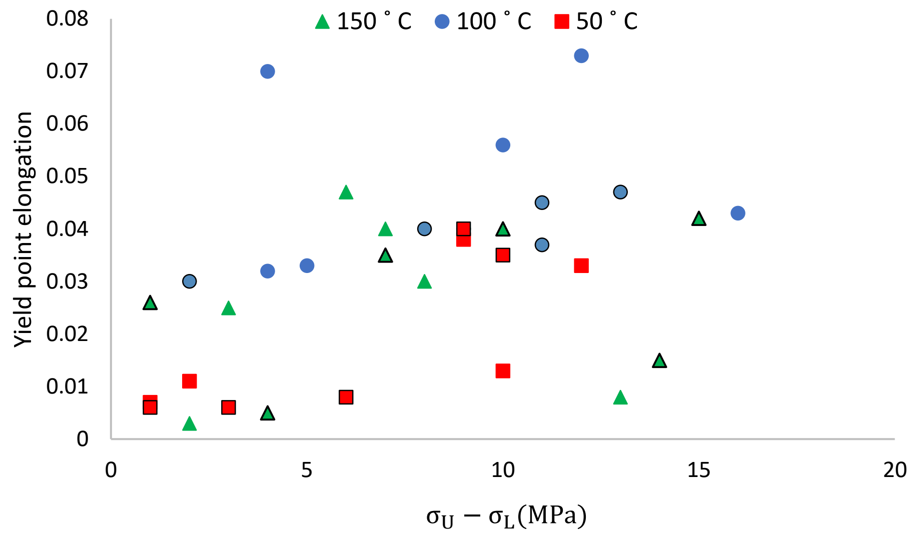

Figure 5-9: Relationship between yield point elongation and yield drop for ULC steels aged at different aging temperatures. Verification tests for each aging temperature are contoured in black.

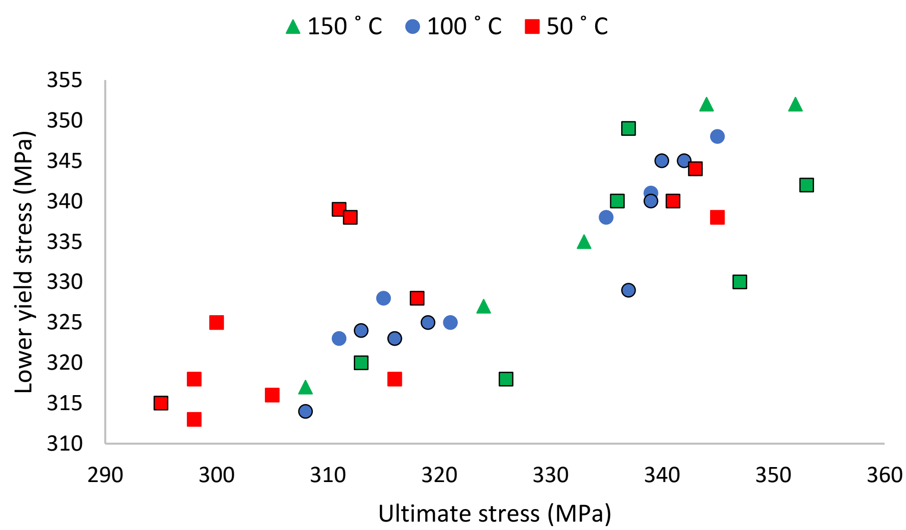

Figure 5-10: Illustrates the approximately linear relationship between the lower yield stress and the ultimate tensile stress for different aging conditions. Second verification tests for each aging temperature are contoured in black.

Following previous work [2], [19], [48], the effect of strain aging will be specifically associated with the increase in yield stress in this chapter. This can be measured in two ways:

1) The difference between the upper yield stress and the stress at the point of unloading from pre-loading ($\Delta\sigma_U$)
2) The difference between the lower yield stress and the stress at the point of unloading from pre-loading ($\Delta\sigma_L$)

These parameters are plotted in Figure 5.11.

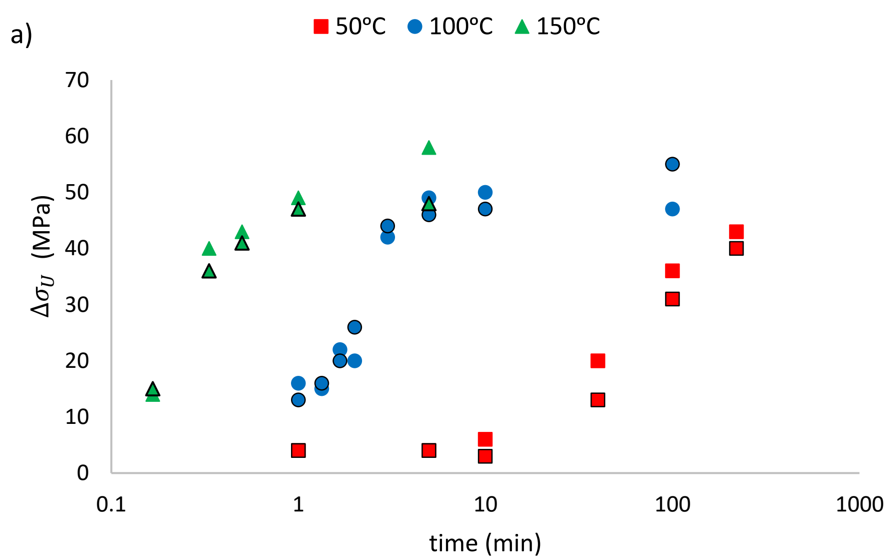

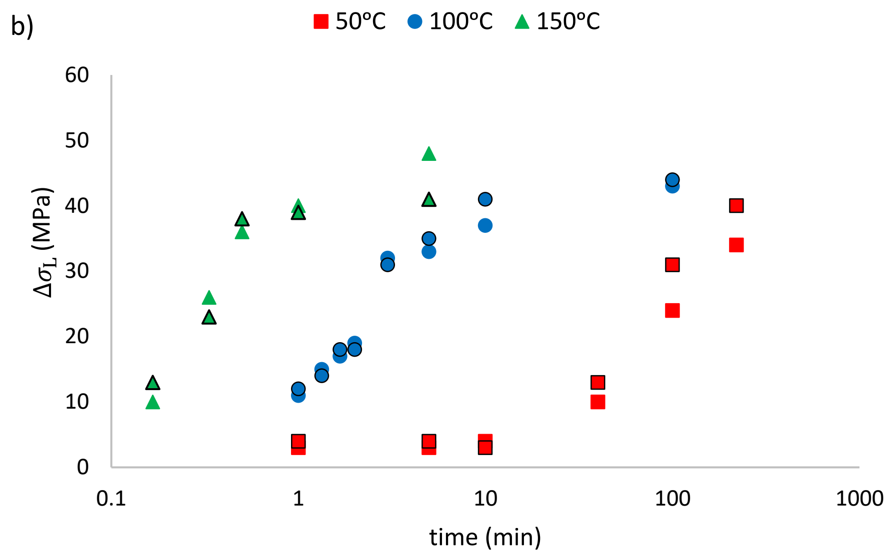

Figure 5-11: The increase in yield stress following strain aging measured using a) the upper yield stress and b) the lower yield stress. Second verification tests for each aging temperature/time are contoured in black.

Figure 5.11 clearly shows the expected increase in yield stress with time and temperature as well as the fact that the strain aging effect saturates, i.e. the yield stress (upper and lower) does not continue to increase beyond a certain limit with further aging, this being independent of the aging temperature. This maximum increase in yield strength during aging is termed $\Delta\sigma_{max}$, and in this work a maximum increase in both upper ($\Delta\sigma_{Umax}$) and lower yield stress ($\Delta\sigma_{Lmax}$) are obtained. These parameters are obtained by averaging the maximum values for each of the methods for the highest temperatures, i.e. the maximum values of $\Delta\sigma_U$ and $\Delta\sigma_L$ for 100ºC and 150ºC treatment. In this case, the 50º C aging treatment data were not used because saturation was not clearly reached. Therefore, the saturation stresses are approximated to $\Delta\sigma_{Umax} =$

$55MPa$ and $\Delta\sigma_{Lmax} = 45\ MPa$, this result being very similar to values reported in the literature for similar steels and aging conditions [48][19].

5.3 Modeling strain aging effect in ULC steels

It was shown in the Literature Review (Chapter 2) that one of the successful models for predicting the evolution of yield stress with strain aging is the Louat modification of the Cottrell-Bilby model [33]. This model (equation 2.13) was used to fit the experimental data presented in Figure 5.11. Taking logs on both sides of equation 2.13 we arrive at,

$$\ln\left(\frac{\Delta\sigma_{max} - \Delta\sigma}{\Delta\sigma_{max}}\right) = \left(-\frac{t}{t^*}\right)^{\frac{2}{3}} \qquad (5.1)$$

In this case, if we plot our data as the natural logarithm of the normalized increase in yield stress (left-hand side of equation 5.1) versus $t^{\frac{2}{3}}$ then the data should fall on a line having a slope of $\left(-\frac{1}{t^*}\right)^{\frac{2}{3}}$.

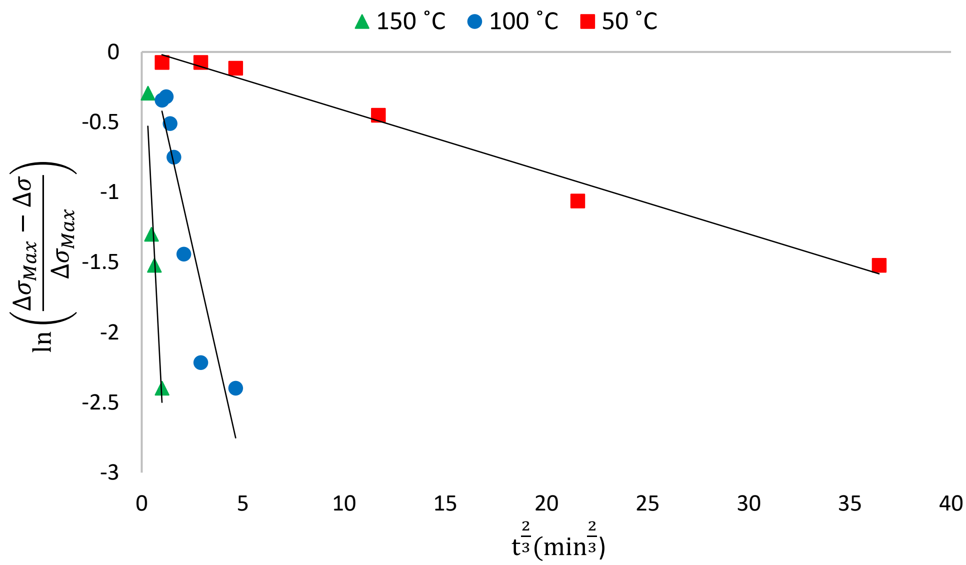

Figure 5-12: Logarithm increase in yield strength with $t^{\frac{2}{3}}$ for different temperatures using upper yield strength experimental data.

Figure 5.12 shows that this linear behavior is well reproduced by the data collected here. As expected, this plot shows that t^* is a function of the aging temperature. This is due to the fact that $t^{*\frac{2}{3}}$ is dependent on binding energy (A) and diffusivity of carbon (D) according to $t^{*\frac{2}{3}} = \left(\frac{KT}{AD}\right)^{\frac{2}{3}} . \frac{1}{3Co\lambda} . \left(\frac{2}{\pi}\right)^{\frac{1}{3}}$ (cf. eq 2.11 and 2.13). Thus, one should expect a relationship between $t^{*\frac{2}{3}}$ and $\left(\frac{1}{D}\right)^{\frac{2}{3}}$. From the slopes obtained from a linear fit to the data in Figure 5.13, values of $t^{*\frac{2}{3}}$ were deduced and plotted as a function of $\left(\frac{1}{D}\right)^{\frac{2}{3}}$ where $D = Do \exp\left(-\frac{Q}{KT}\right)$, with $Do = 1.2x10^{-4} \left(\frac{m^2}{min}\right)$ and Q = 85 $\left(\frac{KJ}{mol}\right)$ is the diffusivity of carbon in BCC iron [16], Although only 3 temperatures (giving three values of $t^{*\frac{2}{3}}$) were studied here, a fourth data point can be added knowing that as the diffusivity goes to infinity (and so $\left(\frac{1}{D}\right)^{\frac{2}{3}}$ goes to zero) t^* should go to zero.

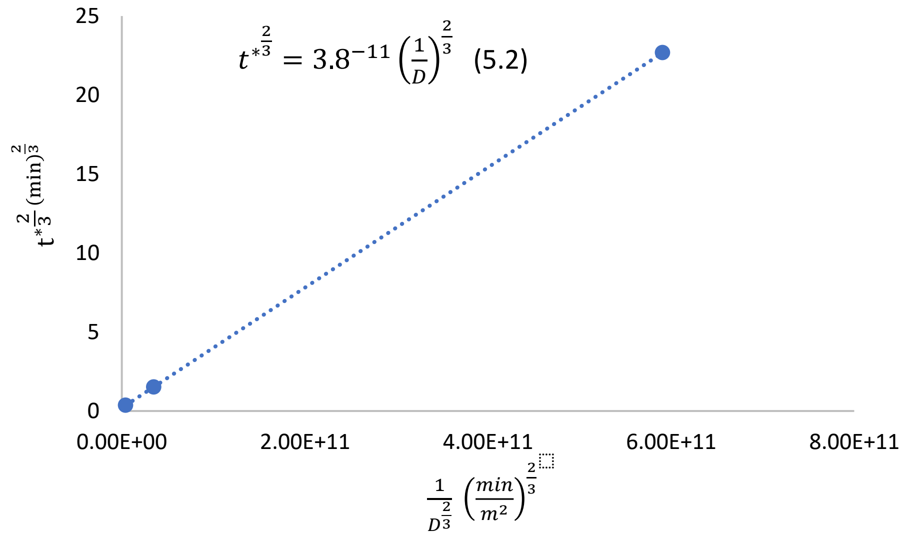

Figure 5-13: Linear relationship between $t^{*\frac{2}{3}}$ and $\left(\frac{1}{D}\right)^{\frac{2}{3}}$ using data from Figure 5.12 for samples aged at 50˚C, 100 ˚C and 150 ˚C.

The model appears to well fit the experimental data with $t^{*\frac{2}{3}} = 3.8^{-11}\left(\frac{1}{D}\right)^{\frac{2}{3}}$, where 3.8^{-11} refers to $\left(\frac{KT}{A}\right)^{\frac{2}{3}}.\frac{1}{3Co\lambda}\left(\frac{2}{\pi}\right)^{\frac{1}{3}}$ in units of $m^{\frac{4}{3}}$, as $\left(\frac{1}{D}\right)^{\frac{2}{3}}$ is in units of $\left(\frac{min}{m^2}\right)^{\frac{2}{3}}$, $t^*$is given in minutes. This relationship allows one to predict the upper yield stress. Applying the same method to the data for the lower yield stress results allows one to predict the lower yield stress.

$$t^{*\frac{2}{3}} = 4.2^{-11}\left(\frac{1}{D}\right)^{\frac{2}{3}} \qquad (5.3)$$

Figures 5.14 shows the experimental data from Figure 5.11 but now with the model fits (equation 2.13) with t* given by equations 5.1 and 5.2. One can see that the fit to the data is very good. This provides the opportunity to interpolate to other aging times and temperatures. To illustrate this an extra set of experimental measurements made at 70^{o}C were performed and the model used to predict their response (Figure 5.14).

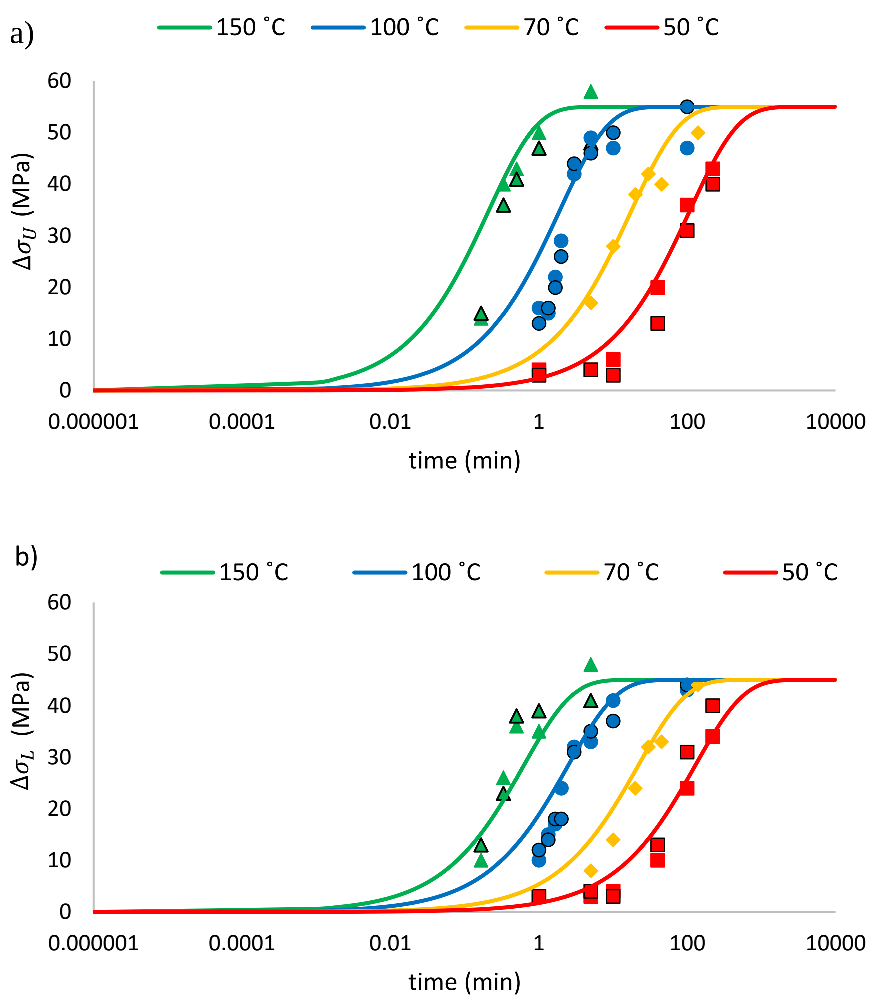

Figure 5-14: Kinetics of ULC steel using a) upper yield point (method 1) and b) lower yield point (method 2). Second verification tests for each aging temperature/time are contoured in black.

While the model does a good job of reproducing the experimental data, it is important to point out that it is based on assumptions. First, only the diffusion of carbon is considered in this model. As discussed above, nitrogen could also play a role in strain aging [23]. One justification for this assumption is the fact that carbon and nitrogen have very different diffusivities in ferrite. For instance, at room temperature, the diffusivity of carbon is $3x10^{-17} cm^2/s$, while nitrogen has a diffusivity of $1x10^{-16} cm^2/s$ [25]. Thus, it is expected that carbon diffusion, which presents the lower diffusivity, controls the kinetics of aging at low temperatures and short times.

A second assumption here is that only the first stage of strain aging effect is considered. In previous models, considered to longer aging times, the effect of carbide precipitation on the yield strength has also been considered [3], [28]. In previous work on ULC steels, De Comman et al. [16] showed no effect of carbide precipitation during strain aging for conditions similar to those studied here. The effects of carbide precipitation are typically seen to appear after saturation of the first stage of strain aging [3], [16], [24], this occurring after longer times than those studied here.

5.4 Summary

In this chapter, experimental strain aging data was obtained, and a model was parameterized to describe the increase in upper and lower yield stress. The results were shown to be comparable to previous studies in the literature. This model will next be used in chapter 6 as part of a constitutive model with a finite element model to allow for the prediction of both yield strength and working hardening response following aging.

Chapter 6: Prediction of the stress-strain response of ULC steels

6.1 Introduction

The goal of this chapter is to predict both the yielding and work hardening behavior of the ULC steel studied here. To do this, a finite element model is developed and coupled with the analytical model presented in Chapter 5 and a constitutive law that allows one to predict not only strain aging effect on yield stress but also the macroscopic and mesoscopic mechanical behavior of ULC carbon steels. A VUHARD subroutine was used to describe the plastic response of the material (Appendix A). The FEM predicted stress-strain curves are compared to tensile test data, while the predicted distribution of strain during Lüders band propagation are compared to digital image correlation (DIC) measurements.

6.2 Description of Abaqus model

When a material deforms homogeneously by plastic deformation, a constitutive law alone can predict the mechanical behavior during a tensile test. However, when a material deforms heterogeneously, for example during the portion of the stress-strain curve associated with yield point elongation of ULC steels, a constitutive law needs to be used together with a numerical (e.g. FEM) model to predict the macroscopic tensile response.

Simulations were performed in this thesis using an explicit, 3D finite element model in ABAQUS CAE version 6.14. The element type was defined as linear element (8-node brick, C3D8R). The material was assumed to be elastically isotropic (Young's modulus = 200 GPa and Poisson's ratio = 0.3) with a density of $7870\ kg.m^{-3}$. The constitutive law describing the plastic response of the material (see description below) was implemented via a VUHARD subroutine developed as a part of this thesis (See Appendix A for the VUHARD routine).

Boundary conditions were defined to reproduce the conditions expected in the experimental tensile test. The surface nodes on one of the grip sections were constrained to no displacement/rotation (encastre condition). The second grip section had boundary conditions applied to the surface nodes allowing for only motion in the y-direction (direction of tensile testing), i.e. deformation is controlled by displacement in y-direction. In this work, displacement was set to $4.03x10^{-3}$ mm/step for both loading and reloading simulations. The surface of the gauge section of the sample was subjected to no mechanical constraint, allowing for those surfaces to behave as free surfaces (zero stress in the x and z directions).

A slight geometrical imperfection was introduced in the upper-left filet portion of the finite element model (Figure 6.1). This was implemented to ensure that Lüders band formation occurred consistently at the same location. The chosen imperfection caused a local perturbation of the cartesian coordinates introducing extra stress concentration. This creates a defect with a shape similar to a v-shaped notch and dimensions of 0.09 mm (length), 0.02 mm (width) and 1 mm (thickness). The stress-strain response of this model was compared to a free defect model using the local behavior constitutive law presented later in this chapter, and the mechanical behavior was found to be not affected by the presence of this small defect.

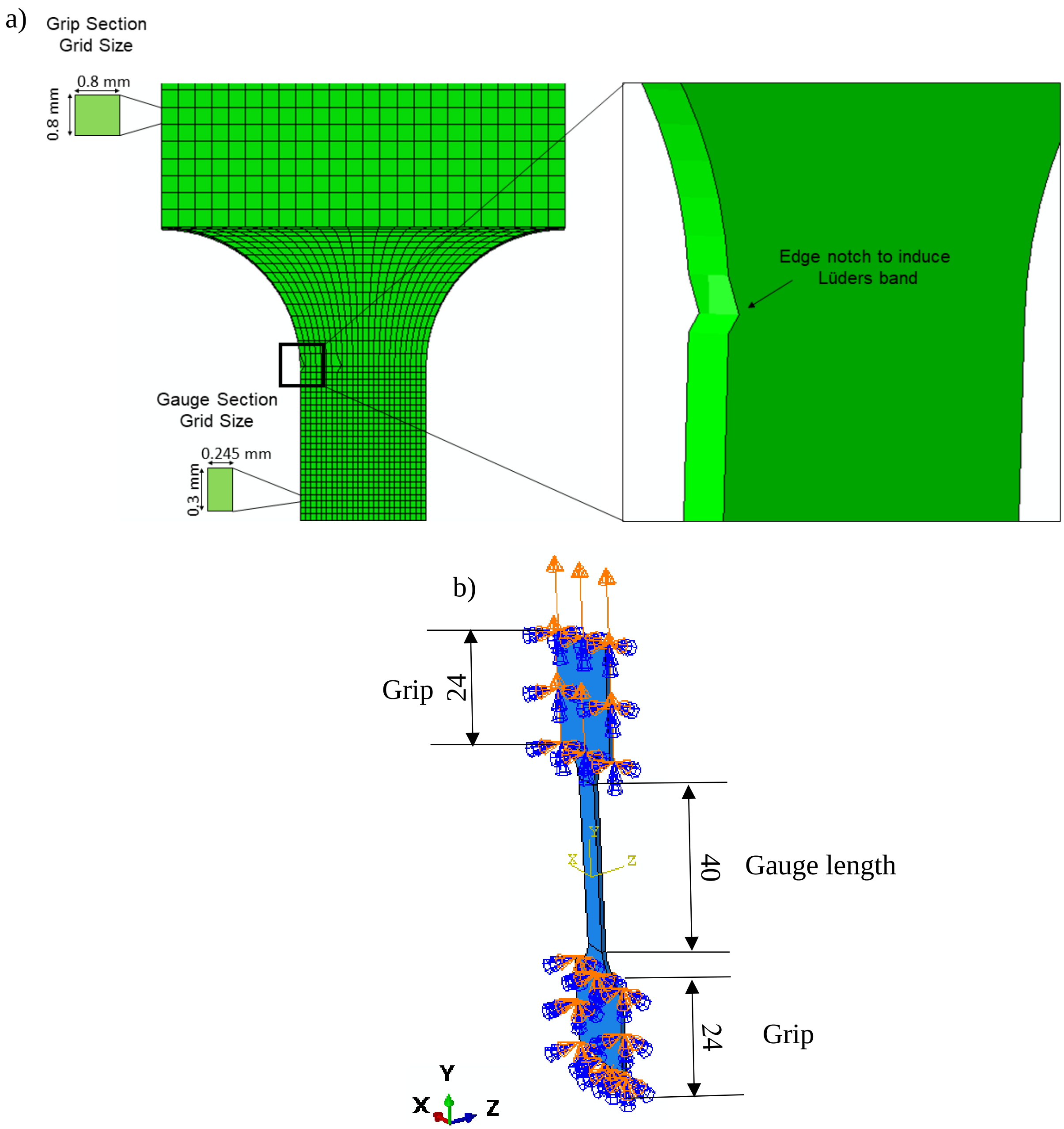

Figure 6-1: Illustration of a) mesh size in the grip section and gauge section, and a notch introduced at the sample shoulder, and b) the boundary conditions used in the model. In b) the blue marks mean no rotation is allowed in the specific direction, orange marks mean no displacement is permitted in the given direction, and the orange arrow indicates that displacement in y-direction is allowed in this model. Units are in millimeters.

The 3-D meshed specimen was designed to have the same dimensions as those of the experimental tensile sample (Figure 4.1). The model's gauge length was meshed with a finer mesh size than the grips so as to better resolve the localized plastic strain induced by the Lüders band. Finally, the tensile stress-strain curves were calculated by averaging the stress and strain at all the nodes in the gauge section of the sample. To do this the true stresses and strains in the y-direction were considered.

6.3 Constitutive law

In Chapter 2 (section 2.10) a constitutive model was presented that allows one to predict (in connection with FEM calculations) the stress-strain response of steels that exhibit Lüders band formation and propagation. More specifically, $\sigma = \sigma_{max} + Q_1.\left(1 - e^{-b_1.\varepsilon_p}\right) + Q_2.\left(1 - e^{-b_2.\varepsilon_p}\right)$ was used to fit the mechanical behavior of ULC samples measured in tension directly after annealing (the results shown in Figure 5.4). Where the σ_{max} is equal the experimental σ_U (327 MPa), and the terms Q_1, b_1, Q_2 and b_2 are fitting parameters that allows one to obtain σ_{min}, and at least three other points during work hardening of the experimental data (Figure 6.2). The experimental lower yield stress is calculated by $\sigma_L = \sigma_{mn} + [(\sigma_{max} - \sigma_{min})/2.5]$. The parameters Q_1, b_1, Q_2 and b_2 used in this work are shown in Table 6.1.

Table 6.1: Displays the parameters used on the constitutive law during loading (eq 2.18).

$Q_1(MPa)$	b_1	$Q_2\ (MPa)$	b_2
345	14.5	-248	43

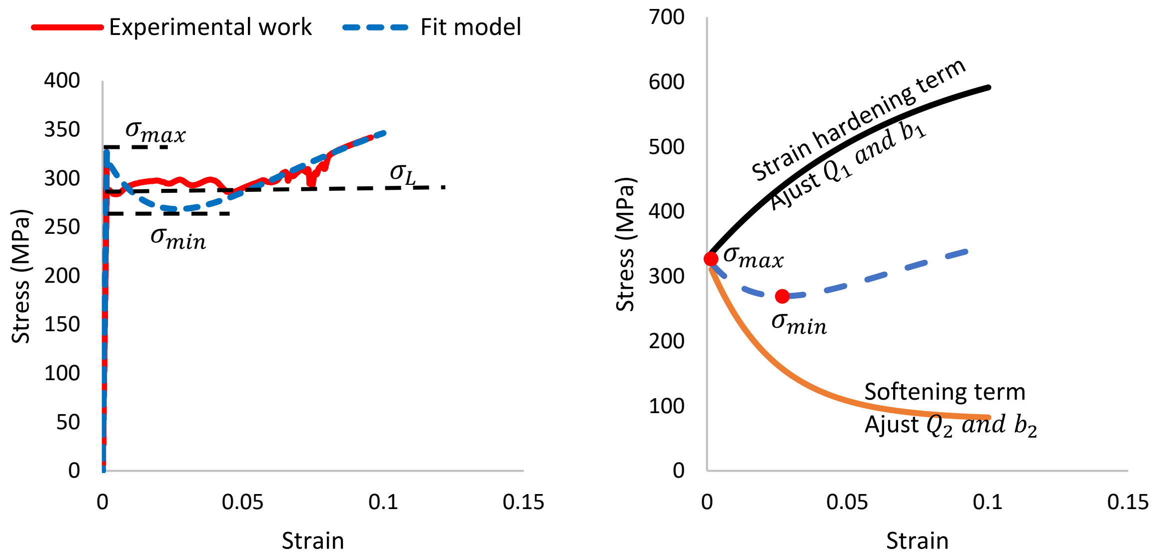

Figure 6-2: Fitting the constitutive model into the experimental data of the tested after annealing sample.

To account for the mechanical response following strain aging, the expression given in equation 2.20 is used where the parameter Q_{BH} was calculated from $\Delta\sigma_{\varepsilon_p=\varepsilon_L} = R_{BH} + Q_{BH}$, where R_{BH} is a parameter that determines the value of the upper yield point. This is taken, following the literature, to be a linear function of $\Delta\sigma_U$, i.e. $1.6\Delta\sigma_U$ [24]. Here $\Delta\sigma_{\varepsilon_p=\varepsilon_L}$ (Figure 6.3) is the difference in flow stress measured between the aged ($\sigma_{a_{\varepsilon_p=\varepsilon_L}}$) and unaged tensile sample ($\sigma_{n_{\varepsilon_p=\varepsilon_L}}$) at the end of the yield point elongation (ε_L). The value of $\sigma_{a_{\varepsilon_p=\varepsilon_L}}$ was approximated to the lower yield stress (σ_L) of the aged sample and calculated using equation 5.3

developed in chapter 5. The value of $\sigma_{n_{\varepsilon_p=\varepsilon_L}}$ was obtained from a tensile sample tested without interruption. For this work the value of $\sigma_{n_{\varepsilon_p=\varepsilon_L}}$ was taken to be 362 MPa. Therefore, Q_{BH} was set as $\sigma_L - 362 - R_{BH}$ and b_{BH} is calculated using equation 2.21. Figure 6.3 shows a schematic that highlights the relationship between these model parameters and the features on the stress-strain curves.

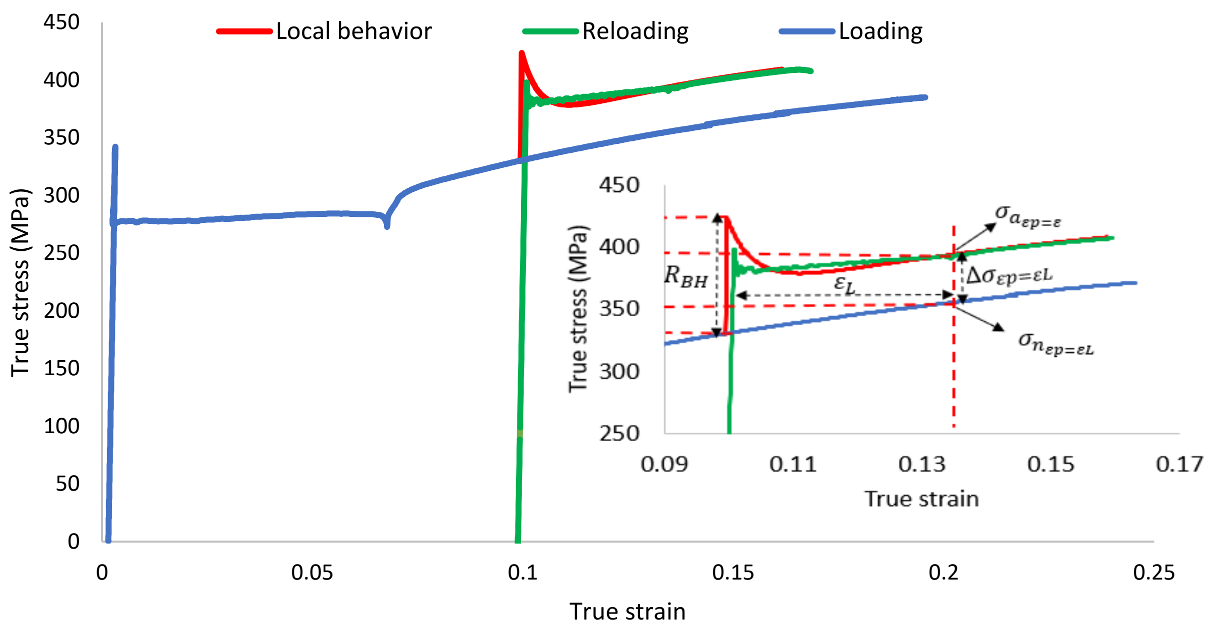

Figure 6-3: Schematic representation of the local behavior parameters where $\sigma_{a_{\varepsilon p=\varepsilon}}$ is calculated using equation 5.3 and $\sigma_{n_{\varepsilon p=\varepsilon L}}$ was fixed to 362 MPa.

It is important to note that in this constitutive equation strain rate sensitivity is not explicitly incorporated. It is expected that strain rate sensitivity could play an important role at the mesoscopic scale given the much higher strain rate in the Lüders band front compared to that imposed macroscopically. The consideration of rate sensitivity is, however, left for future work.

6.4 Sensitivity analysis

It is known that several aspects of the finite element calculation can affect the predictions it makes. Two important ones, in this case, are the mesh size [73], [76] and the time step used [93]. The effect of the mesh size used in the gauge section of the sample on the stress-strain response was checked by varying it, the results being shown in Figure 6.4.

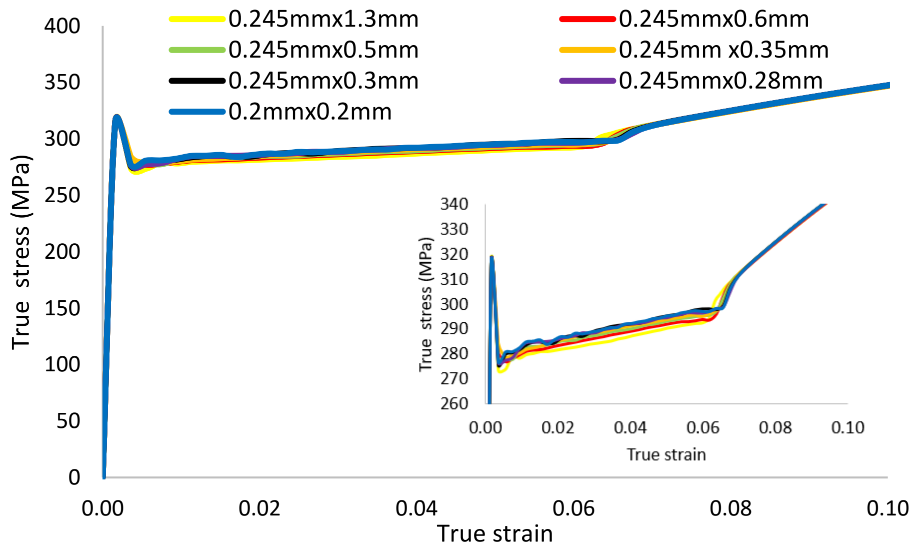

Figure 6-4: Mesh size sensitivity analysis for the mesh in the gauge length with the inset showing the flow stress in the elastic/plastic transition. The numbers shown in the legend refers the width and length of the gauge length mesh size.

From these results, it was found that the results did not change when the mesh in the gauge length was reduced to 0.245 mm (width) x 0.3 mm (length). In all cases, the mesh size in the thickness direction (z-direction) of the sample was left fixed as 0.5 mm. Choosing this mesh size resulted in the 10,896 elements in the model.

The effect of changing the displacement increment per step used for the calculations is shown in Figure 6.5. It was found that as the displacement per step decreased, the upper yield point increased until it saturated to a constant value at a displacement increment of 0.004 mm per step. Based on this, a step size of 0.004 mm/step was used for all simulations.

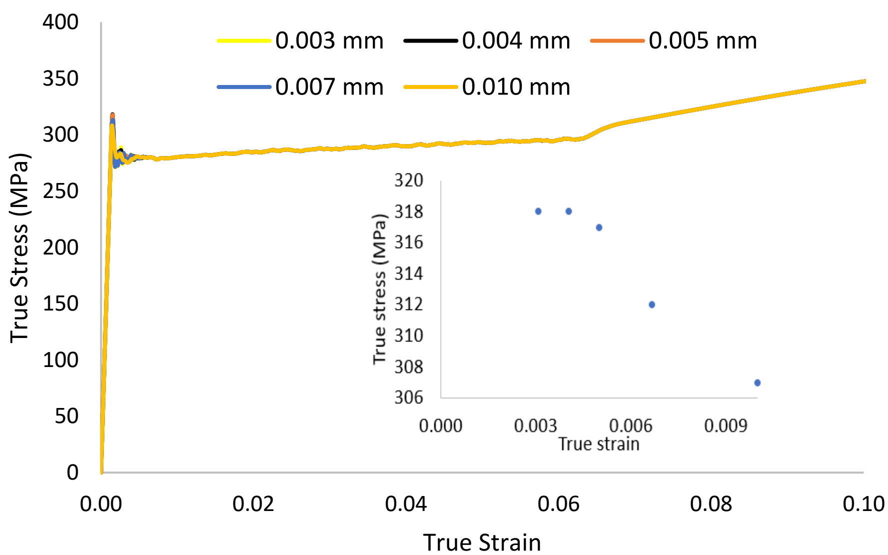

Figure 6-5: Displacement increment per step sensitivity analysis with ampliation of flow stress in the elastic/plastic transition.

6.5 Prediction of macroscopic mechanical behavior of the ULC steel

As shown in Figure 6.6 the FEM predictions and experimental results for the as-annealed material show very good agreement over the range of stresses and strains measured. The yield point elongation and upper yield stress from the FEM model are approximately 16% (0.012), and 2% (8 MPa) smaller than those measured in experiment. This is in the range of scatter seen experimentally in chapter 5.

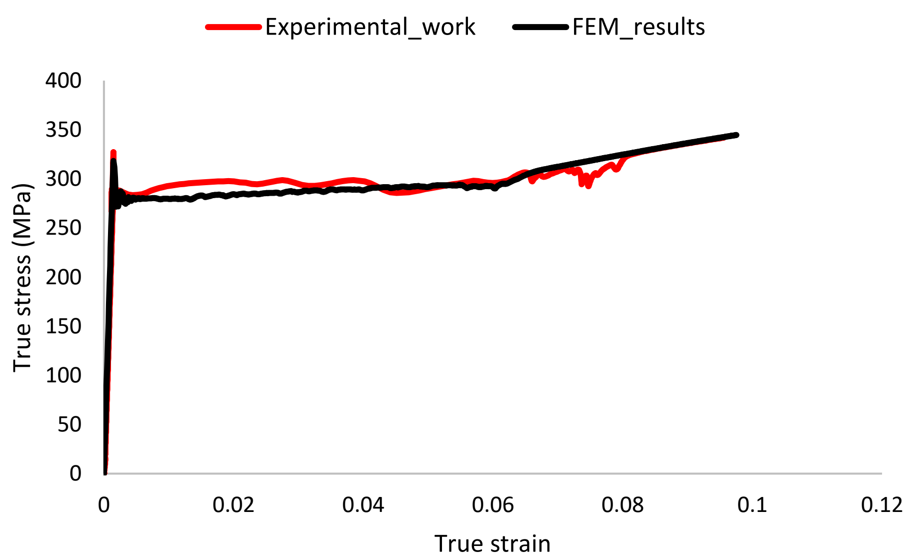

Figure 6-6: Comparison between the experimental tensile stress-strain curve and that predicted by the FEM model for samples in the as-annealed state.

It is not a surprise that the FEM predicted upper yield stress matches well the experimental work because σ_U was given as a material parameter. The prediction of σ_L and yield point elongation are, however, results of the constitutive law used within ABAQUS. The constitutive law, when combined with the FEM model, gives rise to strain localization at the sample's shoulders, causing Lüders band initiation and propagation. This will be discussed in more detail below.

The next step was to use the developed model to predict the mechanical behavior of ULC steels following strain aging where the direction of testing following aging was the same as that used in pre-deformation. In this case, the only additional information provided to the model was the time evolution of the upper yield strength (σ_U) developed in the model in Chapter 5 (equation 5.2). The resulting predicted behavior is compared to selected experimental data from samples aged different times and temperatures in Figure 6.7.

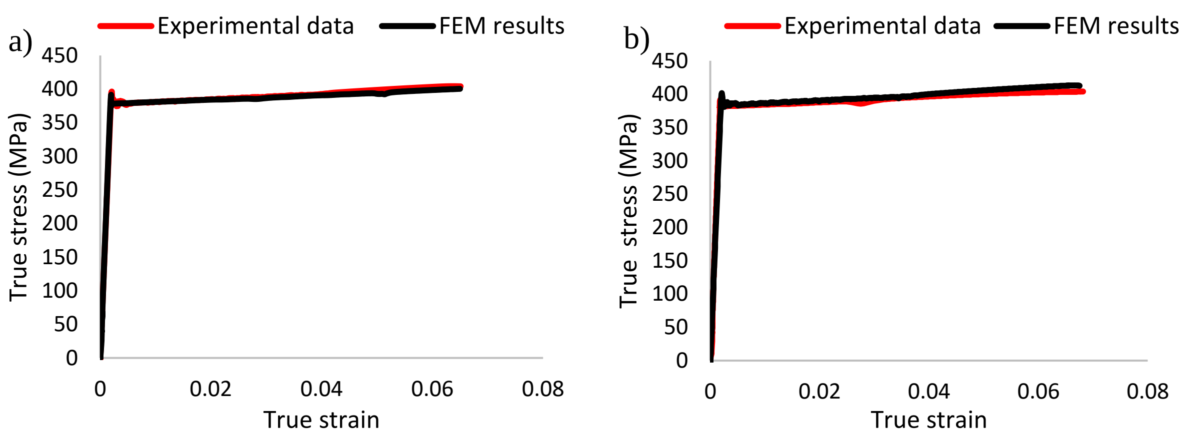

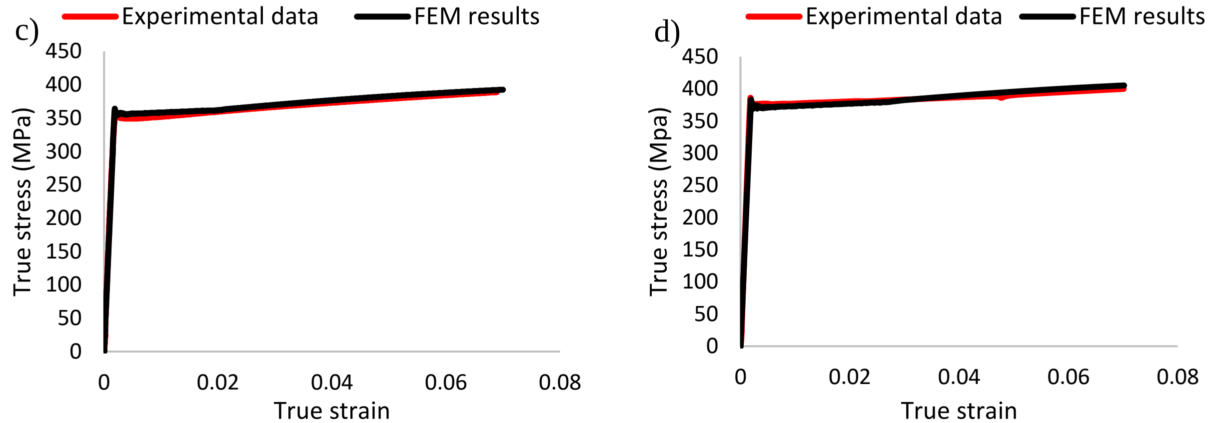

Figure 6-7: Comparing experimental tensile curves with FEM after strain aging for a) 120ºC during 10 min, b) 100ºC during 100 min, c) 70˚C for 10min and d) 70˚C for 30min.

Overall the FEM model is shown to do an excellent job of reproducing the stress-strain behavior as a function of the various pre-strain conditions considered when combined with the model for predicting the upper yield stress presented in Chapter 5. What is not clearly shown by the stress-strain curves is the fact that during testing the plastic deformation occurs non-uniformly over the gauge section of the sample during Lüders band propagation. In order to compare the Lüders band motion in experiments and simulations, full-field experimental measurements of the strains on the surface of the samples were made using digital image correlation. The results of this are described below.

6.6 Prediction of mesoscopic mechanical behavior of the ULC steel

As noted above, the FEM model should predict not only the stress-strain curve but also the non-uniform plastic deformation arising from Lüders band propagation. To evaluate this, digital image correlation (DIC) was used to experimentally measure the mesoscopic plastic strain distribution on the surface of tensile samples. The heterogeneous plastic deformation observed during Lüders band propagation was compared to FEM predictions for samples tested in the as annealed conditions and following strain aging.

6.6.1 DIC basics and sensitivity analysis

DIC has previously been successfully used to track the speed and pattern of Lüders band propagation during deformation of steels [83], [94], [95]. Here the LaVision DIC system (hardware and software) was used to capture and process data. A brief summary of how DIC works and the methodology implemented in this thesis will be presented first, before describing results and comparing with simulations.

The first task in DIC post-processing analysis (after the test is performed) is to select the desired area to be analyzed (mask setting). In this study, the gauge length of the samples was selected. Next, it is necessary to select a seeding point inside of the area of interest (masked area) to make an initial guess for DIC analysis [94], [96], [97]. It is important to notice that the selected seeding point needs to be in a place where speckles are easy to be identified [94], [97]. Next, a subset size and step size must be selected before data analysis. The subset size refers to the size of the sub-portion of the surface whose center is used to calculate the displacement from the reference image [98]. The step size is the selected distance between subset centers [99], [100]. A schematic illustrating these basic concepts is given in Figure 6.8:

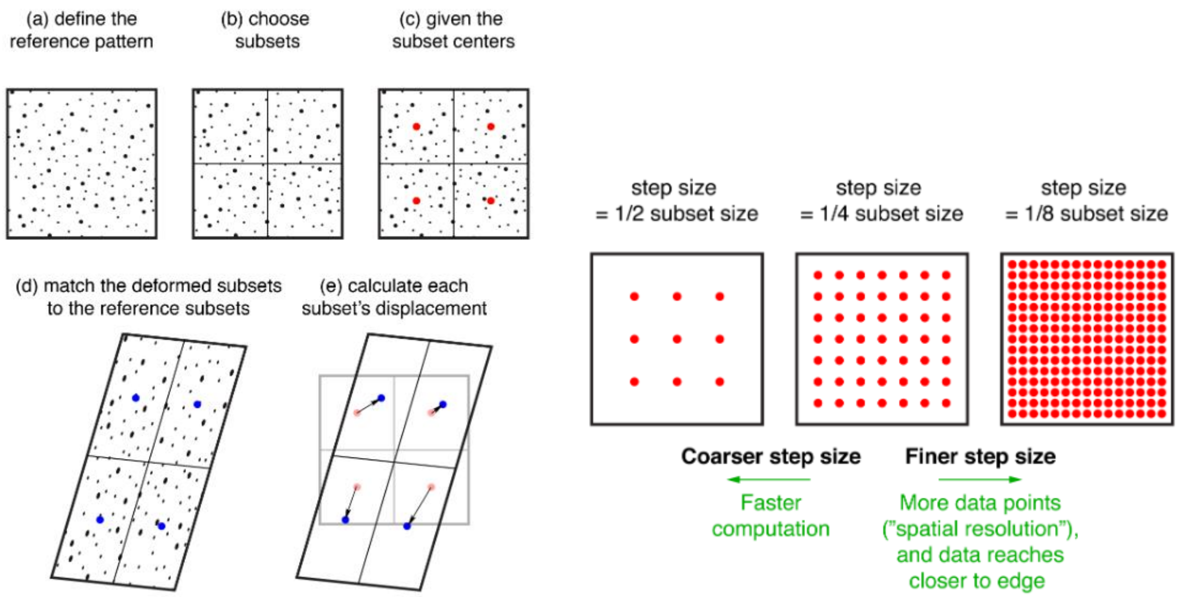

Figure 6-8: Illustration of how DIC analysis is performed. Here reference patterns, subset and subset centers are defined, and displacement is calculated by comparing the deformed subset to the reference subset. Step size and subset size play an important role into computational time and spatial resolution [86].

The subset size is limited by the fact that each subset must contain at least three speckles. A competition exists between using a larger subset size to allow for better pattern matching versus a smaller subset size giving better spatial resolution but with more error in pattern matching [101]. Spatial resolution is, however, more influenced by the step size used in measurements [100]. Normally, the step size is set to be between one-third to one-half of the subset size [99]–[101]. In order to choose the subset size and step size, a sensitivity analysis was performed, where step size was fixed, and subset size was changed so that the ratio between subset size and step size varied between one-fifth to one-half. The results from measurements made on a sample during elastic loading were then used to estimate the young's modulus (E) based on the recorded load and average gauge length strain measured in DIC as a function of

DIC parameters (Table 6.2). In this case, E was shown to only change slightly as the ratio of subset to step size was increased, especially when subset size reached 21 pixels. Therefore, for further studies a subset size of 21pixels and step size of 8 pixels were selected for use in all the DIC experimental analysis performed in this work.

Table 6-1: Change in the young’s modulus estimated by DIC arising from changing the ratio subset and step size.

Subset size (pixel)	Step size (pixel)	Young`s Modulus (GPa)
11	8	206
21	8	204
25	8	204
31	8	204

6.6.2 Investigation of Lüders band formation

Digital image correlation was used to study Lüders band nucleation and propagation during tensile testing of the as-annealed and strain aged samples described above. The point of nucleation of Lüders bands was not possible to clearly identify due to the limited image acquisition frequency used here (9Hz). In the literature it has been argued that Lüders band nucleation occurs before the attainment of the upper yield stress, this occurring by a process called “pre-yield micro-strain” [83], [102], [103]. Others have attributed nucleation to the upper yield stress [45], [104], [105]. In this work, the DIC results were only able to detect clear evidence of a Lüders band (localized strain within the gauge section) at stresses close to the lower yield stress when the Lüders band had covered the entire width of the sample [103]. As noted above this is likely a consequence of the limited acquisition rate of the system used and the limited spatial resolution induced by the camera [94]. To visualize the Lüders bands in these experiments, maps of the strain parallel to the tensile axis are plotted along with the tensile strain on a line running along the length of the gauge section in the center of the sample.

For both as-annealed and strain aged samples, Lüders bands were observed to propagate from the shoulders of the samples[38], [103]. This was expected due to the stress concentration at fillets. Lüders bands were observed to propagate from both the upper and lower shoulders of the samples, with some cases exhibiting two bands. The occurrence of the second band in some cases may be due to the delayed yielding of some grains within the band front [106]. Despite the number of bands, in both cases, the Lüders band(s) travel through the entire gauge length before the material returns to homogeneous deformation. Figure 6.9 and 6.10 illustrate the behavior of Lüders bands as they propagate through the gauge length at different levels of tensile deformation for an as-annealed sample and a strain aged sample. This confirms the heterogenous macroscopic behavior associated with the yield point elongations discussed earlier in this chapter.

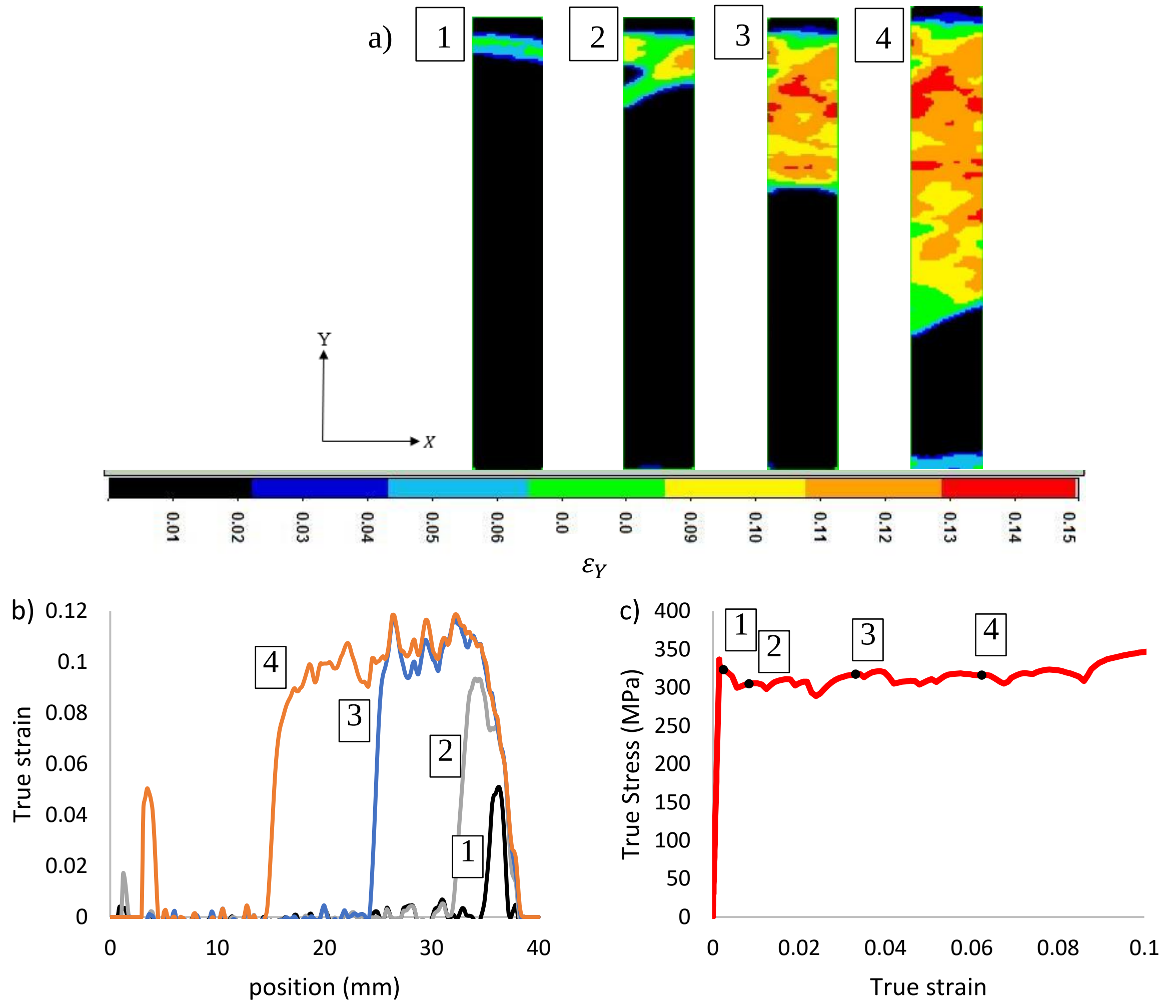

Figure 6-9: Lüders band propagation during 10% pre-deformation. a) Strain parallel to tensile axis (ε_Y) at four levels of tensile deformation b) From the data in (a) one-dimensional plots of ε_Y have been made with the position running along the center of the gauge length of the sample. The numbers in (a) and (b) correspond to the positions on the macroscopic tensile curve shown in (c).

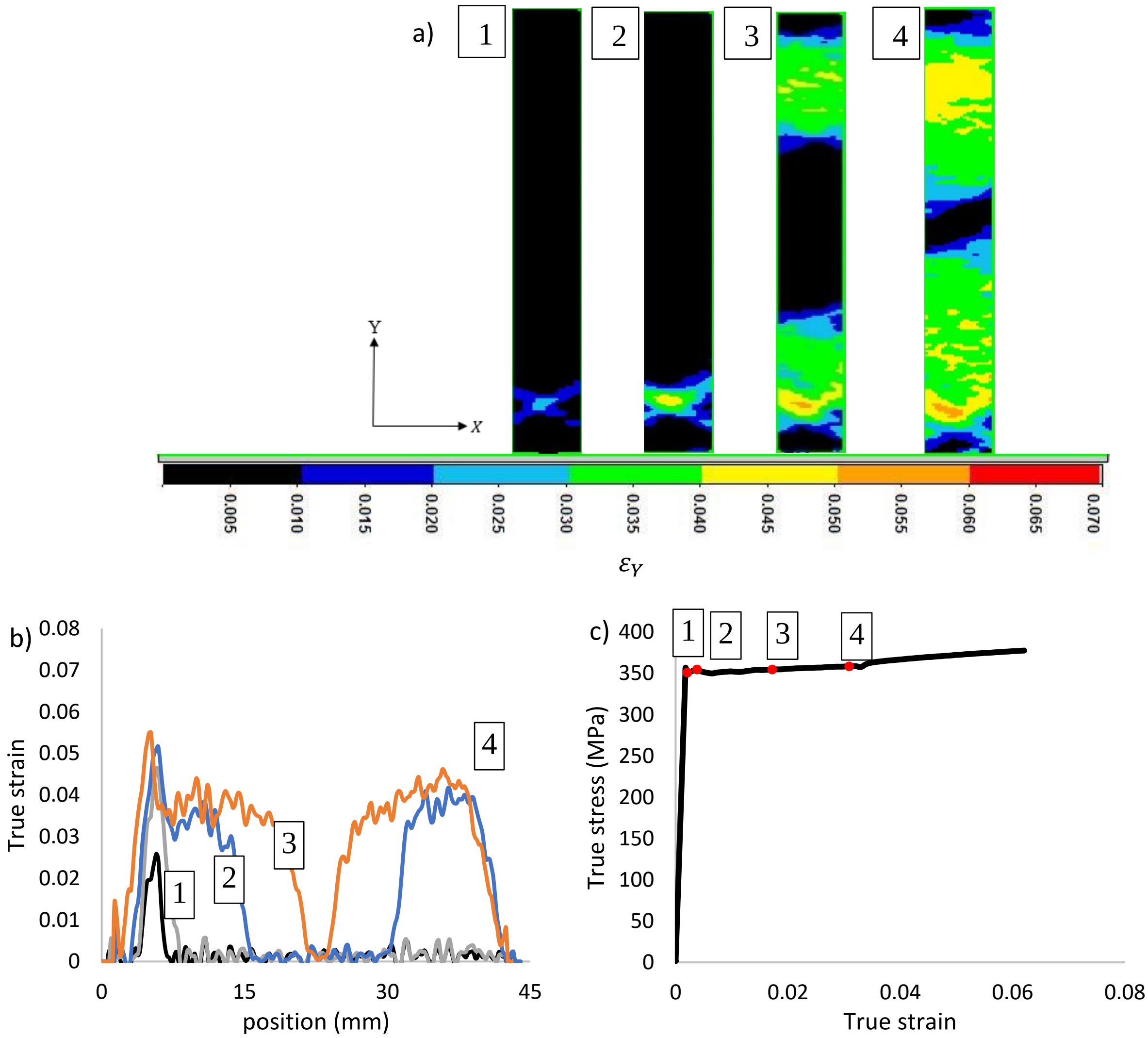

Figure 6-10: Lüders band propagation during reloading after aging for 10 min at 150ºC. a) Strain parallel to tensile axis (ε_Y) at four levels of tensile deformation b) From the data in (a) one-dimensional plots of ε_Y have been made with the position running along the center of the gauge length of the sample. The numbers in (a) and (b) correspond to the positions on the macroscopic tensile curve shown in (c).

The above results from the DIC measurements show several important features, particularly the magnitude of strain accompanying Lüders band, yield point elongation and Lüders band angle and velocity.

At the onset of Lüdering, the magnitude of Lüders strain is in the order of 10^{-2} for both tested conditions. This is one order of magnitude greater than the applied strain. The difference between Lüders band strain and applied strain decreases as the Lüders band propagates and when it has traveled the entire gauge length, the material starts deforming homogenously again. The strain induced by the Lüders band was calculated by averaging the largest 50% of values in the region where the Lüders band has passed. Finally, apart from the very beginning of Lüders band propagation (Figure 6.9 and Figure 6.10- label 1), the strain-induced at the Lüders band front approximates to the yield point elongation.

The as-annealed sample had a yield point elongation of 0.09 (Figure 6.9) whereas the yield point elongation was 0.04 for a sample pre-strained 10% then aged (Figure 6.10). These values are compatible to the tensile test results presented on chapter 5. As seen on chapter 5, despite what has been reported in the literature [92], [107], no clear relationship between the increase in yield point elongation and the drop in yield stress was found. However, a second factor, the work hardening rate, also contributes to the change in yield point elongation seen here. In fact, an increase in yield point elongation with decrease in work hardening rate has been reported in the literature [91].

The angle of the Lüders band as observed by DIC observation was shown to be very similar to what is found in the literature [82], [83]. As expected, the Lüders band deforms while respecting plane strain in the x-direction ($\varepsilon_x = 0$) by being oriented at close to 55º to the tensile direction [46].

The Lüders' band velocity (v) is strongly dependent on the applied stress [107]–[109], and a change in stresses can cause the Lüders band velocity to vary during the tensile test. The velocity was found to change between 3mm/s to 5mm/s for the test shown in Figure 6.9, and between 10mm/s to 20mm/s for the test shown in Figure 6.10. Using $\dot{\varepsilon} = \varepsilon_L \frac{v}{l_o}$ [36], where l_o is 40 mm, the strain rate of samples loaded after annealing and reloaded after aging treatment can be calculated. For the case of the sample loaded after annealing, where $\varepsilon_L\ is$ 0.09 , the strain rate was found to be between $3x10^{-3}\ s^{-1}$ and $1x10^{-2}\ s^{-1}$. While the sample reloaded after aging ($\varepsilon_L = 0.04$), the strain rate was calculated to be between $2x10^{-2}\ s^{-1}$ and $5x10^{-2}\ s^{-1}$. In both cases the calculated strain rate is close to the applied strain rate $6x10^{-2}\ s^{-1}$.

These features observed experimentally can be compared directly with the predictions of the FEM simulations. Because a defect was used in the FEM simulations to induce a single Lüders band to propagate from the same location each time, one cannot directly simulate the statistical aspects of Lüders band formation (e.g. location, one or two bands). The amount of strain induced by the Lüders band, the length of the band front and the shape of the band front can all be compared, however. These were not considered in the initial fitting of the constitutive law used here. Figure 6.11 and 6.12 illustrate Lüders band propagation during loading after annealing and reloading after aging for 10 min at 150ºC.

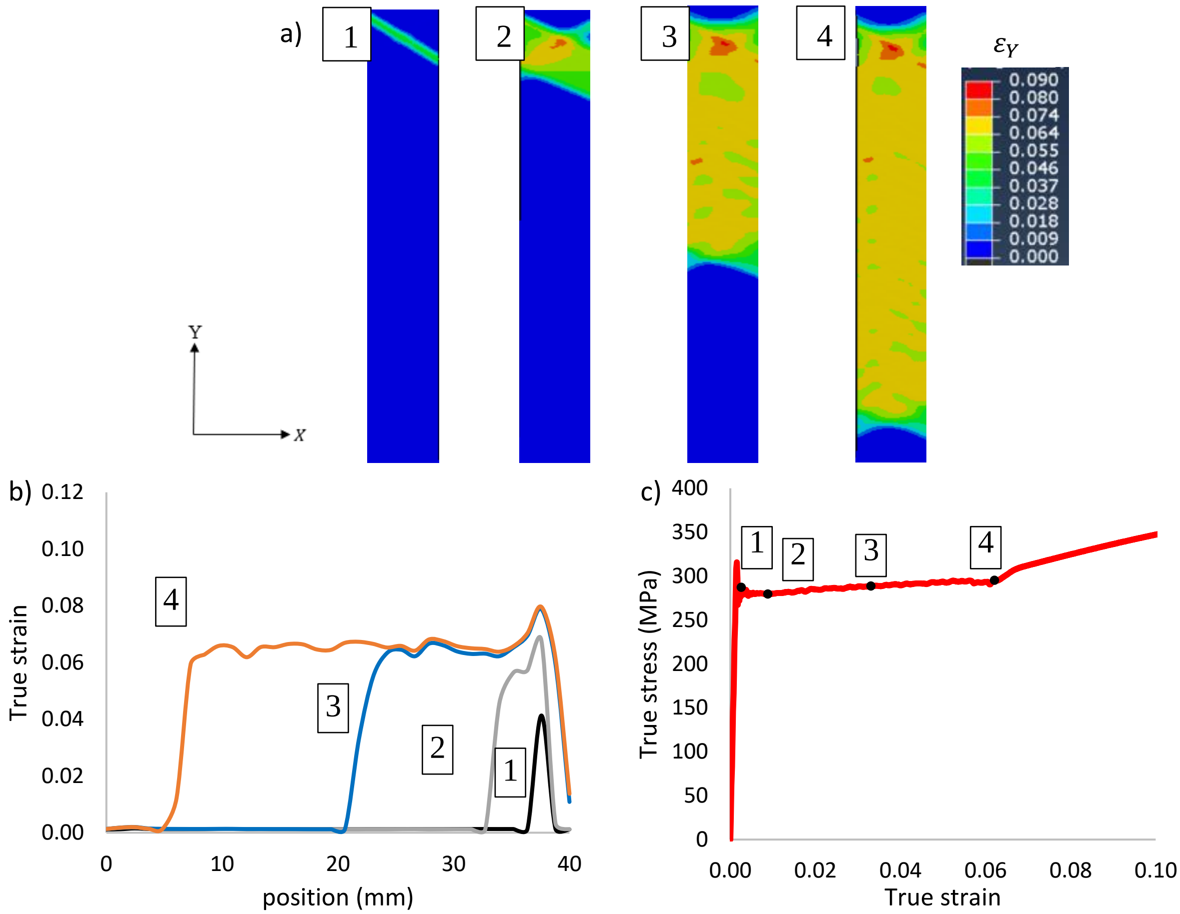

Figure 6-11: Lüders band propagation during 10% pre-deformation using FEM. a) Strain parallel to tensile axis (ε_Y) at four levels of tensile deformation b) From the data in (a) one-dimensional plots of ε_Y have been made with the position running along the center of the gauge length of the sample. The numbers in (a) and (b) correspond to the positions on the macroscopic tensile curve shown in (c).

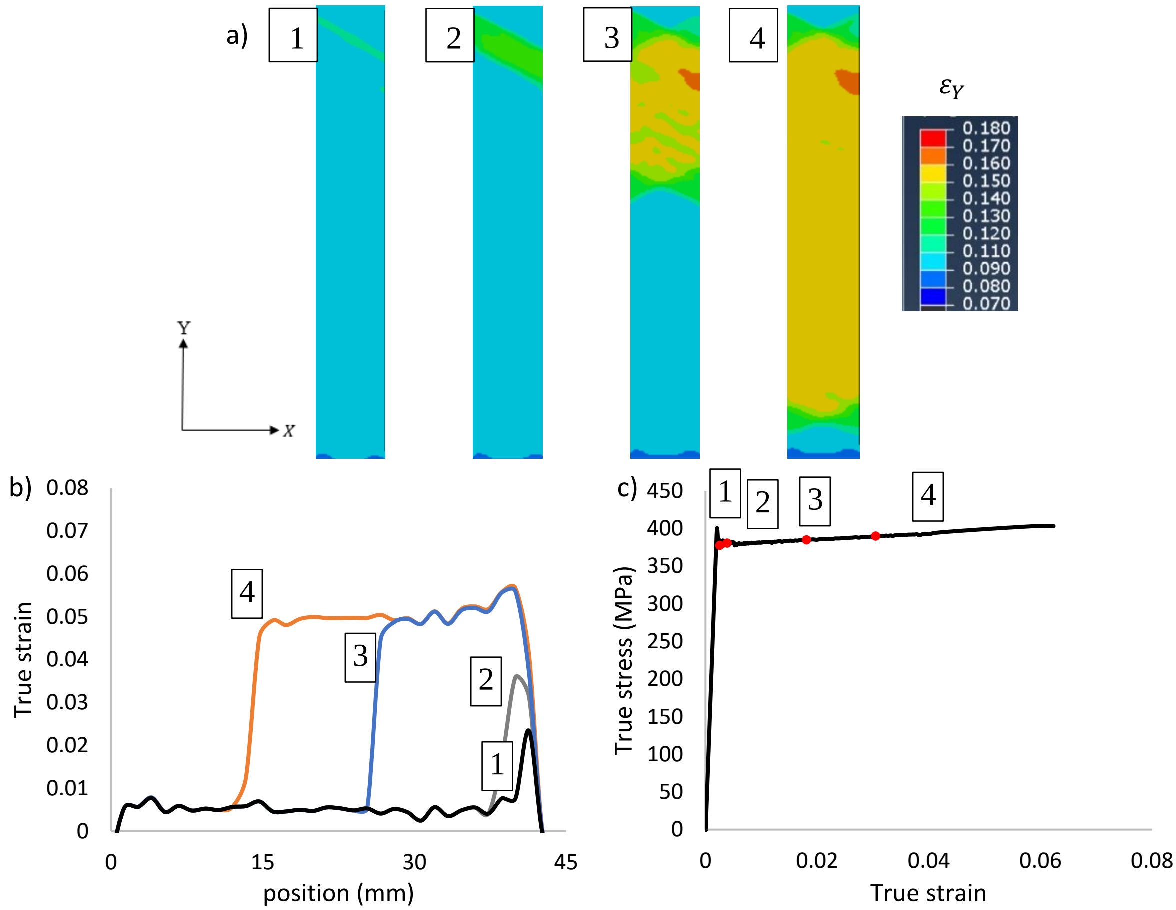

Figure 6-12: Lüders band propagation during reloading after aging for 10 min at 150ºC using FEM. a) Strain parallel to tensile axis (ε_Y) at four levels of tensile deformation b) From the data in (a) one-dimensional plots of ε_Y have been made with the position running along the center of the gauge length of the sample. The numbers in (a) and (b) correspond to the positions on the macroscopic tensile curve shown in (c).

The shape of the bands seen in the FEM model is very similar to those observed experimentally by DIC. Figures 6.13 and 6.14 show the strain profile along the center of samples with Lüders bands obtained from experiments (DIC) and model (FEM) for different levels of macroscopic strain side by side. The strain profile was taken from the same positions shown in Figures 6.9 and 6.11 (during pre-strain test after annealing), and Figure 6.10 and 6.12 (during reloading after aging at 150ºC for 10 minutes).

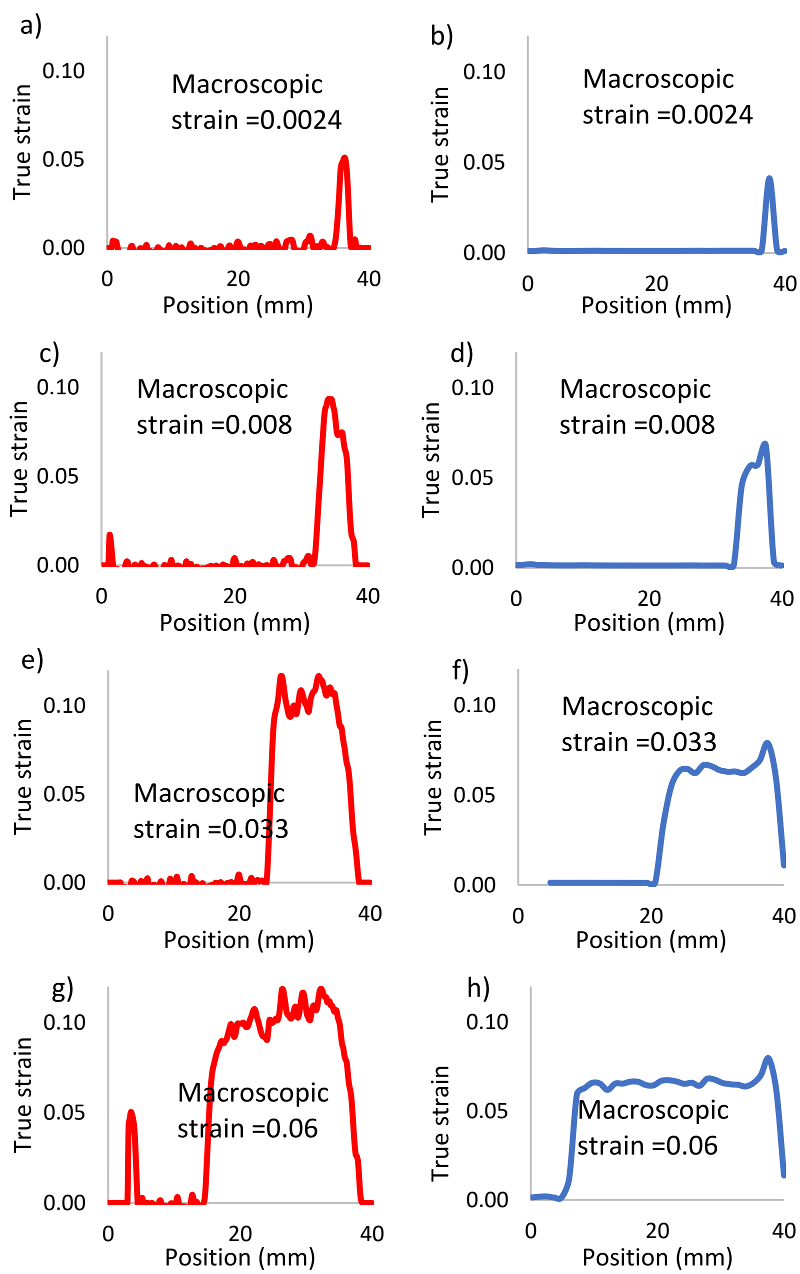

Figure 6-13: Lüders band shape during its propagation through the gauge length using DIC (a, c, e, and g) and FEM modelling (b, d, f, and h) during pre-straining test after annealing.

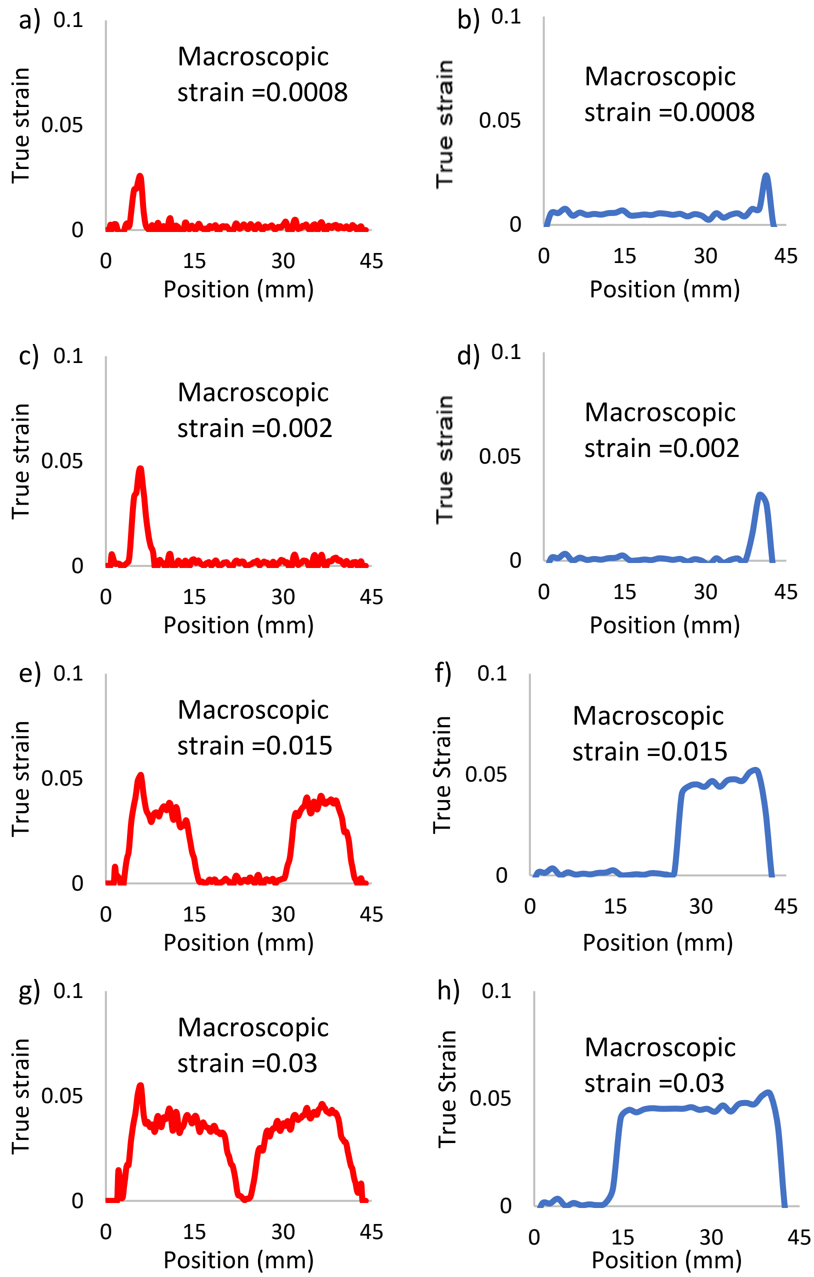

Figure 6-14: Lüders band propagation through the gauge length using DIC (a, c, e and g) and ABAQUS (b, d, f and h) during reloading after aging test at 150ºC for 10min.

Qualitatively the results obtained by FEM and DIC are very similar. Now, a more quantitative comparison is performed by comparing the experimental and modeling results in terms of the magnitude of strain-induced by the Lüders band and the Lüders band length (L_{band}). The magnitude of strain induced by the Lüders band was calculated by averaging the greatest 50% strain points above 0.008 strain (this being just higher than the background 'noise' in the strain measurements) along the centerline of the specimen gauge length. Here, ε_{max} is maximum strain induced by Lüders band. For instance, Figure 6.15 presents 12 strain measurements above 0.008, and the greatest 50% values (6 values) were averaged. Lüders band length was calculated by looking at the difference in the position (x-axis) where the band starts and finishes at a fixed strain (y-axis), defined here to be 0.008 (Figure 6.15).

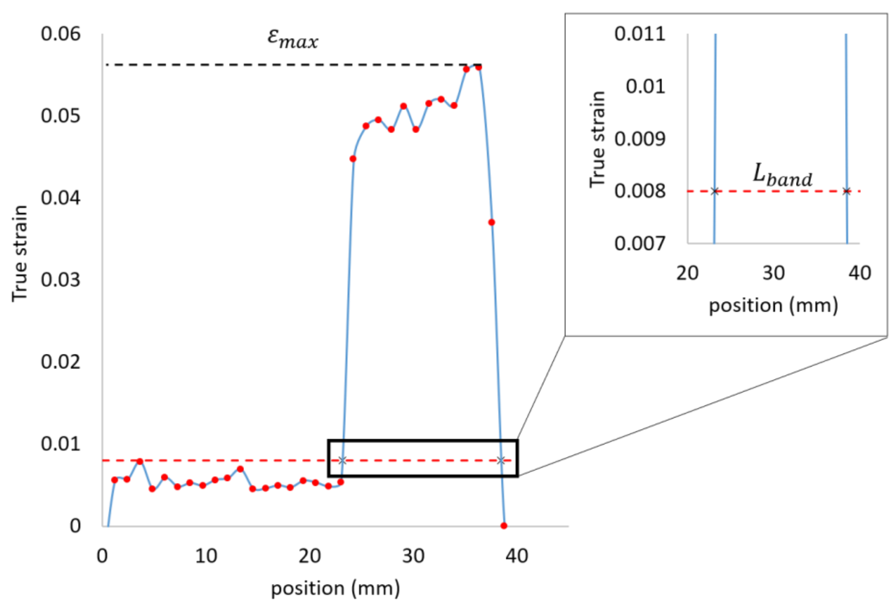

Figure 6-15: Illustrates the procedure used to calculate the magnitude of strain induced by Lüders band and Lüders band length (L_{band}).

Figure 6.16 and 6.17 compare the strain induced by the Lüders band and the Lüders band length measured from FEM and DIC tests. The uncertainty bars in Figure 6.18 were calculated from the difference between the average of the greatest 50% strain points, and maximum and minimum strain values within the greatest 50% strain points. These data points were calculated using the same level of macroscopic strain shown in Figures 6.16 and 6.17. One can see that the FEM model does a good job of predicting both the geometry and strain levels associated with the Lüders bands for both the pre-deformed and aged materials. The fact that the strain induced by the Lüders band measured experimentally is higher than that predicted in Figure 6.16 is a consequence of the fact that the model underestimates the length of the yield point elongation (Figure 6.6).

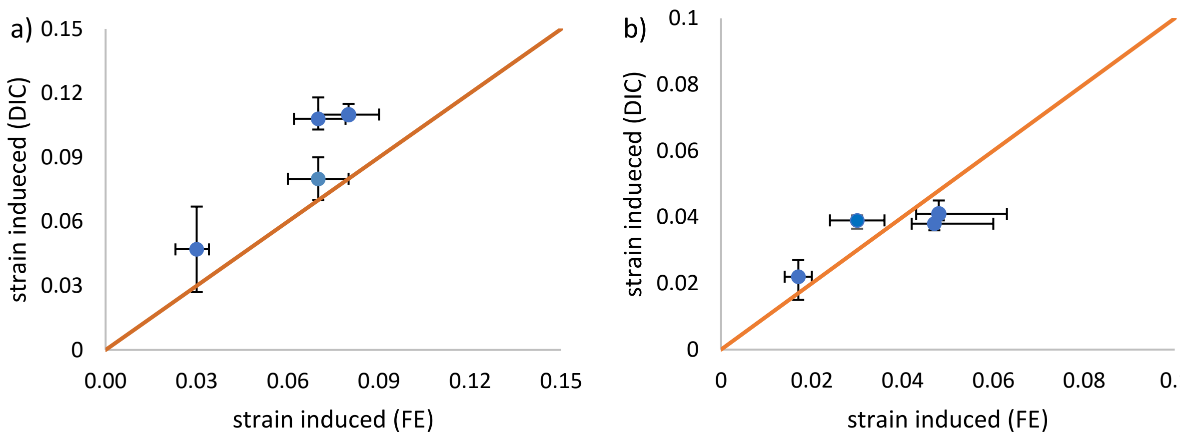

Figure 6-16: Comparison of strain induced by Lüders band between the FE model and DIC during a) 10%pre-deformation after annealing and b) reloading after aging at 150ºC for 10min. The uncertainty bars are displayed in both Figures.

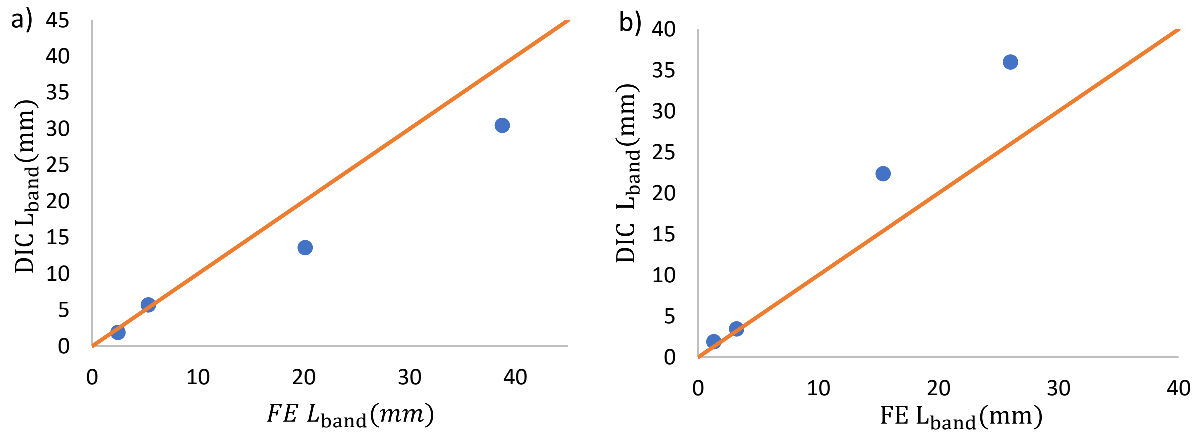

Figure 6-17: Comparison of the Lüders band length between the FE model and DIC during a) 10% pre-deformation after annealing and b) reloading after aging at 150ºC for 10min.

One of the questions that arose in fitting the experimental stress-strain response to the measured stress-strain curve is whether a relationship could be found between the yield point elongation (found experimentally or predicted by FEM simulation) and the value of the parameter $\Delta\varepsilon$ shown in Figure 6.18. The parameter $\Delta\varepsilon$ in the constitutive model is defined as the magnitude of strain that one has to impose before the flow stress rises back to the value it had at the upper yield point. If one could find such a relationship it would make fitting the stress-strain response significantly easier.

Unfortunately, upon the comparison of FEM predicted yield point elongations and the corresponding values of $\Delta\varepsilon$ from the input constituent law, it was found that the yield point elongation is not equal to $\Delta\varepsilon$ (orange line). In this case, the value of $\Delta\varepsilon$ was changed by changing only the value of the upper yield strength in the case of simulated strain aged samples. The conditions chosen here correspond to fits to experimental stress-strain conditions.

In the case of the conditions fit to aged samples at 70°C one sees that a linear relationship does seem to exist but with the $\Delta\varepsilon$ needing being twice the value of the yield point elongation. One factor that might influence this is the fact that at the Lüders band front the stress-state is not simply uniaxial. This may cause a change in local yield/flow stress, affecting the prediction of yield point elongation. Interestingly one sees that for the as-annealed sample, the value of $\Delta\varepsilon$ is nearly the same as the yield point elongation. The important difference between this condition and that of the aged samples is the magnitude of the work hardening after $\Delta\varepsilon$. The aged materials have a much lower work hardening rate meaning that a small error in the predicted flow stress can lead to a large effect on the predicted strain. This suggests that using a relationship between $\Delta\varepsilon$ and the yield point elongation is unlikely to help in fitting the constitutive model given the sensitivity of $\Delta\varepsilon$ to the work hardening rate in the case of the aged materials. At best, this could be used to indicate trends in behaviour.

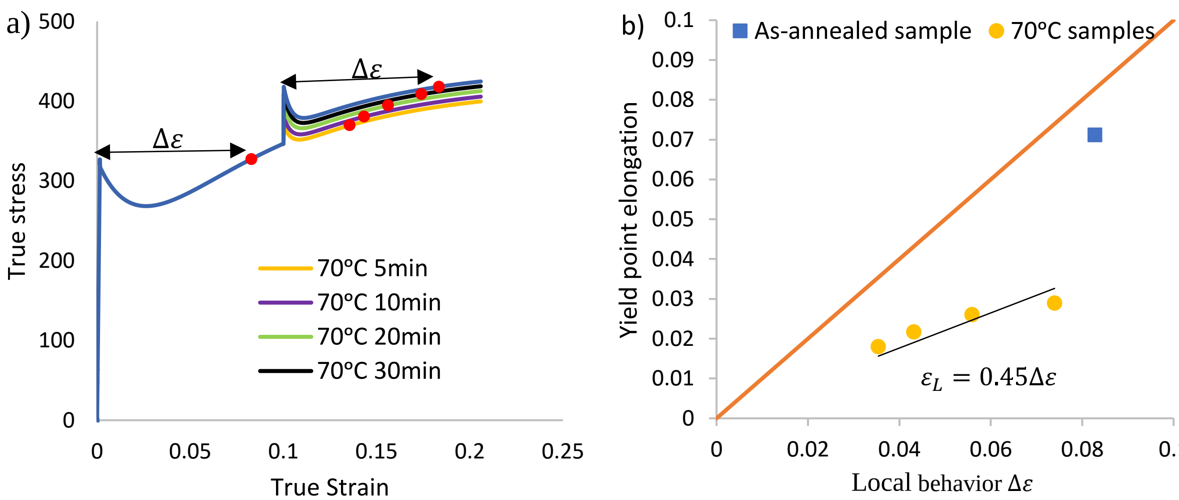

Figure 6-18: Represents a) the local behavior $\Delta\varepsilon$ taken from fits to experimental stress-strain curves and b) the prediction of yield point elongation of samples (as-annealed and aged at 70ºC for different times) using $\Delta\varepsilon$.

6.7 Summary

In this chapter, a finite element model was created in ABAQUS, and combined with the analytical model (chapter 5) and a constitutive law to predict the macroscopic and mesoscopic mechanical behavior of ULC steel during uniaxial tensile tests. In terms of macroscopic behavior, strain aging and mechanical behavior of the ULC steel can be predicted for different aging conditions. Furthermore, this model proved to predict the mesoscopic behavior of ULC carbon steels, especially the strain induced by Lüders band motion and geometry of the Lüders bands. Therefore, this model allows one to predicted and understand the mechanical behavior of aged ULC steels at different scales (macro and mesoscale) during monotonic tensile testing.

Chapter 7: Directionality of the strain aging effect

7.1 Introduction

This chapter aims to investigate the directionality of strain aging of ULC steels. To evaluate this, samples were annealed, cold-rolled to ~10% reduction, aged and then re-loaded in tension. The tensile tests were performed at 0˚, 45˚ and 90˚ to the sheet's rolling direction. As described in Chapter 3, one aging condition is considered (150˚C, 10 minutes), this corresponding to the maximum in strain aging response (Chapter 5, Figure 5.14). The choice of only one aging time/temperature was a result of the delay between rolling and having the sample machined. To avoid complications resulting from small amounts of aging occurring at room temperature during this wait, only this highly aged condition was considered. The mechanical behavior after aging is compared here to the mechanical response of samples presented in Chapters 5 and 6. Also, DIC observations have been made to examine Lüders band formation and propagation in these cold-rolled, aged and tensile tested samples. Finally, a revised constitutive model is presented to help in explaining the observed behavior on strain path change.

7.2 Starting plastic anisotropy

To understand the anisotropy of strain aging, it is necessary to first know the plastic anisotropy of the annealed material prior to cold rolling. Tensile samples were cut from the as-received sheet at 0˚, 45˚ and 90˚ to the rolling direction. These were then annealed to fully recrystallize them (800˚C for 7 min, the same annealing conditions used for the materials described in

Chapters 5 and 6) and then they were tested in tension. Figure 7.1 illustrates the mechanical behavior of ULC steels at different tested directions using the engineering stress-strain diagram.

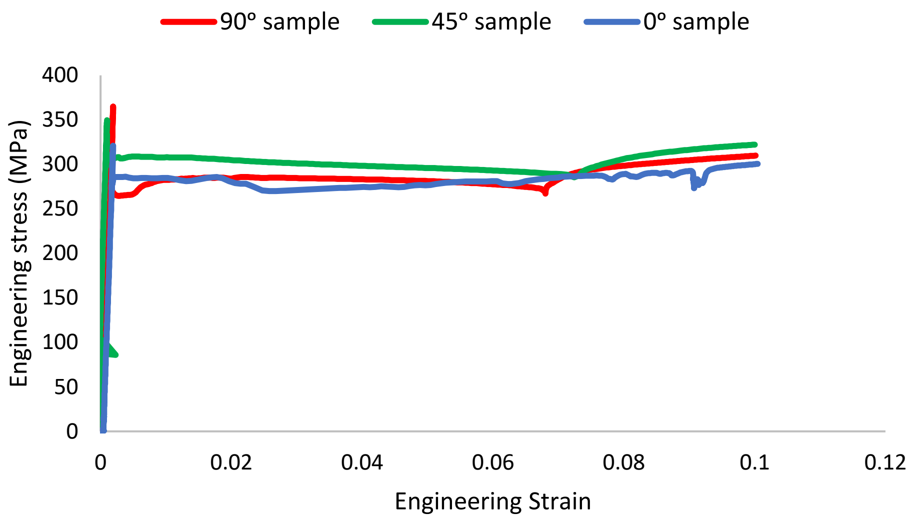

Figure 7-1: Mechanical behavior of ULC steels at different directions to RD.

When compared after 10% tensile deformation, the level of pre-deformation used here, the flow stress of the sample cut at 45˚ to RD showed the highest flow stress (320 MPa). This is compared to flow stresses of 310 MPa for the sample cut at 90˚ to RD and 300 MPa for the sample cut parallel to RD. This difference in flow stress is relatively small as can be seen if these values are compared to the values shown in Figure 5.5 where multiple samples prepared from the same direction in the sheet (parallel to RD) showed a variation of $\pm 6MPa$. This indicates that while the starting material has some plastic anisotropy (due to crystallographic texture) the effect is not very large.

7.3 Tensile behavior of rolled, aged and tensile tested samples

Cold rolling was designed as the pre-deformation path for this study with the aim of achieving the same flow stress following rolling as was obtained after 10% tensile strain in tension [110]. However, controlling the level of strain introduced during cold rolling is difficult. The inability to achieve the desired level of strain will affect the mechanical behavior of the tested materials, making it difficult to compare different samples. With this in mind, special precautions were made to minimize the sample-to-sample variations of strain imposed during rolling. First, for each set of samples studied, the rectangular sheets were rolled in a single pass. This was performed without changing the position of the rolls. Once all samples had been rolled, the roll gap was reduced and the next pass was performed, this process being repeated up to the final desired thickness. The thickness of the samples was measured in 10 different positions before rolling and after each rolling pass. The thickness measurement was performed by using a digital micrometer. From these measurements the average true strain was calculated using the average measured thicknesses. The target was to cold roll to the same equivalent plastic strain, $\varepsilon_{eq} = 0.1$ using $\varepsilon_{eq} = \frac{2}{\sqrt{3}}\varepsilon_z$ for each sample. This required a true thickness strain of $\varepsilon_z = \ln\left(\frac{t_f}{t_o}\right) = -0.09$, where t_f is the sheet thickness after rolling and t_o is the sheet thickness before rolling.

A total of 8 rectangular samples were subjected to cold rolling. The dimensions of these samples were constrained by the size of the roll gap of the rolling mill and the size of the annealing furnace. Out of these rolled sheets tensile samples were cut. For the case of tensile samples cut at 0˚ and 90˚ to RD, a total of 3 samples could be cut from one rolled sheet. For the case of the tensile samples cut at 45˚ to RD only one tensile sample could be produced per rolled sheet (Figure 4.3).

In total 4 tensile samples were produced for each test direction. Two samples were tested in the as rolled (no aging treatment) state while the other 2 were aged before testing. As mentioned above, for the 0˚ and 90˚ conditions, three samples could be cut from one rolled sheet. Two of these samples were aged while the third sample was tested in the as-rolled condition. The fourth sample was then taken from a second rolled sheet and tested in the as-rolled condition. For the case of samples tested at 45˚ to RD each sample was taken from a separate rolled sheet.

Table 7.1 gives a detailed description of each of the samples prepared. The rolled sheets are labeled A-H. The tensile samples taken from each sheet, and their condition (aged, not aged) are indicated. The uncertainty in the strain was computed using $\Delta\varepsilon = \frac{1}{t_f}\,\Delta t_f + \frac{1}{t_o}\,\Delta t_o$, where t_o is the average initial thickness, t_f is average final thickness, and Δt_f, Δt_0 are the standard errors of the mean values of t_f and t_o[111], [112]. Table 7.2 displays the calculated uncertainties for all samples subjected to cold rolling.

Table 7-1: The nomenclature used for the rolled sheets (A-H) and information of the subsequent tensile samples taken from them.

A	B	C	D	E	F	G	H
0˚	0˚	90˚	90˚	45˚	45˚	45˚	45˚
Aged	Not aged	Aged	Not Aged	Aged	Aged	Not aged	Not aged
Aged	---------	Aged	---------	---------	---------	---------	---------
Not aged	---------	Not aged	---------	---------	---------	---------	---------

Table 7-2: The average initial thickness (t_0) and average final thickness (t_f) in millimeters, the estimated uncertainty in the strain, and strain ε_z.

	A	B	C	D	E	F	G	H
average t_f	0.921	0.922	0.920	0.924	0.914	0.919	0.921	0.921
average t_0	1.006	1.003	1.006	1.012	1.003	1.004	1.007	1.01
ε_z	-0.088	-0.084	-0.089	-0.090	-0.092	-0.088	-0.089	-0.092
Uncertainty in strain	0.0020	0.0001	0.0015	0.0004	0.0001	0.0026	0.0007	0.0001

It is important to note that tensile samples tested in the as-rolled (not aged) condition were taken from different rolled sheets, while samples tested at 0˚ and 90˚ after aging were produced from same rolled sheet (table 7.1). It is expected that is harder to have the same level of strain for the unaged samples compared to aged samples.

Figure 7.2 shows the true stress-strain curves obtained from each of the samples in Table 7.1. In each case the curves are plotted only up to uniform elongation as determined from the Considére criterion. It can be seen that the tensile samples taken from sheets C, D, G and H and tested in the as-rolled condition start to neck almost immediately upon reloading in tension. Samples tested at 45˚ and 90˚ to RD presented higher yield stress than samples tested parallel to RD, even though the 0˚ to RD samples displayed higher pre-strain levels than 45˚ and 90˚ directions. More specifically, the 45˚ and 90˚ directions registered yield stresses of 379 and 376 MPa, while the yield stress measured at 0˚ to RD was 360 MPa. Similar differences due to testing direction following rolling have been reported in the literature [5].

After aging, the mechanical behavior of all tested samples was similar, with the samples tested at 45˚ and 90˚ increasing their uniform elongation. Even samples tested at 45˚ to RD, which had a different pre-strain level (Figure 7.2-b), showed very similar results.

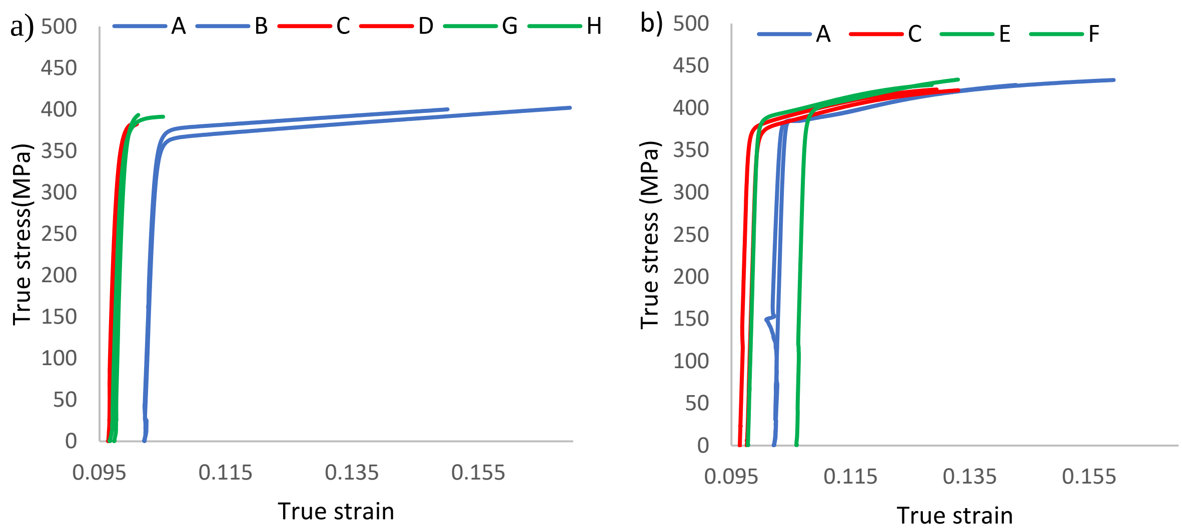

Figure 7-2: Displays the flow stress of tensile samples tested in different directions to RD for a) unaged and b) aged conditions. The labels A, B, C, D, E, F, G, H correspond to the samples listed in Tables 7.1 and 7.2.

The above results suggest that the yield stress of the sample tested at 0˚ to RD would match well the flow stress of an annealed sample tested in uniaxial tension to the same equivalent strain (tensile strain of 0.1). However, as shown in Figure 7.3, this was found not to be true. The higher observed yield and flow stress (~30 MPa) after rolling might be a consequence of either the change in deformation path or underestimation of pre-deformation during cold rolling. A change in strain path can lead to changes in the yield strength [4], [5], [8]. While the underestimation of pre-deformation during cold rolling can be a consequence of extra 'redundant' deformation induced by friction between the rolls and the workpiece [113]. It was assumed here that the rolling induced ideal plane strain deformation, which must be considered to give a lower bound estimate to the true level of plastic work done to the sample.

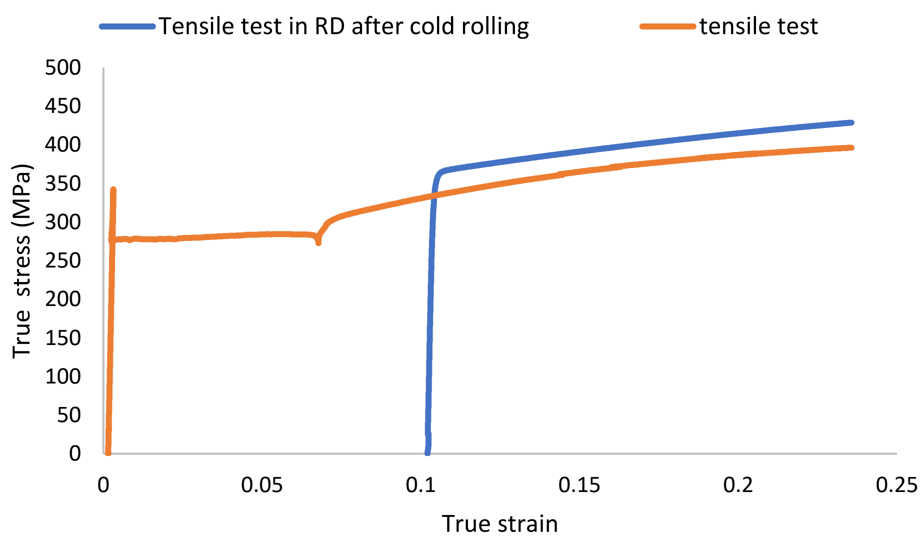

Figure 7-3: Comparison between two tensile samples. The first is an as-annealed sample tested with no pre-deformation (orange curve). The second (blue) is a sample rolled to an equivalent strain of 0.1, estimated from assumed plane strain deformation and the reduction in thickness, then tensile tested parallel to the rolling direction.

Fortunately, the work hardening rate can be used to help analyze the results as an additional consideration. A benefit of this approach is that, unlike strain, the stress and work hardening rate are not path dependent, when one assumes that they depend only on the dislocation density. In this way, the mechanical behavior of the as-rolled and re-tested in tension samples can be fairly compared with the annealed and tested in tension sample (Figure 7.4). The work hardening rate ($\frac{\partial\sigma}{\partial\varepsilon}$) was estimated by $\frac{\Delta\bar{\sigma}}{\Delta\bar{\varepsilon}}$ where $\Delta\bar{\sigma}$ and $\Delta\bar{\varepsilon}$ are averaged from 4 stress and 4 strain points, respectively. It can be seen that the working hardening rate of samples tested at 0˚ to RD match well that of the annealed sample before necking. However, tests at 45˚ and 90˚ to RD seem to start neck just after the onset of plastic deformation. Here both the conditions for the onset of diffuse necking $\frac{\partial\sigma}{\partial\varepsilon} = \sigma$ [114], and localized necking, $\frac{\partial\sigma}{\partial\varepsilon} = \frac{\sigma}{2}$ [115], [116], for sheet samples loaded in tension are shown.

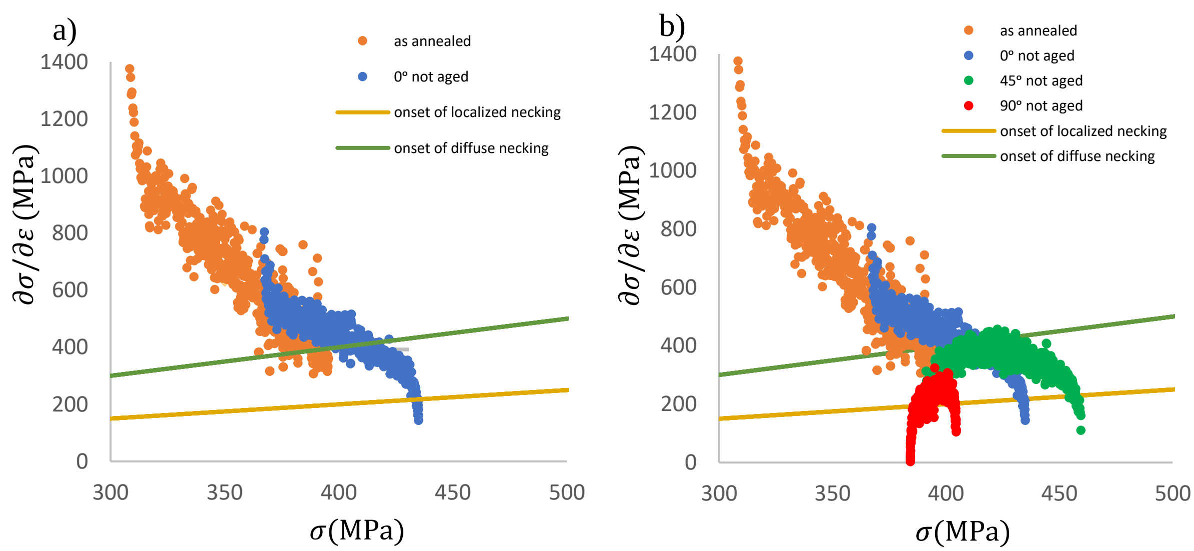

Figure 7-4: Work hardening rate comparison between a) as annealed (pre-deformed in tension) and as-rolled (0˚ to RD) samples and b) as-annealed (pre-deformed in tension) and as-rolled samples (0˚, 45˚ and 90˚ to RD) samples.

The similarity between the work hardening rate of the as-annealed and the as-rolled samples indicates that the pre-deformation developed during cold rolling was underestimated and needs to be readjusted to better compare with the mechanical behavior of the as-annealed material (Figure 7.5). The equivalent plastic strain developed during cold rolling was therefore readjusted to 14% (0˚ to RD),16% (45˚), and 13% (90˚) to best match the work hardening rates to that of the as-annealed material (Figure 7.5). It can be observed that the sample tested at 0˚ to RD falls directly on top of the as-annealed tensile curve when this is done. For the sample tested at 45˚ to RD, the flow stress starts slightly higher at the onset of plastic deformation but seems to rapidly return to the as-annealed behavior. For the sample tested at 90˚ to RD, a much more significant change seems to be induced by cold rolling. Therefore, it was not possible to find a strain that would allow its behavior to match that of the as-annealed material. This might have been because diffuse necking started from the onset of plastic deformation. Similar behavior for samples tested at 90˚ to RD compared to as-tensile tested samples have been reported in the literature [117].

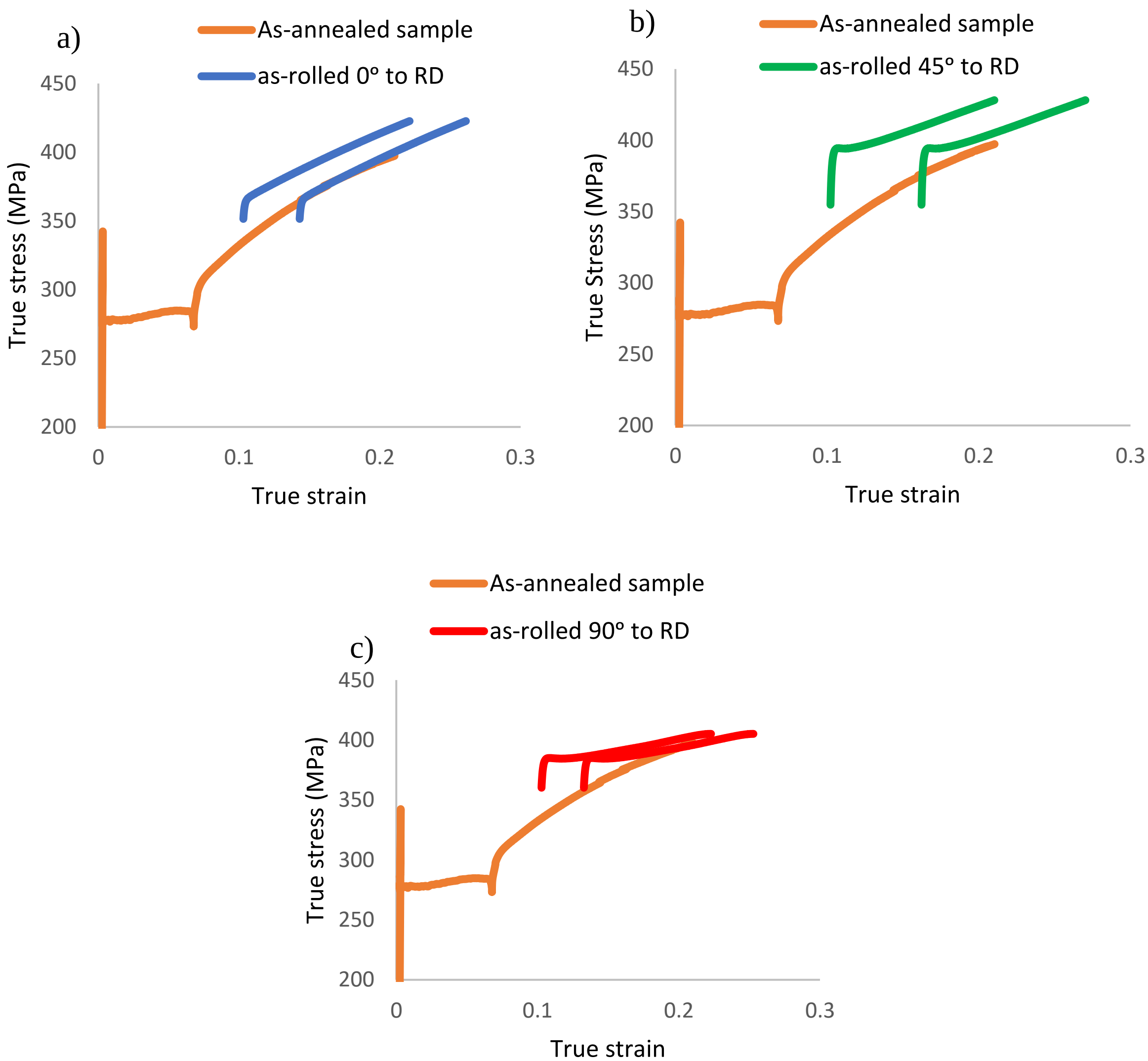

Figure 7-5: The effect of adjusting the magnitude of the equivalent plastic strain for the a) 0˚, b) 45˚ and c) 90˚ to RD tests to better match the work hardening rates of the as-annealed material.

The difference in pre-strain levels between annealed and as-rolled samples means it is most reasonable to compare the yield stress on re-loading in tension after rolling and aging to the yield stress measured from tensile testing the as-rolled sheet, which is obtained as the 0.2% offset yield stress. This is done from this point on.

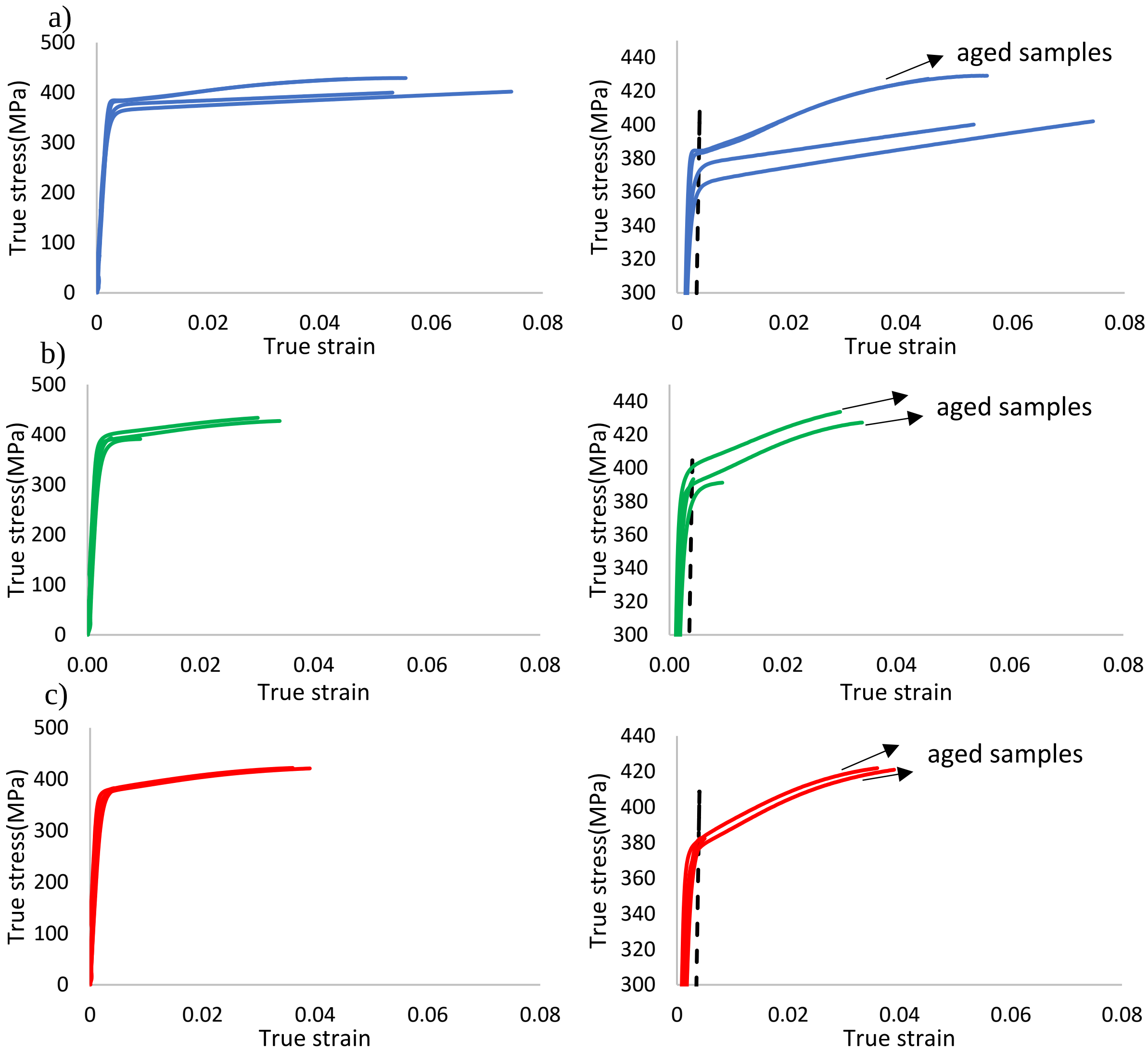

Figure 7-6: Mechanical behavior of tensile samples loaded at a) 0˚ from RD, b) 45˚ from RD and c) 90˚ from RD after cold rolling with no aging treatment and after aging treatment. The figures on the left-hand side show the complete stress-strain curves to necking while those on the right side highlight the behavior close to yield.

Figure 7.6 shows two important features of the directionality of strain aging in ULC steels. First, the change in yield stress is much smaller on aging of rolled samples compared to tensile pre-deformed samples. The 0˚ to RD samples were the only ones to show a measurable change in yield stress after aging treatment (approximately 25 MPa). This is about half of the increase in yield stress during strain aging tests made with tensile pre-straining (Chapter 5 and 6). Second, strain aging significantly changes the work hardening behavior of these materials. This finding is just the opposite to what was observed during monotonic tensile tests, where work hardening rate declined after aging (Figure 7.7a). The decrease in work hardening rate following aging of samples tested in monotonic tension has also been reported in the literature [91]. In comparison Figure 7.7 shows that aging after cold rolling increases the work hardening rate at yield by a factor of ~ 2 compared to the work hardening rate of the as-rolled samples at yield (Figure 7.7b).

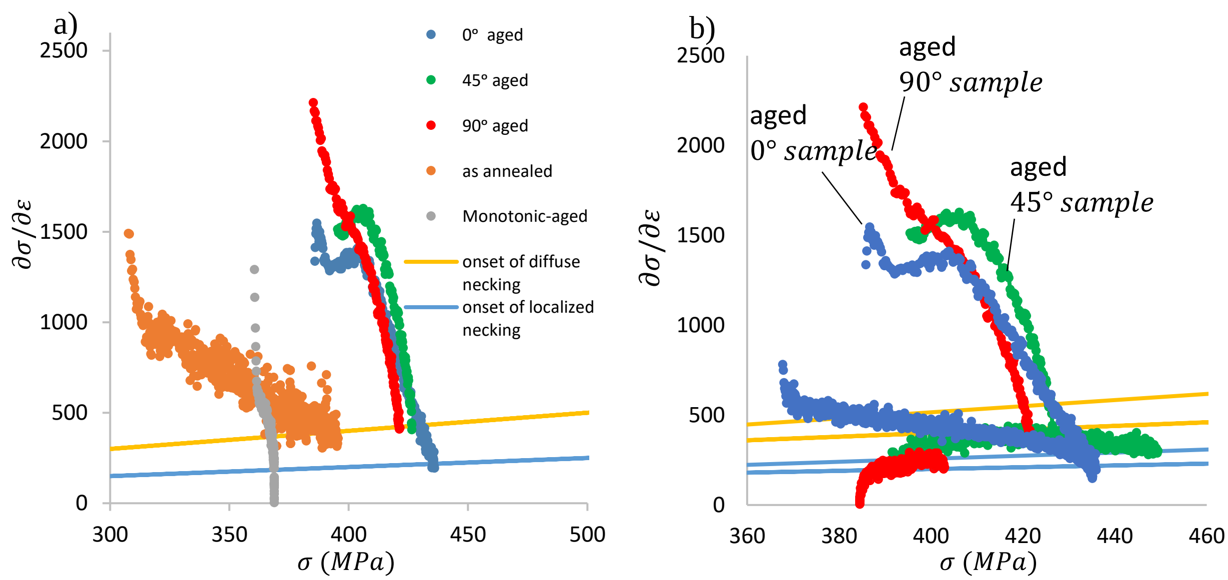

Figure 7-7: Comparison of the work hardening rate between a) tensile samples (as-annealed and aged) and rolled, aged, and retested in tension samples (0˚, 45˚ and 90˚ to RD) and b) rolled samples (aged and not aged) retested in different directions.

In summary, strain aging affects the mechanical behavior of ULC steels tested following rolling differently from what was observed for samples pre-deformed in tension. Strain aging following rolling leads to a large change in work hardening rate and a small effect on the yield strength. The effect of aging and strain path change on the work hardening rate has had little attention in the literature if compared to the increase in yield stress in monotonic tensile tests. Few observations are reported after aging and strain reversal where a much greater change in flow stress compared to monotonic tensile is observed after aging [8], [20].

7.3.1 Mesoscopic mechanical behavior of ULC steels

As seen in Figure 7.6, samples deformed in different directions after rolling and aging do not show any of the characteristic features of strain aging seen in chapter 5 for the case of monotonic tensile tests, i.e. no evidence of upper yield stress, lower yield stress, or yield point elongation. However, the stress-strain curves at yield do show a lower work hardening rate at yield, particularly the sample tested parallel to RD after aging. Therefore, DIC was used to evaluate the homogeneity of plastic deformation at the onset of yielding in these rolled and aged samples.

Samples tested at 0˚ to RD did exhibit some heterogeneity of the strain along the gauge length following yielding (Figure 7.8). Similar observations have been related to the formation of “complex Lüders bands” in the literature [82]. It is noticeable, however, that the strain heterogeneity remains fixed in one location and does not propagate like a Lüders band. The magnitude of the strain also does not appear to concentrate further in this region and so does not seem to indicate the formation of a neck. Further study would be required to better understand this observation, but it does not change the discussion presented below.

The other two samples tested at 45 and 90º to RD did not show any evidence of strain heterogeneity as shown in Figure 7.9 and 7.10.

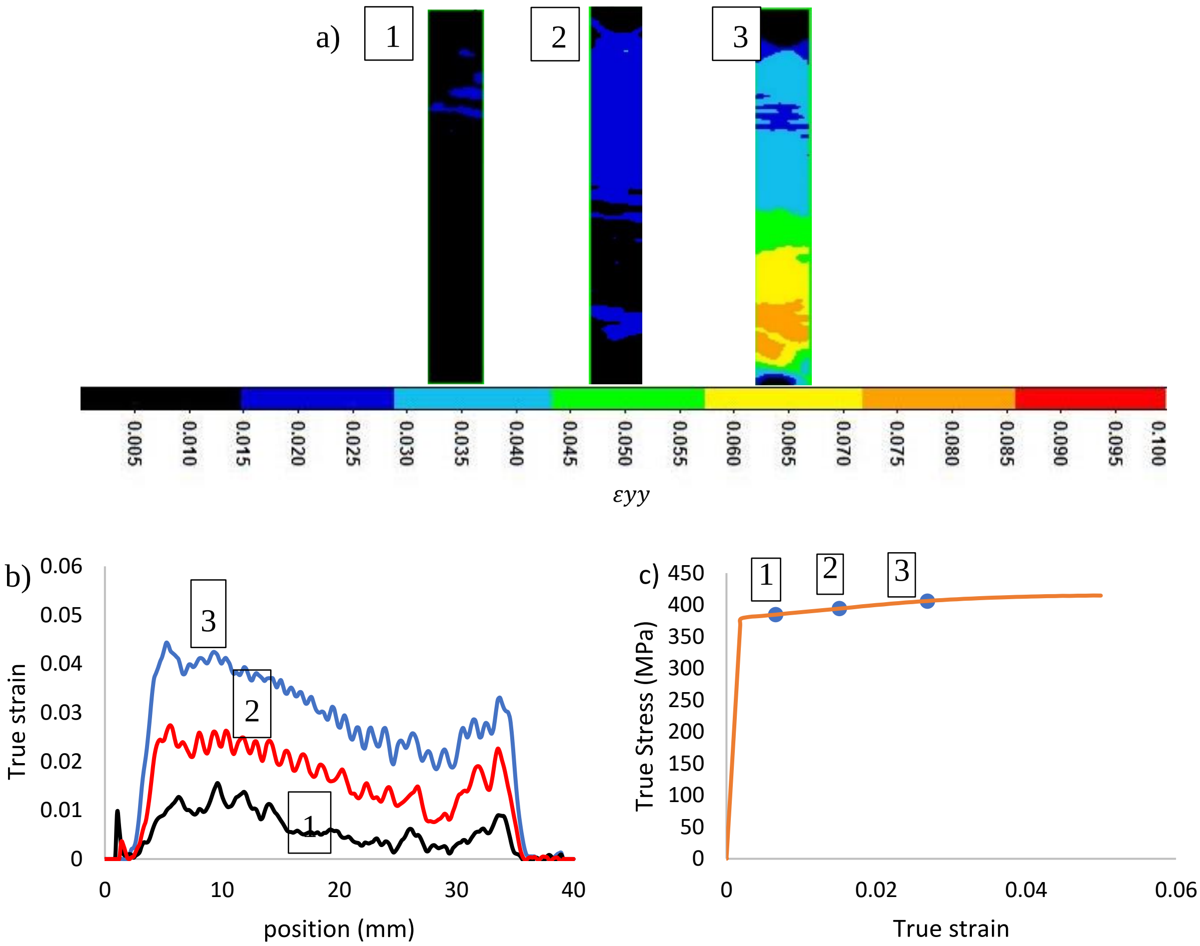

Figure 7-8: Investigation of Lüders band formation during reloading in the RD direction after cold rolling and aging at 150ºC for 10 minutes. The numbers in (a) and (b) correspond to the positions on the macroscopic tensile curve shown in (c).

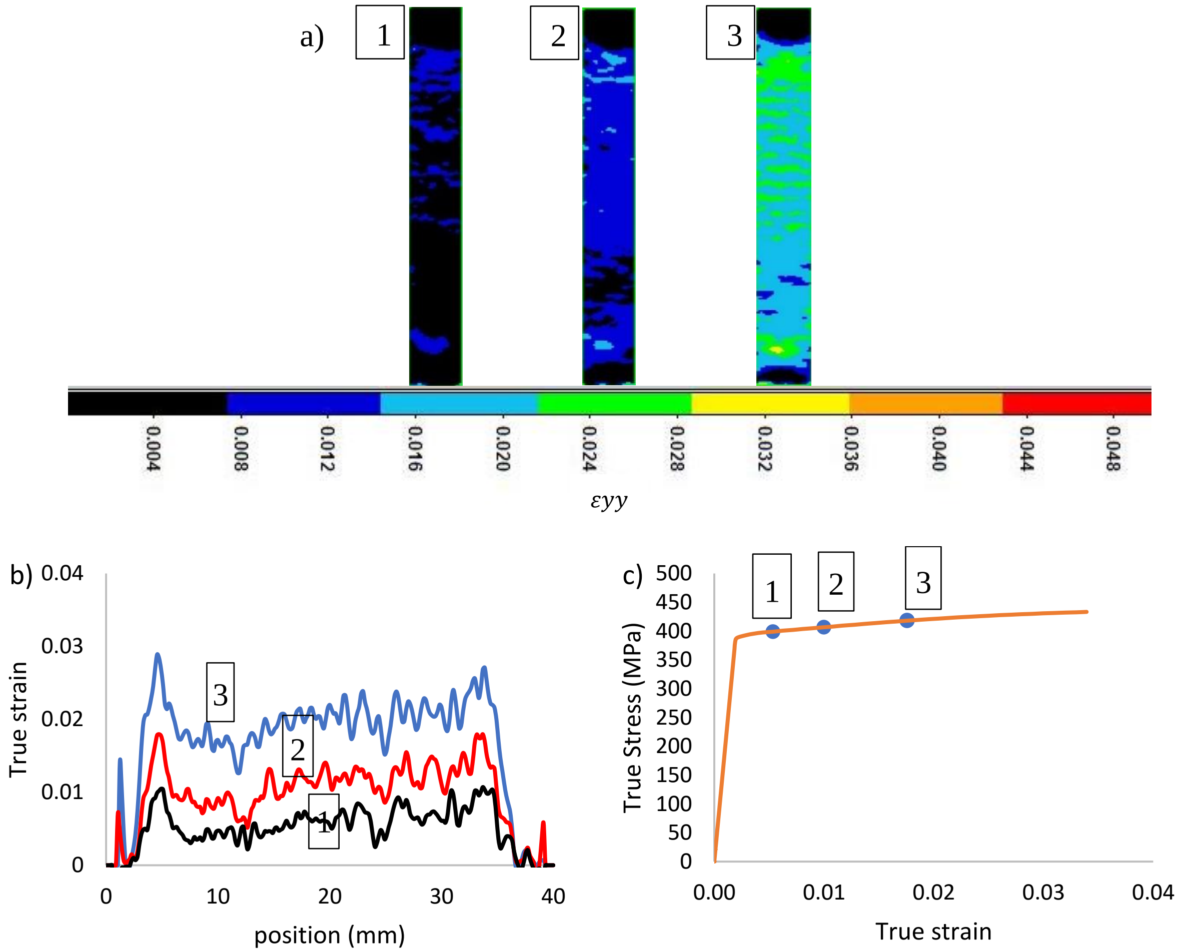

Figure 7-9: Investigation of Lüders band formation during reloading at 45º from RD direction after cold rolling and aging at 150ºC for 10 minutes. The numbers in (a) and (b) correspond to the positions on the macroscopic tensile curve shown in (c).

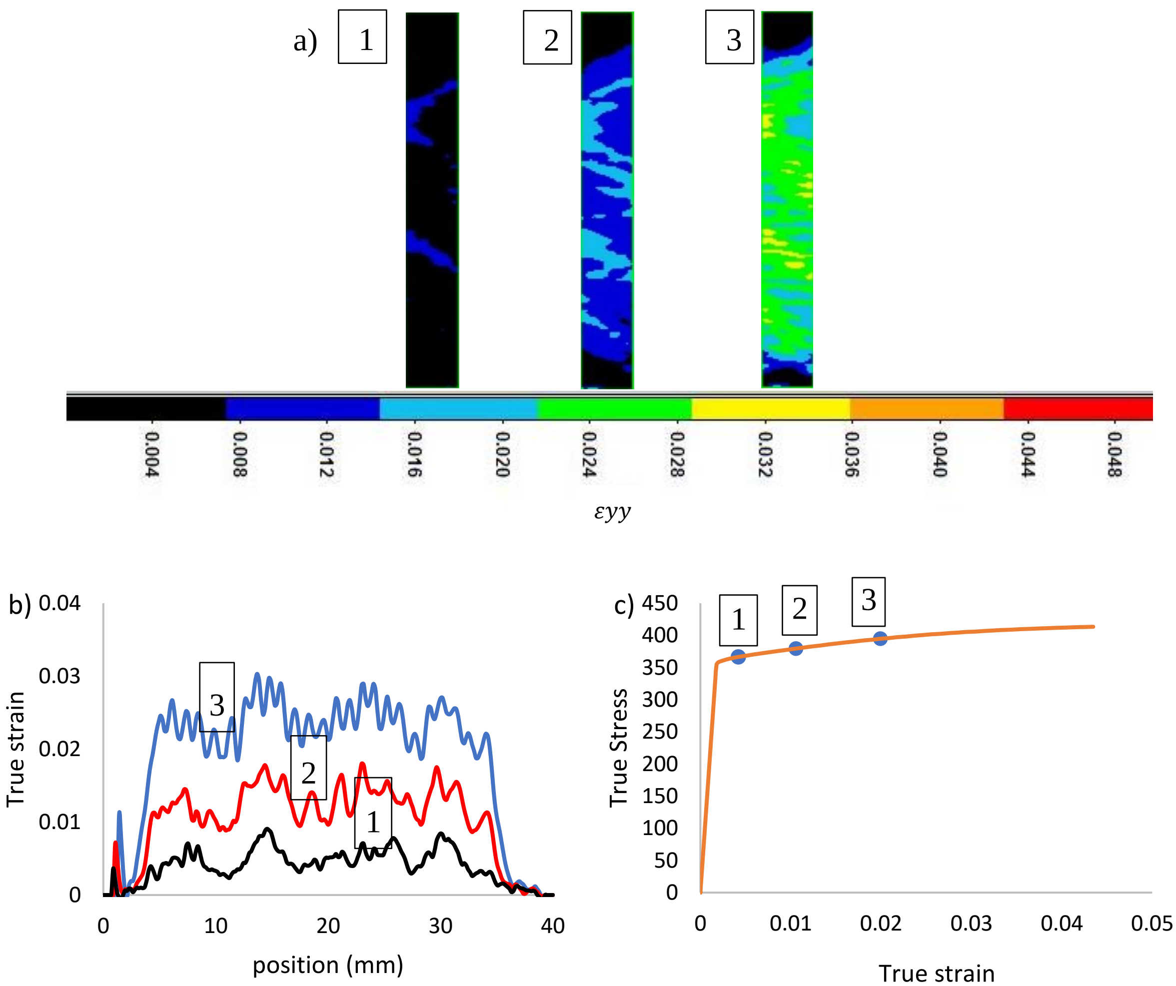

Figure 7-10: Investigation of Lüders band formation during reloading at 90º from RD direction after cold rolling and aging at 150ºC for 10 minutes. The numbers in (a) and (b) correspond to the positions on the macroscopic tensile curve shown in (c).

7.4 Modeling the mechanical behavior of ULC steels as a function of test direction

This section aims to develop a constitutive model to predict the flow stress and work hardening rate of the ULC steels presented above. Unlike the model presented earlier in the thesis, a physically based model using a modification of the Kock-Mecking model will be used to fit the mechanical behavior of ULC steels before and after aging treatment. Finally, the model is tested against the mechanical behavior of the samples from Chapter 6 to show that this approach could be applied to a wide range of conditions.

7.4.1 Model

The model used here is an adapted version of the model recently presented by Medrano [118] which itself is based on the original work of Hahn [37]. In the case of Hahn's model, the effects of strain aging were linked to the reduction of mobile dislocations due to locking of dislocations. Medrano [119] made an additional contribution from the effects of a change to the effectiveness of dislocations at storing forest dislocations and therefore changing the work hardening rate following strain aging. In this case Medrano's approach uses a modified version of the Kocks and Mecking [120] model (KM) to account for both mobile and forest dislocation density, which play different roles during plastic deformation. Using this approach, the flow stress is written as a function of the forest dislocation density (ρ_f) and the imposed strain rate ($\dot{\varepsilon}$) as,

$$\sigma = \sigma_o + M\alpha G b\sqrt{\rho_f}\left(\frac{\dot{\varepsilon}}{\dot{\varepsilon}_o}\right)^m (7.1)$$

Where σ_o is a friction stress, M is the Taylor factor, α is a constant and $\dot{\varepsilon}_o$ is a reference strain rate which is assumed proportional to the mobile dislocation density $\dot{\varepsilon}_o = \beta^*\rho_m$ [121]. The mobile dislocation density is assumed to evolve to a saturation value ρ_m^{sat} at a rate controlled by the parameter η.

$$\frac{\partial \rho_m}{\partial \varepsilon} = \eta \rho_m^{sat} \left(1 - \frac{\rho_m}{\rho_m^{sat}}\right) \text{ (7.2)}$$

The evolution of forest dislocation density is given by the competition between dislocation storage and annihilation,

$$\frac{\partial \rho_f}{\partial \varepsilon} = K3\sqrt{\rho_f} - K4\rho_f \text{ (7.3)}$$

Here K3 and K4 are parameters that are fit to match the experimental stress-strain response.

Equations 7.1-7.3 should allow for the prediction of the stress-strain response of a material with no strain aging. In the case of ULC steel, the as-annealed material already shows the effects of aging in the upper yield stress and yield point elongation. Thus, the equations were fit to match the stress strain response (using the parameters in Table 7.3) at strains beyond the Lüders plateau (Figure 7.11). It is important to notice that η is a fitting parameter associated with the generation rate of mobile dislocations. This parameter becomes important after aging where mobile dislocations developed during pre-loading are assumed to be locked, and new mobile dislocations are created during reloading. For instance, a small η during reloading causes the generation rate of mobile dislocation to drop, which increases the work hardening rate of the tested material. For the fitting shown in Figure 7.11 it was assumed that the mobile dislocation density was already at its saturation value (discussed below) so that the value of η is not important.

Table 7-3: Parameters used for modeling.

Parameter	Value	Description
	Material Parameters	
b	0.205nm	Burgers vector
G	80 GPa	Shear modulus
M	3	Taylor factor
alpha	0.35	pre-factor in Taylor equation
m	0.02	rate sensitivity
	Hardening Parameters (as-annealed)	
σ_o	175 MPa	initial yield stress
K3	$1.85\ x\ 10^8 m^{-1}$	hardening fitting parameter
K4	9.8	softening fitting parameter
	Hardening Parameters (aged after cold rolling)	
K30	$2x10^8 m^{-1}$	locking of ρ_{f0} parameter
K40	19	recovering of ρ_{f0} parameter
η	$5x10^{13}$	generation rate of ρ_m

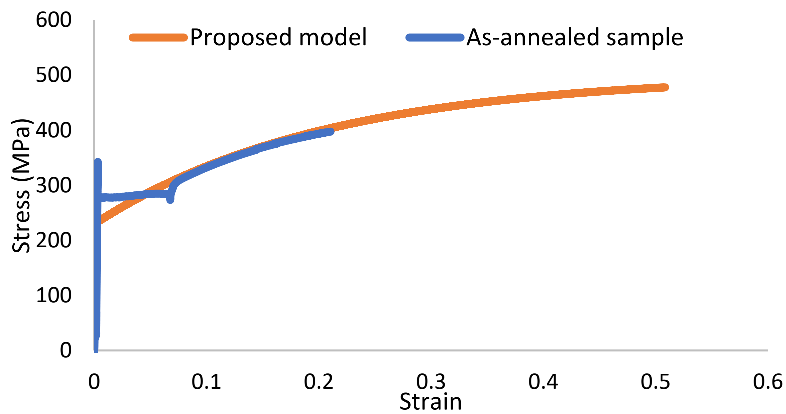

Figure 7-11: Modeling as-annealed mechanical behavior using the proposed model.

7.4.2 Changing the deformation path after cold rolling

The change in deformation path has been reported to affect the microstructure, causing a change in yield stress and flow stress [7], [61], [62]. For instance, when the second deformation path is orthogonal to first direction, an increase in flow stress is expected. According to literature, when the second deformation is orthogonal to the first, an increase in the yield stress is expected [5], [68]. This is caused by the need for new slip systems to be active, these being obstructed by the presence of the dislocations stored in the first deformation[5], [122].

The effect of strain path change on the yield stress observed in this study is less than that reported for other steels [5], [7], [61], [62]. Figure 7.12 compares the results found in this work with work on low carbon steels where the strain path change was obtained by tensile pre-strain followed by the preparation of new tensile samples at various angles from the prior tensile direction [63]. In this figure σ_β is the stress at the tested angle and σ_ρ is the flow stress at the end of the pre-deformation. For this study the maximum difference in stress between the tested direction was 5%.

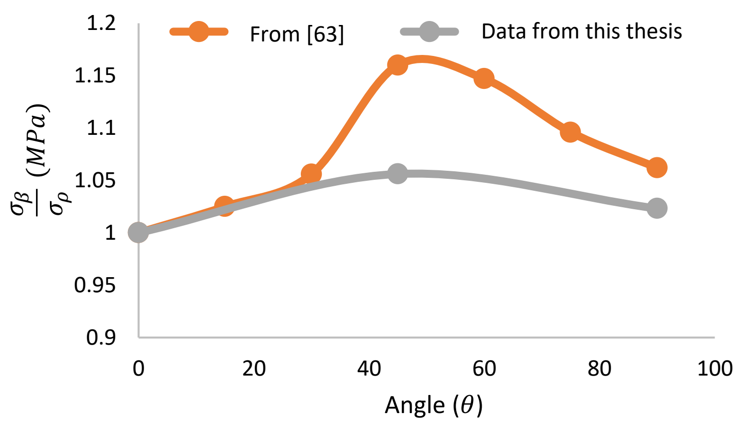

Figure 7-12: Ratio of the subsequent yield stress σ_β to the yield stress along a monotonic tensile test σ_ρ [63].

Because of the small strain path effect shown here it will be assumed that the Kocks-Mecking behavior (Figure 7.4) can be used for describing the response of all the rolled samples (Figure 7.13). An important reason for doing this is that it allows for one to predict the forest dislocation density at the end of pre-straining in rolling. This is reported in Table 7.4. In this case the mobile dislocation is simply assumed to be constant ($\rho_m = \rho_m^s$). These will be used as inputs to the aging model described below.

Table 7-4: Prediction of dislocation density at the onset of plastic deformation during cold rolling using the proposed model.

Direction	$\rho_f (m^{-2})$	$\rho_m (m^{-2})$
0˚	$1.20x10^{14}$	$1.00x10^{13}$
45˚	$1.37x10^{14}$	$1.00x10^{13}$
90˚	$1.11x10^{14}$	$1.00x10^{13}$

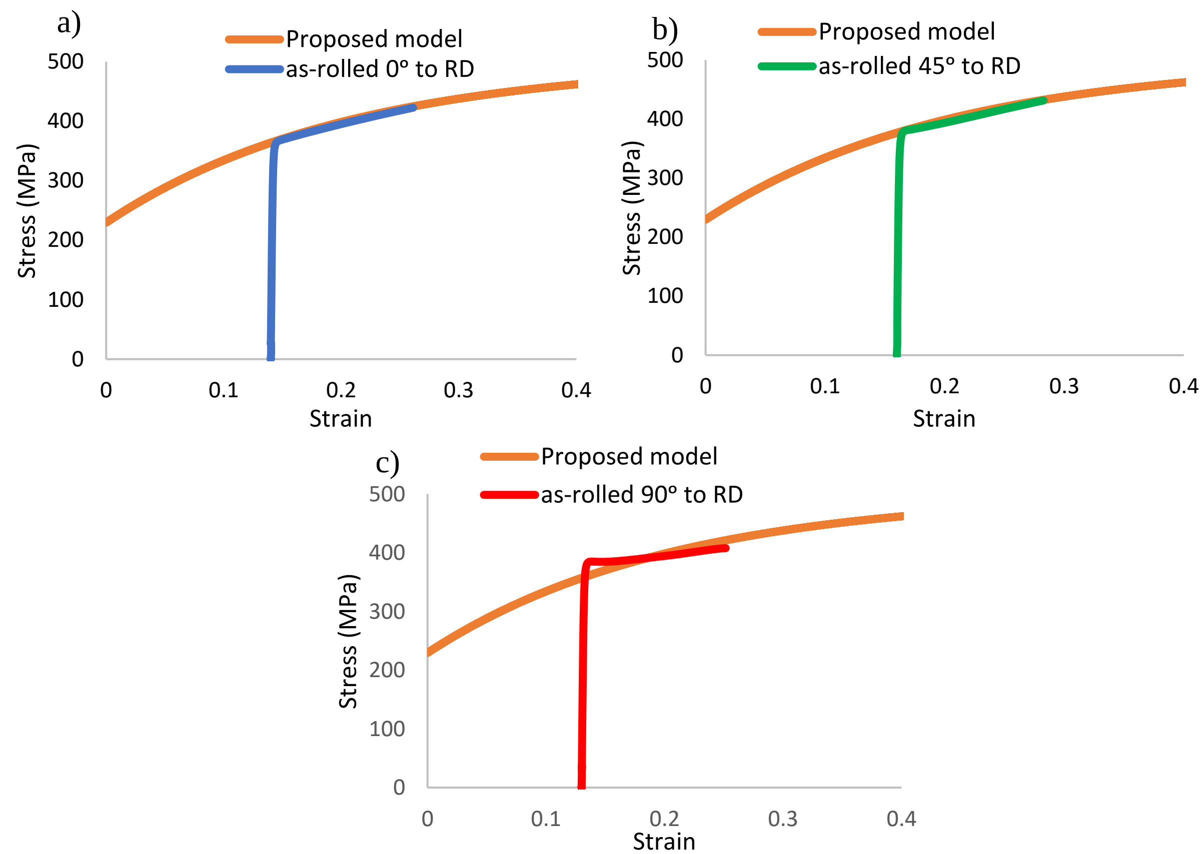

Figure 7-13: Using the proposed model to fit as-rolled a) 0˚ to RD, b) 45˚ RD and c) 90˚ to RD.

7.4.3 Accounting for the effects of strain aging

After aging, it was shown that the samples tested in different directions had a change in their work hardening rate (Figure 7.7). Normally, a Kocks-Mecking model [120] would predict that the work hardening rate is an increasing function of the dislocation density. Given the low aging temperature used here it is surprising that there would be any change in the dislocation density and therefore the work hardening rate.

Here, following Hahn and Medrano [37], [119], the effect of aging is assumed to make two contributions to the dislocation density. First, like in the model of Hahn, it is assumed that aging causes solute to segregate to dislocations making many of the mobile dislocations, from the pre-deformation, immobile. This reduces the reference strain rate in equation 7.1, therefore, increasing the stress required for achieving the imposed strain rate. As plastic deformation proceeds the mobile dislocation density recovers according to equation 7.2. The second effect of aging, following Medrano [119] is that forest dislocations formed during pre-deformation are locked during aging by segregation of solute. This changes their rate of dynamic recovery and their capacity to trap other forest dislocations after reloading in a different deformation path. To account for this, equation 7.3 is modified to:

$$\frac{\partial \rho_f}{\partial \varepsilon} = K30\sqrt{\rho_{f0}} + K3\sqrt{\rho_f} - K4\rho_f \quad (7.4)$$

Where K30 is a new fitting parameter and $\rho_{f0}$is the density of locked forest dislocation. To account for the gradual removal of the locked dislocations by deformation in the new deformation path [6], [7], [68], [123], ρ_{f0} is assumed to follow an equation,

$$\frac{\partial \rho_{f0}}{\partial \varepsilon} = -K40\, \rho_{f0} \left[1 - \exp\left(-\sqrt{\frac{\rho_{f0}}{\rho_f}}\right)\right] \quad (7.5)$$

The term in the square bracket accounts for the probability of annihilation [119].

This new model requires two new material parameters ($K30$ and $K40$) as well as the fraction of forest and mobile dislocations that are locked by solute. The values of K30 and K40 are given in table 7.4. A single set of parameters were used for all three of the testing directions following aging. The fraction of locked forest dislocations ($f - \rho_{f0}$) and available mobile dislocations ($f - \rho_m$) were adjusted for each of the testing directions. The values found to give the best results are given in Table 7.5. Using these values, the predicted stress-strain response for the re-loaded samples is shown in Figure 7.14.

Table 7-5: Shows the used fractions of locked forest dislocations and available mobile dislocations after aging treatment.

Direction	$f - \rho_{f0}$	$f - \rho_m$
0°	0.75	0.01
45°	0.8	0.05
90°	0.9	0.015

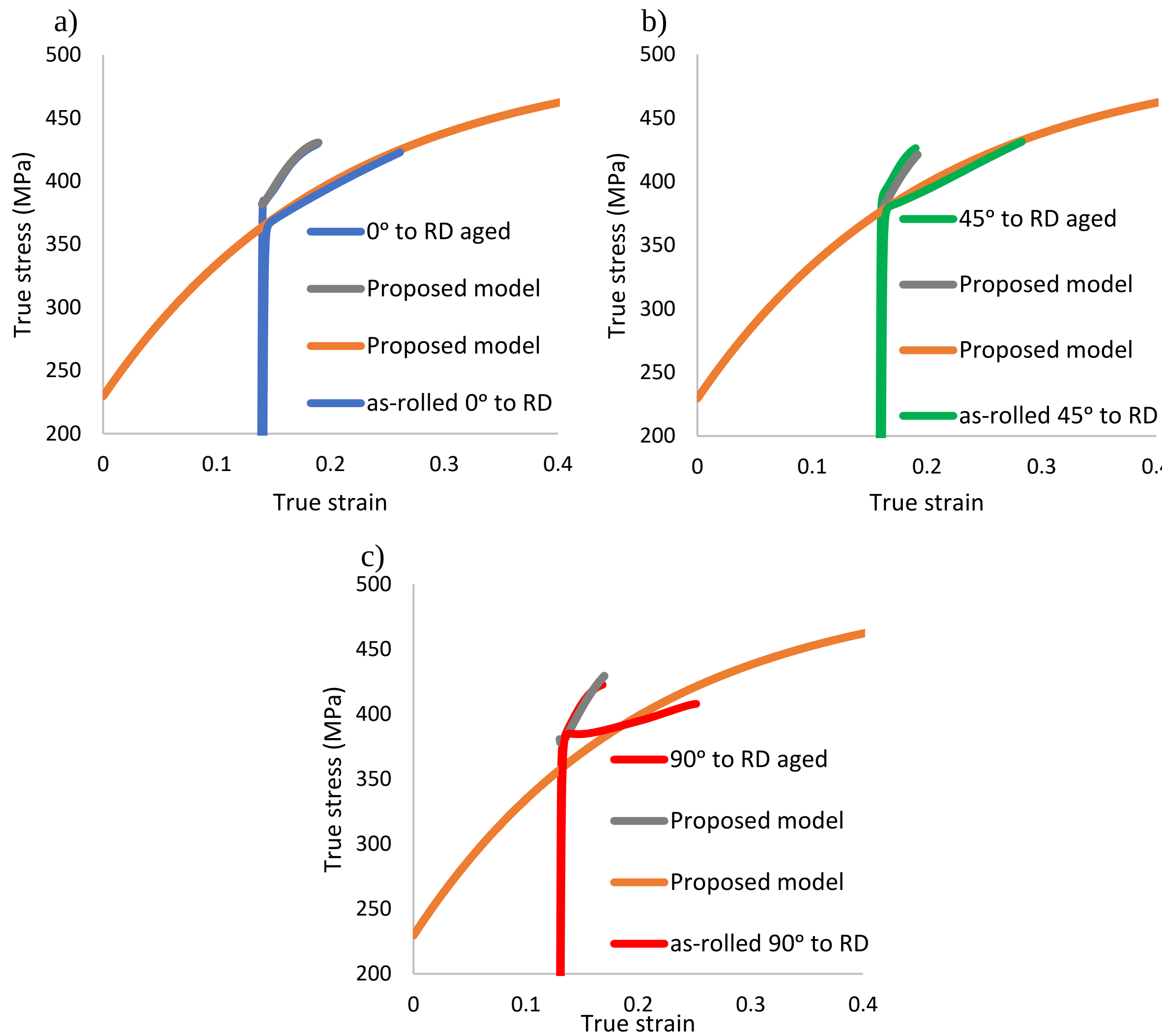

Figure 7-14: Using the proposed model to predict the mechanical behavior of rolled and aged samples re-tested at a) 0˚ to RD, b) 45˚ RD and c) 90˚ to RD.

As seen in Figure 7.14, this model is able to predict the behavior of ULC steels reloaded in different directions after aging well. This prediction would not possible using the model presented in Chapter 6. The current model allows one to control both mobile and forest dislocation densities during plastic deformation. After aging, the mobile dislocation density controls the increase in yield stress, i.e. the decrease in the mobile dislocation density increases the yield stress up to a saturation point. In the case of non-monotonic deformation paths, the mobile dislocation density appears to not be reduced enough to cause an increase in yield stress after strain aging. On the other hand, the increase of forest dislocation density locked after aging was found to greatly affect the work hardening rate. This played a crucial role in the prediction of the mechanical behavior after aging.

7.4.4 Predicting behavior under monotonic deformation

In Chapter 6 a constitutive model combined with finite simulations was used to predict the stress-strain response of ULC steels when Lüders band formation occurred after aging. If the model presented in the previous section is to be useful, it should also be possible for it to be used to predict the results presented in Chapter 6. This would have the benefit of bringing a more physically based model to the prediction of the monotonic behavior of ULC steels following strain aging.

It was described above that the Kocks-Mecking model could only predict the as-annealed flow stress and work hardening behavior after the end of the Lüder's plateau (Figure 7.11). However, if the additional effects of strain aging introduced above are considered it is also possible to reasonably well predict the stress-strain curve including the Lüders deformation when coupled with finite element simulation. In order to do this, the model presented in the previous section was coupled to the finite element simulation used in Chapter 6. For simplification, strain rate was assumed to constant during FE simulation. This is a poor assumption, especially at the

Lüders front where the strain rate is much higher than that imposed experimentally[41], [45]. However, as a first illustration of the value of this model it has been neglected here. All of the parameters in Table 7.3 were used but the initial dislocation densities were selected as shown in Table 7.6. Figure 7.15 shows the resulting constitutive law coupled with finite element simulation. In order to well approximate the upper yield point the initial mobile dislocation density had to be set to a very low value, this consistent with the suggestions of Johnson and Gilman[36].

Table 7-6: Prediction of dislocation density at the onset of plastic deformation during pre-deformation and reloading after aging using the proposed model.

Direction	$\rho_f(m^{-2})$	$\rho_m(m^{-2})$	$f-\rho_{f0}$	$f-\rho_m$
As- annealed	$1.35x10^{13}$	≈ 0	-----	-----
Aged	$8.28x10^{13}$	$1.00x10^{13}$	0.3	0.0001

Overall, the model does an excellent job of predicting the upper and lower yield stresses though it under predicts the yield point elongation. One of the reasons for the underprediction of yield point elongation may be because this simulation did not account for strain rate dependency at the Lüders band front as described above. In this way, this problem may be solved by incorporating the effect of local strain rate during FEM simulation. This could be achieved by creating a VUHARD routine like the one used for the model presented in Chapter 6.

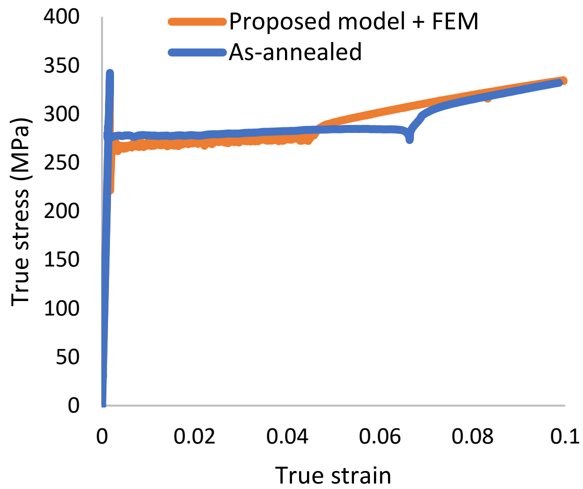

Figure 7-15: Using the proposed model and FEM to predict the non-uniform plastic deformation region of ULC steels.

Having shown that this model can be used to predict the stress-strain response of the as-annealed material it was next checked to see if it could predict the behavior of tensile pre-deformed, aged and re-tested in tension samples presented in Chapter 6. Here, as an illustration, only one case (aged to full capacity sample) is fit using the model described above. The fit obtained to the experimental stress-strain curve using the model combined with finite element simulation is shown in Figure 7.16. The values of the parameters used to make this fit are shown in Table 7.3.

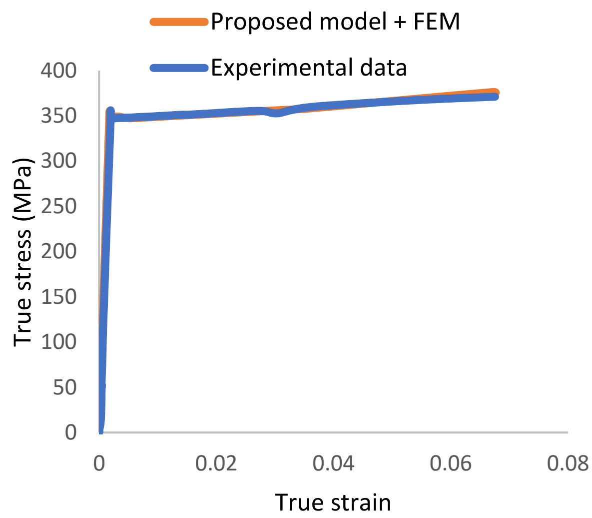

Figure 7-16: Fitting aged monotonic tensile test behavior by the proposed model combined with FEM.

In this case, aging increases the yield stress but decreases the work hardening rate. This is opposite of what was observed for the samples that were aged after rolling. In that case, the most important modification of Kocks-Mecking model was the locked forest dislocation density that serves as strong obstacles for dislocations moving in the new deformation path. For the case of tensile pre-strain followed by aging and re-testing in tension the present model would indicate that these locked forest dislocations act as much less strong obstacles, or that the fraction of these locked dislocations is much lower. The important contribution in this case comes from the need for almost all mobile dislocations to be locked in order for one to achieve the correct upper-yield stress.

In summary, the physically based model, a version of the Hahn and Medrano models [37], [119], has been shown to well predict the stress-strain response for the different test conditions studied in this thesis. This provides a more physically motivated alternative to the model used in Chapter 6. While both models can predict the mechanical behavior of ULC steels during pre-deformation and after aging treatment and reloading in same direction, only the model presented in this chapter can predict the response following strain path changes. Future work should investigate the efficiency of this model when tested in different materials after aging and reloading in different directions. Also, this model can be used to study the effect of strain rate on the flow stress of samples presenting non-uniform plastic deformation due to Lüders band formation and propagation. This can be done by using VUHARD subroutines during FEM simulation, similarly to what has been presented in chapter 6.

Chapter 8: Conclusion and future work

8.1 Conclusion

This thesis has contributed to improving our understanding of strain aging in ULC steels, particularly with respect to the effect of strain path change. Analytical models used for predicting the effects of strain aging have been validated in combination with finite element simulations. A new, physically motivated model has been shown to be useful for all of the conditions studied here.

In Chapter 5, an analytical model was used to characterize the kinetics of strain aging for monotonic tensile results. This used the Loaut-Cottrel model. This model was shown to predict the upper and lower yield strength after strain aging for different temperatures and times for the studied steel.

The results presented in Chapter 5 were then used with a constitutive law from the literature and finite element simulations to allow for the prediction of the full stress-strain response of monotonically pre-deformed samples. The mesoscopic behavior associated with Lüders band formation and propagation was also shown to be well reproduced by comparison of finite element simulations and experimental digital image correlation results.

Finally, samples pre-deformed in rolling and tested in different directions compared to the rolling direction after aging have shown to behave very differently compared to samples deformed in tension. The rolled and aged samples did not exhibit an upper and lower yield stress, and yield point elongation, but rather showed a large increase in work hardening rate. A physically based model was used in this case and shown to be able to reproduce the observations. This model was also shown to be capable of predicting the results of samples pre-tested in tension. The main advantage of this model compared to the one used earlier in the thesis is that it can be directly related to physical processes expected to be important in the material.

8.2 Future work

1. Complementary studies of strain aging and deformation history should be performed. In particular, the effect of cold rolling pre-deformation level on the mechanical behavior before and after aging should be studied.
2. A detailed study of the microstructure, e.g. the formation of microbands [5], should be undertaken. This would allow the various predictions of the model presented in chapter 7 to be studied. Transmission electron microscopy would be very useful in this case [67].
3. The effect of strain aging in conditions where the materials have much more complex microstructures, e.g. high strength low alloy steels and TRIP steels, should be investigated in terms of the effect of strain path on strain aging. For instance, the model proposed in Chapter 7 could be used to predict the mechanical response in such materials.
4. Perform other sorts of pre-straining tests rather than rolling. For instance, one could pull large samples during loading, cut tensile samples at different angles from RD, and reload

them after aging. This would easy the control of the pre-deformation level which is one of the challenges found during cold rolling.

5. Investigate the point where Lüders bands nucleates in ULC steels and other materials. This can be done by investigating the thermal and strain fields associated with Lüders bands formation. The DIC technique with appropriate spatial resolution and acquisition rate can be used to investigate strain fields around Lüders bands, and infrared thermography (IRT) can be used to study the thermal fields associated with Lüders bands nucleation and propagation.

Bibliography

[1] S. Berbenni, V. Favier, X. Lemoine, and M. Berveiller, “A micromechanical approach to model the bake hardening effect for low carbon steels,” *Scr. Mater.*, vol. 51, no. 4, pp. 303–308, 2004.

[2] H. Alihosseini and K. Dehghani, “Bake hardening of ultra-fine grained low carbon steel produced by constrained groove pressing,” *Mater. Sci. Eng. A*, vol. 549, pp. 157–162, 2012.

[3] L. J. Baker, S. R. Daniel, and J. D. Parker, “Metallurgy and processing of ultralow carbon bake hardening steels,” *Mater. Sci. Technol.*, vol. 18, no. 4, pp. 355–368, 2002.

[4] V. Ballarin, A. Perlade, X. Lemoine, O. Bouaziz, and S. Forest, “Mechanisms and modeling of bake-hardening steels: Part II. Complex loading paths,” *Metall. Mater. Trans. A Phys. Metall. Mater. Sci.*, vol. 40, no. 6, pp. 1375–1382, 2009.

[5] S. Hiwatashi and S. Yonemura, “Anisotropic Increase in Yield Strength by Straining and Baking of Bake-Hardenable Steel,” *Mater. Sci. Forum*, vol. 495–497, pp. 1485–1492, 2009.

[6] E. V. Nesterova, B. Bacroix, and C. Teodosiu, “Experimental observation of microstructure evolution under strain-path changes in low-carbon IF steel,” *Mater. Sci. Eng. A*, vol. 309, no. 310, pp. 495–499, 2001.

[7] W. Wen *et al.*, “Mechanical behavior of low carbon steel subjected to strain path changes: Experiments and modeling,” *Acta Mater.*, vol. 111, pp. 305–314, 2016.

[8] M. D. Richards, E. S. Drexler, and J. R. Fekete, “Aging-induced anisotropy of mechanical properties in steel products: Implications for the measurement of engineering properties,” *Mater. Sci. Eng. A*, vol. 529, no. 1, pp. 184–191, 2011.

[9] S. Zhao, C. Meng, F. Mao, W. Hu, and G. Gottstein, “Influence of severe plastic deformation on dynamic strain aging of ultrafine grained Al-Mg alloys,” *Acta Mater.*, vol. 76, pp. 54–67, 2014.

[10] Z. Fu, “A study of static strain aging of selected ferritic,” M.S thesis, Tempere University of Technology, Hervanta, 2017.

[11] Georgy E. Dieter, *Mechanical metallurgy*, Second. McGraw-Hill, 1986.

[12] I. S. Kim and S. S. Kang, “Dynamic strain aging in SA508-class 3 pressure vessel steel,” *Int. J. Press. Vessel. Pip.*, vol. 62, no. 2, pp. 123–129, 1995.

[13] A. K. Taheri, T. M. MacCagno, and J. J. Jonas, “Dynamic strain aging and the wire drawing of low carbon steel rods,” *ISIJ Int.*, vol. 35, no. 12, pp. 1532–1540, 1995.

[14] Roger N.Wright, *Relevant aspects of carbon and low-alloy steel metallurgy*, Second. Elsevier, 2016.

[15] S. G. Hong and S. B. Lee, “Mechanism of dynamic strain aging and characterization of its effect on the low-cycle fatigue behavior in type 316L stainless steel,” *J. Nucl. Mater.*, vol. 340, pp. 307–314, 2005.

[16] A. K. De, B. C. De Cooman, and S. Vandeputte, “Kinetics of strain aging in bake hardening ultra low carbon steel-a comparison with low carbon steel,” *J. Mater. Eng. Perform.*, vol. 10, no. 5, pp. 567–575, 2001.

[17] S. Gündüz, B. Demir, and R. Kaçar, “Effect of aging temperature and martensite by volume on strain aging behaviour of dual phase steel,” *Ironmak. Steelmak.*, vol. 35, no. 1, pp. 63–68, 2008.

[18] A. Bülbül, R. Kaçar, A. Bülbül, and R. Kaçar, “Factors affecting kinetics of strain aging in S275JRC steel,” *Mater. Res.*, vol. 20, no. 1, pp. 210–217, 2016.

[19] A. K. De, S. Vandeputte, and B. C. De Cooman, “Static strain aging behavior of ultra low carbon bake hardening steel,” *Scr. Mater.*, vol. 41, no. 8, pp. 831–837, 1999.

[20] Q. Lai, C. W. Sinclair, and W. J. Poole, “The anisotropic kinetics of strain aging in a martensitic steel,” *Can. Metall. Q.*, vol. 57, no. 1, pp. 20–27, Jan. 2018.

[21] J. Z. Zhao, A. K. De, and B. C. De Cooman, “Kinetics of Cottrell atmosphere formation during strain aging of ultra-low carbon steels,” *Mater. Lett.*, vol. 44, no. 6, pp. 374–378, 2000.

[22] V. T. L. Buono, B. M. Gonzalez, and M. S. Andrade, “Strain aging of AISI 430 ferritic stainless steel,” *Scr. Mater.*, vol. 38, no. 2, pp. 185–190, 1997.

[23] A. H. Cottrell and B. A. Bilby, “Dislocation theory of yielding and strain ageing of iron,” *Proc. Phys. Soc. Sect. A*, vol. 62, no. 1, p. 49, 1949.

[24] V. Ballarin, M. Soler, A. Perlade, X. Lemoine, and S. Forest, “Mechanisms and modeling of bake-hardening steels: Part I. Uniaxial tension,” *Metall. Mater. Trans. A Phys. Metall. Mater. Sci.*, vol. 40, no. 6, pp. 1367–1374, 2009.

[25] W. C. Leslie, *The physical metallurgy of steels*. Hempisphere Pub. Corp, 1981.

[26] D. V. Wilson, “Grain-size dependence of discontinuous yielding in strain-aged steels,”

Acta Metall., vol. 16, no. 5, pp. 743–753, 1968.

[27] A.H.Cottrel, *Dislocation and plastic flow in crystals*. London: Oxford University Press, 1953.

[28] J. Z. Zhao, A. K. De, and B. C. De Cooman, “Formation of the Cottrell atmosphere during strain aging of bake-hardenable steels,” *Metall. Mater. Trans. A Phys. Metall. Mater. Sci.*, vol. 32, no. 2, pp. 417–423, 2001.

[29] R. D. A. V. Gomes, “Computational insights into the strain aging in bcc iron at atomic scale.,” Ph.D dissertation, L` Institut National des Science Appliquees de Lyon, Lyon, 2011.

[30] Y. Hanlumyuang, P. A. Gordon, T. Neeraj, and D. C. Chrzan, “Interactions between carbon solutes and dislocations in bcc iron,” *Acta Mater.*, vol. 58, no. 16, pp. 5481–5490, 2010.

[31] H. K. D. H. Bhadeshia, “Carbon in cubic and tetragonal ferrite,” *Philos. Mag.*, vol. 93, no. 28–30, pp. 3714–3725, 2013.

[32] D. J. Bacon, D. M. Barnett, and R. O. Scattergood, “Anisotropic continuum theory of lattice defects,” *Prog. Mater. Sci.*, vol. 23, no. C, pp. 51–262, 1980.

[33] N.Louat, “On the theory of the Portevin-Le Chatelier effect,” *Scr. Metall.*, vol. 15, no. c, pp. 1167–1170, 1981.

[34] A. K. De, K. De Blauwe, S. Vandeputte, and B. C. De Cooman, “Effect of dislocation density on the low temperature aging behavior of an ultra low carbon bake hardening steel,” *J. Alloys Compd.*, vol. 310, no. 1–2, pp. 405–410, 2000.

[35] S. Hartley, “Strain-ageing in tantalum,” *Acta Metall.*, vol. 14, no. 10, pp. 1237–1246, 1966.

[36] J. J. Gilman and W. G. Johnston, “Dislocation velocities, dislocation densities, and plastic flow in lithium fluoride crystals,” *J. Appl. Phys.*, vol. 30, no. 2, pp. 129–144, 1959.

[37] G. T. Hahn, “A model for yielding with special reference to the yield-point phenomena of iron and related bcc metals,” *Acta Metall.*, vol. 10, no. 8, pp. 727–738, 1962.

[38] V. S. Ananthan and E. O. Hall, “Macroscopic aspects of Lüders band deformation in mild steel,” *Acta Met. mater*, vol. 39, no. 12, pp. 3153–3160, 1991.

[39] A.K.De., S. Vandeputte, B. Soenen, and B. C. De Cooman, “Effect of grain size on the static strain aging of ULC-bake hardening steel,” *Zeitschrift für Met. 95*, vol. 8, pp. 713–717, 2004.

[40] J. F. Butler, “Lüders front propagation in low carbon steels,” *J. Mech. Phys. Solids*, vol. 10, no. 4, pp. 313–318, 1962.

[41] T. Brlić, S. Rešković, I. Jandrlić, and F. Skender, “Influence of strain rate on stress changes during Lüders bands formation and propagation,” *IOP Conf. Ser. Mater. Sci. Eng.*, vol. 461, no. 1, 2018.

[42] S. Rešković, I. Jandrlić, and F. Vodopivec, “Influence of testing rate on Lüders band propagation in niobium microalloyed steel,” vol. 55, no. 2, pp. 157–160, 2016.

[43] W. M. Lomer, “The yield phenomenon in polycrystalline mild steel,” *J. Mech. Phys. Solids*, vol. 1, no. 1, 1952.

[44] H. Fujita and S. Miyazaki, “Lüders deformation in polycrystalline iron,” *Acta Met.*

materMetallurgica, vol. 26, pp. 1273–1281, 1978.

[45] J. Zhang and Y. Jiang, “Lüders bands propagation of 1045 steel under multiaxial stress state,” *Int. J. Plast.*, vol. 21, no. 3, pp. 651–670, 2005.

[46] “Analysis of deformation process,” *University of Cambridge*, 204AD. [Online]. Available: https://www.doitpoms.ac.uk/tlplib/metal-forming-3/plane_stress.php.

[47] K. Subramanian and A. Duncan, “Tensile Properties for Application to Type I and II Waste Tank Flaw Stability Analysis,” 2000. [Online]. Available: https://sti.srs.gov/fulltext/tr2000232/tr2000232.html.

[48] L. M. Storozheva, “Ultralow-carbon steels for automotive industry with the effect of hardening upon drying of completed parts,” *Metalloved. i Termicheskaya Obrab. Met.*, vol. 43, no. 9, pp. 9–18, 2001.

[49] T. Okunaga, “Effect of grain size and solid solution the bake hardenability of low carbon strengthening aluminum-killed elements steel*,” *Trans. ISIJ*, vol. 24, no. 17, pp. 17–23, 1984.

[50] Y. Ono *et al.*, “Roles of solute C and grain boundary in strain aging behaviour of fine-grained ultra-low carbon steel sheets,” *Tetsu-to-Hagane*, vol. 105, no. 4, pp. 452–461, 2019.

[51] A. J. Beaudoin, P. R. Dawson, K. K. Mathur, U. F. Kocks, and D. A. Korzekwa, “Application of polycrystal plasticity to sheet forming,” *Comput. Methods Appl. Mech. Eng.*, vol. 117, no. 1–2, pp. 49–70, 1994.

[52] H. R. Wenk and P. Van Houtte, “Texture and anisotropy,” *Reports Prog. Phys.*, vol. 67,

no. 8, pp. 1367–1428, 2004.

[53] T. R. Society, P. Transactions, and E. Sciences, “Deformation microstructures and textures in steels,” *R. Soc.*, vol. 357, no. 1756, pp. 1471–1485, 2011.

[54] D. Raabe, “Texture and microstructure evolution during cold rolling of a strip cast and of a hot rolled austenitic stainless steel,” *Acta Mater.*, vol. 45, no. 3, pp. 1137–1151, 1997.

[55] P. Gobernado, R. Petrov, D. Ruiz, E. Leunis, and L. A. I. Kestens, “Texture evolution in Si-alloyed ultra low-carbon steels after severe plastic deformation,” *Adv. Eng. Mater.*, vol. 12, no. 10, pp. 1077–1081, 2010.

[56] I. Samajdar, B. Verlinden, L. Kestens, and P. Van Houtte, “Physical parameters related to the developments of recrystallization textures in an ultra low carbon steel,” *Acta Mater.*, vol. 47, no. 1, pp. 55–65, 1998.

[57] Z. Zhao, W. Mao, F. Roters, and D. Raabe, “A texture optimization study for minimum earing in aluminium by use of a texture component crystal plasticity finite element method,” *Acta Mater.*, vol. 52, no. 4, pp. 1003–1012, 2004.

[58] V. J. Martínez, J. I. Verdeja, and J. A. Pero-Sanz, “Interstitial free steel: Influence of α-phase hot-rolling and cold-rolling reduction to obtain extra-deep drawing quality,” *Mater. Charact.*, vol. 46, no. 1, pp. 45–53, 2001.

[59] M. Mehdi, Y. He, E. J. Hilinski, and A. Edrisy, “Texture evolution of a 2.8 wt pct Si non-oriented electrical steel and the elimination of the 〈111〉//ND texture,” *Metall. Mater. Trans. A Phys. Metall. Mater. Sci.*, vol. 50, no. 7, pp. 3343–3357, 2019.

[60] J. L. Raphanel, J. H. Schmitt, and B. Baudelet, “Effect of a prestrain on the subsequent

yielding of low carbon steels sheets: experiments and simulations," *Int. J. Plast.*, vol. 2, no. 4, pp. 371–378.

[61] S. Bin Zaman, F. Barlat, and J. H. Kim, "Deformation-induced anisotropy of uniaxially prestrained steel sheets," *Int. J. Solids Struct.*, vol. 134, pp. 20–29, 2018.

[62] M. Härtel, C. Illgen, and M. F. X. Wagner, "Experimental evaluation of Bauschinger effects during tension-compression in-plane deformation of sheet materials," *IOP Conf. Ser. Mater. Sci. Eng.*, vol. 118, no. 1, 2016.

[63] J. L. R. J.H. Schmitt, E.L. Shen, "A parameter for measuring the magnitude of a change of strain path: validation and comparison with experiments on low carbon steel," *Int. J. Plast.*, vol. 10, pp. 535–551, 1994.

[64] R. A. Elliot, E. Orowan, T. Udoguchi, and A. S. Argon, "Absence of yield points in iron on strain reversal after aging, and the Bauschinger overshoot," *Mech. Mater.*, vol. 36, no. 11, pp. 1143–1153, 2004.

[65] D.N.Williams, "Interaction between the Bauschinger effect and strain aging," vol. 11, no. September, pp. 1629–1631, 1980.

[66] A. G. Kostryshev, "Bauschinger effect in Nb and V microalloyed line pipe steels," Ph.D. dissertation, University of Birminghan, Edgbaston, 2009.

[67] S. Thuillier and E. F. Rauch, "Development of microbands in mild steel during cross loading," *Acta Metall. Mater.*, vol. 42, no. 6, pp. 1973–1983, 1994.

[68] M. van Riel and A. H. van den Boogaard, "Stress-strain responses for continuous orthogonal strain path changes with increasing sharpness," *Scr. Mater.*, vol. 57, no. 5, pp.

381–384, 2007.

[69] F. Aguirre, S. Kyriakides, and H. D. Yun, “Bending of steel tubes with Lüders bands,” *Int. J. Plast.*, vol. 20, no. 7, pp. 1199–1225, 2004.

[70] L. J. Baker, J. D. Parker, and S. R. Daniel, “Mechanism of bake hardening in ultralow carbon steel containing niobium and titanium additions,” *Mater. Sci. Technol.*, vol. 18, no. 5, pp. 541–547, 2002.

[71] F. Yoshida, Y. Kaneda, and S. Yamamoto, “A plasticity model describing yield-point phenomena of steels and its application to FE simulation of temper rolling,” *Int. J. Plast.*, vol. 24, no. 10, pp. 1792–1818, 2008.

[72] H. Tsukahara and T. Iung, “Finite element simulation of the Piobert – Lϋders behavior in anuniaxial tensile test,” *Mater. Sci. Eng.*, vol. 248, pp. 304–308, 1998.

[73] J. Belotteau, C. Berdin, S. Forest, A. Parrot, and C. Prioul, “Mechanical behavior modeling in the presence of strain aging,” *Fract. Nano Eng. Mater. Struct. - Proc. 16th Eur. Conf. Fract.*, pp. 827–828, 2006.

[74] Y. Liu, S. Kyriakides, and J. F. Hallai, “Reeling of pipe with Lüders bands,” *Int. J. Solids Struct.*, vol. 72, pp. 11–25, 2015.

[75] J. F. Hallai and S. Kyriakides, “On the effect of Lüders bands on the bending of steel tubes. Part II: Analysis,” *Int. J. Solids Struct.*, vol. 48, no. 24, pp. 3285–3298, 2011.

[76] M. Mazière and S. Forest, “Strain gradient plasticity modeling and finite element simulation of Lüders band formation and propagation,” *Contin. Mech. Thermodyn.*, vol. 27, no. 1–2, pp. 83–104, 2013.

[77] M. Ma and Yishang Zhang, “Advanced high strength steel and press hardening,” in *Proceedings of the 4th international conference on advanced high strength steel and press hardening*, 2018, p. 632.

[78] K. Sztwiertnia, “Recrystallization,” 2012. [Online]. Available: https://www.intechopen.com/books/recrystallization. [Accessed: 02-Jul-2020].

[79] C. yang Qiu, L. Li, L. lei Hao, J. gong Wang, X. Zhou, and Y. lin Kang, “Effect of continuous annealing temperature on microstructure and properties of ferritic rolled interstitial-free steel,” *Int. J. Miner. Metall. Mater.*, vol. 25, no. 5, pp. 536–546, 2018.

[80] L. Chiang, K. Yang, and I. Hsiao, “Effects of annealing conditions on bake hardenability for ULC steels,” *China Steel Tech. Rep.*, no. 24, pp. 6–11, 2011.

[81] ASTM, “Standard Terminology Relating to Methods of Mechanical Testing,” 2009.

[82] N. Srinivasan, N. Raghu, and B. Venkatraman, “Study on the deformation band characteristics in mild steel using digital image correlation,” *J. Multidiscip. Eng. Sci. Technol.*, vol. 1, no. 5, pp. 400–403, 2014.

[83] S. Nagarajan, R. Narayanaswamy, and V. Balasubramaniam, “An insight into Lüders deformation using advanced imaging techniques,” *J. Mater. Eng. Perform.*, vol. 22, no. 10, pp. 3085–3092, 2013.

[84] A. L. Rechenmacher, S. Abedi, O. Chupin, and A. D. Orlando, “Characterization of mesoscale instabilities in localized granular shear using digital image correlation,” *Acta Geotech.*, vol. 6, no. 4, pp. 205–217, 2011.

[85] LaVision GmbH, “DaVis 8.4 Software.” Germany, p. 344, 2017.

[86] Digital image correlation.org, “A practical guide to DIC,” 2019. [Online]. Available: https://digitalimagecorrelation.org/. [Accessed: 10-Oct-2019].

[87] A. Bonfietti and M. Lombardi, “The Weighted Average Constraint,” *ResearchGate*, no. October 2012, p. 16, 2014.

[88] H. Le, C. S. Nguyen, and A. H. Bui, “Experimental processing of ultra-low carbon steel using vacuum treatment,” *Acta Metall. Slovaca*, vol. 24, no. 1, pp. 4–12, 2018.

[89] H. B. Sun, Y. Kaneda, M. Ohmori, and F. Yoshida, “Effect of stress concentration on upper yield point in mild steel,” *Mater. Trans.*, vol. 47, no. 1, pp. 96–100, 2006.

[90] F. Y. M. Haggag and G. E. Lucas, “Determination of Lüders strains and flow properties in steels from hardness/microhardness tests,” *Metall. Trans. A*, vol. 14, no. 8, pp. 1607–1613, 1983.

[91] N. Tsuchida, Y. Tomota, K. Nagai, and K. Fukaura, “A simple relationship between Lüders elongation and work-hardening rate at lower yield stress,” *Scr. Mater.*, vol. 54, no. 1, pp. 57–60, 2006.

[92] G. T. Van Rooyen, “Basic factors which influence the Lüders strain during discontinuous yielding,” *Mater. Sci. Eng.*, vol. 7, no. 1, pp. 37–48, 1971.

[93] C. Bruton, M. Governance, and B. Street, “Simulating the response of free-standing rocking rigid bloks using Abaqus/standard,” *SIMULIA UK Reg. User Meet.*, 2017.

[94] A. F. Ab Ghani, M. B. Ali, S. Dharmalingam, and J. Mahmud, “Digital image correlation (DIC) technique in measuring strain using opensource platform Ncorr,” *J. Adv. Res. Appl. Mech.*, vol. 26, no. 1, pp. 10–21, 2016.

[95] D. V. Johnson, “Lüders bands in RPV Steel,” PhD dissertation, Cranfield University, Cranfield, 2012.

[96] P. Bing, D. W, and Y. Xia, “Incremental calculation for large deformation measurement using reliability-guided digital image correlation,” *Opt. Lasers Eng.*, vol. 50, no. 4, pp. 586–592, 2012.

[97] R. Cintrón and V. Saouma, “Strain measurements with the digital image correlation system Vic-2D,” 2008.

[98] B. Pan, H. Xie, Z. Wang, K. Qian, and Z. Wang, “Study on subset size selection in digital image correlation for speckle patterns,” *Opt. Express*, vol. 16, no. 10, p. 7037, 2008.

[99] X. Gu, Y. Liang, and S. Fu, “Evaluation and optimization of digital image correlation processing variables using genetic algorithm,” *J. Strain Anal. Eng. Des.*, vol. 51, no. 6, pp. 408–415, 2016.

[100] International digital image correlation society, “A Good practices guide for digital image correlation standardization, good practices, and uncertainty quantiication committee.” p. 94, 2018.

[101] D. Lecompte, S. Bossuyt, S. Cooreman, H. Sol, and J. Vantomme, “Study and generation of optimal speckle patterns for DIC,” *Proc. SEM Annu. Conf. Expo. Exp. Appl. Mech. 2007*, vol. 3, no. Jan, pp. 1643–1649, 2007.

[102] S. Nagarajan, N. Raghu, and B. Venkatraman, “Advanced imaging for early prediction and characterization of zone of Lüders band nucleation associated with pre-yield microstrain,” *Mater. Sci. Eng. A*, vol. 561, pp. 203–211, 2013.

[103] V. I. Danilov, V. V Gorbatenko, and L. B. Zuev, “Luders deformation of low-carbon steel,” *Steel Transl.*, vol. 47, no. 10, pp. 662–668, 2017.

[104] I. Jandrlić, S. Rešković, and F. Vodopivec, “Determining the amount of Lüders band in niobium microalloyed steel,” *Metalurgija*, vol. 55, no. 4, pp. 631–634, 2016.

[105] S. Miyazaki and H. Fujita, “Dynamic observation of the process of Lüders band formation in polycrystalline iron,” *Trans. JIM*, vol. 20, pp. 603–608, 1979.

[106] T. Brlić, S. Rešković, I. Jandrlić, and F. Skender, “Lüders bands at the beginning of the plastic flow of materials,” *Metalurgija*, vol. 57, no. 4, pp. 357–359, 2018.

[107] D. H. Johnson, M. R. Edwards, and P. Chard-Tuckey, “Microstructural effects on the magnitude of Lüders strains in a low alloy steel,” *Mater. Sci. Eng. A*, vol. 625, pp. 36–45, 2015.

[108] H. B. Sun, F. Yoshida, M. Ohmori, and X. Ma, “Effect of strain rate on Lüders band propagating velocity and Lüders strain for annealed mild steel under uniaxial tension,” *Mater. Lett.*, vol. 57, no. 29, pp. 4535–4539, 2003.

[109] H. C. and G.Stone, “The effect of stress on the Lüders band velocity in niobium,” *J.Mech.Phys.Solids*, vol. 12, pp. 139–148, 1968.

[110] M. A. Meyers and K. K. Chawla, *Mechanical behavior of materials*, Second edi. Cambridge, 2009.

[111] A. V. Jarred Cadwell, “Propagation of Error,” 2020.

[112] H. H. Ku, “Notes on the use of propagation of error formulas,” *J. Res. Natl. Bur. Stand. Sect. C Eng. Instrum.*, vol. 70C, no. 4, p. 263, 1966.

[113] D. Weisz-Patrault, L. Maurin, N. Legrand, A. Ben Salem, and A. Ait Bengrir, “Experimental evaluation of contact stress during cold rolling process with optical fiber Bragg gratings sensors measurements and fast inverse method,” *J. Mater. Process. Technol.*, vol. 223, pp. 105–123, 2015.

[114] V. Tvergaard, *Necking in tensile bars with rectangular cross−section*, vol. 103, no. 1−2. p. 273−290.

[115] J. L. D. and S. J. H. Z. Marciniak, *Mechanics of sheet metal forming*, 2nd ed. 2002.

[116] P. Perzyna, *Localization and fracture phenomena in inelastic solids*. New York: Springer Vienna, 1998.

[117] D. V Wilson and P. S. Bate, “Influences on cell walls and grain boudaries on transient responses on an IF steel to changes in strain path,” *Acta Met. mater*, vol. 42, no. 4, pp. 1099–1111, 1994.

[118] S. Medrano, “Study of concurrent recovery and precipitation on the mechanical behaviour of Al-Mg alloys with small additions of Cu,” no. December, p. 151, 2018.

[119] S. Medrano and C. W. Sinclair, “Transient strain age hardening of Al – Mg alloys,” *Materialia*, vol. 12, no. March, 2020.

[120] H. Mecking and U. F. Kocks, “Kinetics of flow and strain-hardening,” *Acta Metall.*, vol. 29, no. 11, pp. 1865–1875, 1981.

[121] L. P. Kubin and Y. Estrin, “Evolution of dislocation densities and portevin-Le chatelier effect,” *Acta. Met. Mater.*, vol. 38, no. 5, pp. 697–708, 1990.

[122] E. V. Nesterova, B. Bacroix, and C. Teodosiu, “Microstructure and texture evolution

under strain-path changes in low-carbon interstitial-free steel," *Metall. Mater. Trans. A Phys. Metall. Mater. Sci.*, vol. 32, no. 10, pp. 2527–2538, 2001.

[123] M. S. Pham, M. Iadicola, A. Creuziger, L. Hu, and A. D. Rollett, "Thermally-activated constitutive model including dislocation interactions, aging and recovery for strain path dependence of solid solution strengthened alloys: Application to AA5754-O," *Int. J. Plast.*, vol. 75, pp. 226–243, 2015.

Appendix

This appendix includes the V-Uhard subroutines used for the model developed in chapter 6. Both subroutines used during loading after annealing and reloading after aging are available in this section.

- Using V-Uhard subroutine during loading (as-annealed sample):

```
subroutine vuhard(
C Read only -
     * nblock,
     * jElem, kIntPt, kLayer, kSecPt,
     * lAnneal, stepTime, totalTime, dt, cmname,
     * nstatev, nfieldv, nprops,
     * props, tempOld, tempNew, fieldOld, fieldNew,
     * stateOld,
     * eqps, eqpsRate,
C Write only -
     * yield, dyieldDtemp, dyieldDeqps,
     * stateNew )

      include 'vaba_param.inc'

      dimension props(nprops), tempOld(nblock), tempNew(nblock),
     1 fieldOld(nblock,nfieldv), fieldNew(nblock,nfieldv),
     2 stateOld(nblock,nstatev), eqps(nblock), eqpsRate(nblock),
     3 yield(nblock), dyieldDtemp(nblock), dyieldDeqps(nblock,2),
     4 stateNew(nblock,nstatev), jElem(nblock)
C
C
      parameter ( zero = 0.d0, one = 1.d0 )

C
      double precision val_T, val_k, val_b, eps, epsdot, val_s, val_r,
C
C     character*80 cmname
      val_T = props(1)          !Refers to sigma max
      val_k = props(2)          !Refers to Q1
      val_b = props(3)          !Refers to b1
```

```
      val_s = props(4)          !Refers to Q2
      val_r = props(5)          !Refers to b2

C
      do 100 km = 1,nblock
C

      eps = eqps(km)
      epsdot = eqpsRate(km)
C
        !Elastic deformation
        if(eps .lt. zero) then
          eps = zero
          dyieldDeqps(km,1) = zero
          dyieldDeqps(km,2) = zero

        !Plastic deformation
        else
C          yield(km)= val_T+ val_k * (1- EXP(-val_b *(eps)))   !Array containing the yield stress
     1     - val_s * (1- EXP(-val_r*(eps)))                     (for isotropic plasticity)

           dyieldDeqps(km,1)= val_k * val_b * EXP(-val_b       !derivative of yield stress with
     1     *(eps)) - val_s * val_r * EXP(-val_r * (eps))       respect to eq plastic strain.

           dyieldDeqps(km,2)=0                                 ! strain rate is not taken into
                                                               account

       endif
C
100 continue
      return
      end
```

- Using V-Uhard subroutine during reloading after aging:

```
subroutine vuhard(
C Read only -
     * nblock,
     * jElem, kIntPt, kLayer, kSecPt,
     * lAnneal, stepTime, totalTime, dt, cmname,
     * nstatev, nfieldv, nprops,
     * props, tempOld, tempNew, fieldOld, fieldNew,
     * stateOld,
     * eqps, eqpsRate,
C Write only -
     * yield, dyieldDtemp, dyieldDeqps,
     * stateNew )

      include 'vaba_param.inc'

      dimension props(nprops), tempOld(nblock), tempNew(nblock),
     1 fieldOld(nblock,nfieldv), fieldNew(nblock,nfieldv),
     2 stateOld(nblock,nstatev), eqps(nblock), eqpsRate(nblock),
     3 yield(nblock), dyieldDtemp(nblock), dyieldDeqps(nblock,2),
     4 stateNew(nblock,nstatev), jElem(nblock)
C
C
      parameter ( zero = 0.d0, one = 1.d0 )

C
      double precision val_T, val_k, val_b, eps, epsdot, val_s, val_r, val_DS, val_ep, val_bh, val_q
C
C       character*80 cmname
      val_T = props(1)          !Refers to sigma max
      val_k = props(2)          !Refers to Q1
      val_b = props(3)          !Refers to b1
      val_s = props(4)          !Refers to Q2
      val_r = props(5)          !Refers to b2
      val_DS = props(6)         !Refers to RBH
      val_bh = props(7)         !Refers to  the coefficient term bh
      val_ep = props(8)         !Refers to plastic pre-deformation level
      val_q = props(9)          !Refers to QBH
C
```

```
      do 100 km = 1,nblock
C

      eps = eqps(km)
      epsdot = eqpsRate(km)
C
         !Elastic deformation
         if(eps .lt. zero) then
           eps = zero
           dyieldDeqps(km,1) = zero
           dyieldDeqps(km,2) = zero


         !Plastic deformation
        else if (eps .gt.0.1d0) then
           yield(km)= val_T+ val_k*(1- EXP(-val_b*(eps)))-  !Array containing the yield stress
     1     val_s *(1- EXP(-val_r *(eps)))+val_DS – val_q      (for isotropic plasticity)
     2     *(1- EXP(-val_bh*(eps - val_ep)))

          dyieldDeqps(km,1)= val_k * val_b * EXP(-val_b     !derivative of yield stress with
     1    *(eps))-val_s *val_r*EXP(-val_r *(eps))-val_q       respect to eq plastic strain.

     2    * val_bh*EXP(-val_bh*(eps - val_ep))
          dyieldDeqps(km,2)=0                                ! strain rate is not taken into
                                                               account.



        endif
C
100   continue
      return
      end
```